# Cavitation erosion monitoring by acoustic emission

Markku Ylonen

# THÈSE

Pour obtenir le grade de

**DOCTEUR DE L'UNIVERSITE GRENOBLE ALPES**

**préparée dans le cadre d'une cotutelle *entre***

***la Communauté Université Grenoble Alpes* et *Tampere University***

Spécialité : **Mécanique des fluides, Energétique, Procédés**

Arrêté ministériel : le 25 mai 2016

Présentée par


## Markku YLÖNEN


Thèse dirigée par **Jean-Pierre Franc,** Directeur de Recherche CNRS, LEGI
et **Marc Fivel,** Directeur de Recherche CNRS, SIMaP
et **Pentti Saarenrinne,** Professeur, Tampere University
et **Kari Koskinen,** Professeur, Tampere University
et codirigée par **Juha Miettinen,** Docent, Tampere University

préparée au sein du **Laboratoire des Écoulements Géophysiques et Industriels** (LEGI)
dans **l'École Doctorales I-MEP2 – Ingénierie – Matériaux, Mécanique, Environnement, Energétique, Procédés, Production**

# Cavitation Erosion Monitoring by Acoustic Emission

## Suivi de l'Erosion de Cavitation par Émission Acoustique

Thèse soutenue publiquement le **17 Janvier 2020**,
devant le jury composé de :

**Monsieur Romuald SKODA**
Professeur, Ruhr-Universität Bochum, Président
**Madame Riitta KEISKI**
Professeur, University of Oulu, Rapporteur
**Monsieur Rickard BENSOW**
Professeur, Chalmers University of Technology, Rapporteur
**Monsieur Marc FIVEL**
Directeur de Recherche CNRS, Directeur de Thèse
**Monsieur Kari KOSKINEN**
Professeur, Tampere University, Directeur de Thèse

# PREFACE

I am deeply grateful for all the help in the research and writing of my thesis. I would like to thank my supervisors Pentti Saarenrinne, Jean-Pierre Franc, Juha Miettinen, Marc Fivel and Kari Koskinen for all the lengthy discussions concerning science behind cavitation and acoustic emission and for all the support during the challenging process of getting a research exchange running, along with a double degree under a cotutelle agreement. I would like to thank Pentti and Juha for the confidence they had in me when they hired me first as a Master's Thesis worker and then as a Doctoral Researcher, while sending me to France in the very beginning of my career. The whole exchange process had its challenges, and I am happy that we were able to work them out together. Next, I would like to thank Jean-Pierre and Marc for their contribution to the process, and especially for inviting me as a part of their laboratories and research groups. I felt a strong sense of belonging there, and I spent the most exciting and enjoyable times of my research at LEGI and SIMaP, in Grenoble. Thank you Kari for stepping in as my supervisor, and for helping me through the final stages of the thesis.

During my experiments at LEGI and SIMaP, I got significant help from many coworkers. I would like to especially thank Michel Riondet for teaching me how to use the PREVERO cavitation tunnel and for helping me with the wide range of experiments I carried out with it. I thank also Jan Hujer, Jean-Bastien Carrat, Chakri Ravilla, Prasanta Sarkar, Shrey Joshi, Sholpan Sumbekova, Xiaoyu Qiu, Yves Paquette, Vincent Clary, Guillaume Fromant, Stefan Hoerner, Nickolas Stelzenmuller and all other colleagues and friends I had the pleasure of discussing and spending time with in Grenoble, about many scientific issues, but more importantly, about all possible topics imaginable. I want to thank Jouni Elfvengren, Petteri Multanen, Jukka-Pekka Hietala, Petteri Ojala, Jari Rämö and Pertti Pakonen for the discussions and help during the NEM-Project, and I want to thank Tuomo Nyyssönen, Mari Honkanen, Jarmo Laakso and Pasi Peura for the cooperation in some of our articles. I would also like to thank Fabio Villa and Phoevos Koukouvinis for sharing their data and for their help in one of the publications.

A significant part of the work in my thesis was performed under a project called Accelerated Life Cycle Estimation (NEM – Nopeutettu Elinkaaren Määritys). The goal of the project was to study and develop methods to predict machine wear, with the aid of accelerated testing, concentrating on four separate cases. It was a Business Finland project with industrial partners, providing the cases and funding. The four cases were divided into four work packages: 1) Field data based lifetime testing of mechanical assemblies, 2) Accelerated multivariate component testing, 3) Adaptive life cycle estimation, and 4) Failure and ageing mechanisms and models. The work in my thesis was for a large part carried out under work package 3. The life cycle estimation was out of the scope of this thesis, as it proved out that cavitation and cavitation erosion were so difficult to monitor that it was more fruitful to limit the thesis to them and not to attempt any lifetime estimation schemes.

Therefore, I thank Business Finland, Sandvik Mining and Construction Oy, Fortum Power and Heat Oy, Teollisuuden Voima Oyj, Valtra Oy and all the members of the board of the NEM Project at the Tampere University of Technology. I especially appreciate the help of Voitto Kokko, who made it possible to study such an interesting case. I also thank the Fortum Foundation, who made it possible to finish my work under a grant, when the NEM-project was already finished. Additionally, I thank the Tampereen teknillisen yliopiston tukisäätiö for their grant, which allowed further processing of the thesis after the project. I would like to thank also the staff at Tampere University of Technology, which became a part of Tampere University in 2019, and at Université Grenoble Alpes. I appreciate these academic institutions for all the work for science and the future of humankind.

I thank my parents Merja and Matti Ylönen, and my brother Lauri Ylönen and all my friends for their company and support in life and in the thesis process. Most importantly, I thank my wife Jenni. I am forever happy to love her and be with her, and I appreciate beyond words her support and confidence in me. She did not hesitate to join me in the three-year adventure in France, even when it meant significant uncertainty to her career and life. Additionally, I thank her for helping me through the process, both by encouraging me, and by correcting my grammar in the publications.

Tampere 26th August 2019
Markku Ylönen

# ABSTRACT

Cavitation is the formation of vapor bubbles either in a static liquid or in a liquid flow due to a drop in static pressure. When these bubbles collapse, as a result of pressure recovery, they may damage adjacent surfaces. These events are major causes of damage and nuisance in hydro machines. Modern hydro turbines are often used to regulate power grids; therefore, they may be operated out of their designed range. The flow-related optimal operation is different from the economic optimal usage. Detecting and characterizing cavitation and assessing damage during operation can be difficult or even impossible. Acoustic emission (AE) measurements provide a way to measure cavitation without access to the flow, but interpreting the data is challenging. This thesis presents insights in the ways of treating the AE data both in characterizing individual pits created by cavitation impacts and in tracking the evolution of cavitation erosion. Additionally, the erosion rates of three turbine materials were compared, and the main reasons behind the differing erosion rates of two martensitic turbine steels were discovered. The same high-speed cavitation tunnel was used in all cavitation experiments. This thesis firstly presents a method for enveloping an AE waveform signal and for counting the peak voltage values. The resulting cumulative distributions were compared to those of cavitation pit diameters, and from this comparison, a connection was proposed between AE peak voltage value and pit diameter. The second result was the connection between cavitation cloud shedding frequency and erosion evolution. The process of demodulating high frequency AE signals effectively promotes the low frequency shedding. The shedding frequency increased with accumulating material loss, and it was concluded that this increase is due to geometry effects, namely surface roughness. In addition to the two proposed methods, it was found that the decisive factors in the differing erosion rates of the martensitic stainless steels are the prior austenite grain size, packet and block sizes and the retained austenite fraction. This thesis provides guidelines directly applicable, such as the martensitic steel classifying, and methods that require further development, if one wishes to utilize them in hydro machine cavitation monitoring instead of laboratory measurements in a cavitation tunnel. The main outcome is that AE is a potential way to monitor cavitation, with the important benefit of not requiring any access to the flow.

# RESUME

La cavitation est la formation de bulles de vapeur dans un liquide statique ou en écoulement. L'érosion de cavitation se produit quand ces bulles collapsent à cause de la récupération de pression. Ce phénomène peut endommager les parois à proximité desquelles les bulles collapsent. Il s'agit d'un problème majeur dans les machines hydrauliques. Par exemple, les turbines hydrauliques fonctionnent aujourd'hui souvent dans des régions défavorables du point de vue de la cavitation, pour réguler le réseau électrique. Mesurer la cavitation et le taux d'érosion est souvent très difficile voire impossible. L'émission acoustique (EA) est une méthode qui permet la mesure de cavitation sans accès direct à l'écoulement ; toutefois, les données sont difficiles à interpréter. Cette thèse présente quelques possibilités de traitement des données de l'EA pour quantifier les diamètres des indentations créées par impacts individuels de la cavitation et aussi pour évaluer l'érosion de cavitation. De plus, les taux d'érosion de trois matériaux d'aubes de turbine Francis ont été caractérisés. Les raisons pour les différences dans le taux d'érosion de deux aciers inoxydables et martensitiques sont analysées. Tous les essais de cavitation ont été réalisés dans le même tunnel de cavitation haute vitesse. Un premier résultat majeur de cette thèse est le développement d'une méthode pour compter les pics d'EA par une technique d'enveloppe du signal. Les distributions cumulées des pics d'EA sont comparées à celles des diamètres d'indentations. Une relation est proposée entre l'amplitude des pics d'EA et le diamètre des indentations. Le deuxième résultat majeur est le lien entre l'évolution de l'érosion de cavitation et la fréquence de lâcher des nuages de cavitation. Bien que les signaux d'EA soient mesurés en haute fréquence, un processus de démodulation a été mis en œuvre qui permet de mettre en évidence la basse fréquence de lâcher. Cette fréquence augmente avec la rugosité et la déformation de surface au fur et à mesure de la progression de l'endommagement. Par ailleurs, les raisons entre les différences de taux d'érosion des aciers inoxydables et martensitiques ont été identifiées : la taille des grains d'austénite initiale, les tailles des plaques et plaquettes et la quantité d'austénite résiduelle sont les principaux facteurs influants. Cette thèse propose plusieurs résultats directement utilisables, comme la classification entre les aciers inoxydables martensitiques, ainsi que des méthodes pour surveiller la cavitation mises au point en laboratoire dans un

tunnel de cavitation et potentiellement applicables aux machines hydrauliques. Le résultat majeur est que l'EA a un fort potentiel pour surveiller la cavitation et l'érosion de cavitation avec l'avantage important qu'elle ne nécessite pas d'accès direct à l'écoulement.

# TIIVISTELMÄ

Kavitaatioksi on ilmiö, jossa joko paikallaan olevaan tai liikkuvaan nesteeseen muodostuu höyrykuplia staattisen paineen pudotessa. Nämä höyrykuplat romahtavat paineen palautuessa, jolloin ne voivat vahingoittaa läheisiä pintoja. Tämä ilmiö voi aiheuttaa vakavia vaurioita sekä häiriötä virtauskoneissa. Moderneja vesivoimaturbiineja käytetään usein sähköverkon tasapainottamiseen, jolloin niitä saatetaan käyttää suunnitellun optimialueen ulkopuolella. Taloudellinen optimi ei aina ole sama kuin virtauksen suhteen optimaalinen ajotilanne. Kavitaation ja sen aiheuttamien vaurioiden tarkastelu käytön aikana on vaikeaa tai jopa mahdotonta. Akustisen emission (AE) mittaukset mahdollistavat kavitaation havainnoinnin ilman suoraa yhteyttä virtaukseen, mutta näiden mittausten datan tulkitseminen on haastavaa. Tässä väitöskirjassa esitellään tapoja tulkita AE-dataa sekä yksittäisten kavitaatiokuplien romahdusten, että kavitaatioeroosion etenemisen tarkkailun tasoilla. Lisäksi tässä työssä vertaillaan kolmen turbiinimateriaalin eroosionopeuksia. Kahden martensiittisen turbiiniteräksen osalta tarkastellaan syitä eroavien eroosionopeuksien takana. Kaikki kavitaatiokokeet suoritettiin samassa kavitaatiotunnelissa. Ensimmäisenä esitellään menetelmä AE-signaalin verhokäyrän käytöstä AE-signaalin maksimiamplitudien laskentaan. Näistä laskettiin kumulatiiviset jakaumat, joita verrattiin kavitaatiokuoppien halkaisijoiden vastaaviin jakaumiin. Tästä luotiin yhteys AE-signaalin maksimiamplitudien ja kuoppien halkaisijoiden välille. Toinen päätulos oli yhteys kavitaatiopilven romahdustaajuuden sekä eroosion etenemisen välille. Korkeataajuinen AE-signaali demoduloitiin matalan taajuuden romahtamisilmiön havaitsemiseksi. Romahtamistaajuus kasvaa materiaalihäviön kumuloituessa. Tästä pääteltiin, että taajuuden kasvu johtuu virtausgeometrian, muutoksista. Martensiittisten terästen eroosionopeuksien erolle löydettiin syiksi paketti- ja blokkikoot sekä jäännösausteniitin määrä. Tämä väitöskirja esittelee suoraan hyödynnettäviä tuloksia, kuten martensiittisten terästen luokittelu kavitaatiokestävyyden suhteen, sekä menetelmiä, jotka vaativat jatkokehittämistä, mikäli niitä halutaan käyttää virtauskoneiden monitorointiin pelkän laboratoriotestaamisen lisäksi. Tärkein huomio on se, että AE on erittäin lupaava keino kavitaation mittaamiseen. Huomattavin etu AE:lla on siinä, että sen käyttö ei vaadi suoraa yhteyttä, eikä minkäänlaista vuorovaikutusta virtaukseen.

# CONTENTS

## *List of Figures*

## *List of Tables*

# ABBREVIATIONS

Greek symbols

| | |
|---|---|
| $\varrho_w$ | Density of water |
| $\sigma$ | Cavitation number |
| $\tau$ | Coverage time |

Latin symbols

| | |
|---|---|
| $A_e(t_n)$ | Eroded profile area at time $t_n$ |
| $A_{loss}(t_n)$ | Eroded profile area loss at time $t_n$ |
| $D_0$ | Reference pit diameter |
| $D$ | Cavitation pit diameter |
| $D_0$ | Reference pit diameter |
| $f_s$ | Cavitation cloud shedding frequency |
| $H$ | Length parameter in the Strouhal number |
| $h_m(r,t_n)$ | Eroded profile height at radius $r$ and at time $t_n$ |
| $k_i$ | A group of geometry parameters in a flow channel |
| $N$ | Amount of samples in an AE signal |
| $m$ | Running sample index in a time – analytic signal |
| $\dot{N}_{0,peak}$ | AE reference peak rate |
| $\dot{N}_{peak}$ | AE cumulative peak rate |
| $\dot{N}_{0,pit}$ | Reference pitting rate |
| $\dot{N}_{pit}$ | Cumulative pitting rate |
| $p_d$ | Cavitation tunnel downstream pressure |
| $p_r$ | Reference pressure in a hydro machine |
| $p_u$ | Cavitation tunnel upstream pressure |
| $p_v(T)$ | Saturated vapor pressure at temperature $T$ |
| $\Delta p$ | Pressure difference over a hydraulic system |
| $Re$ | Reynolds number |
| $s_r$ | Profilometer radial resolution |
| $St$ | Strouhal number |

| | |
|---|---|
| $T$ | Temperature |
| $t$ | Time |
| $U$ | AE peak voltage value |
| $U_0$ | AE reference voltage |
| $U_{cutoff}$ | AE cut-off voltage |
| $U_{ref}$ | AE system reference voltage |
| $V$ | Flow velocity |
| $V_c$ | Cavity velocity |
| $V_e(t_n)$ | Eroded profile volume at time $t_n$ |
| $V_{loss}(t_n)$ | Eroded profile volume loss at time $t_n$ |
| $X(m)$ | Discrete – time Fourier transform of an AE signal |
| $z(m)$ | One sided N-point discrete – time analytic signal |

Abbreviations

| | |
|---|---|
| AE | Acoustic emission |
| ASL | Average signal level |
| CCD | Charge-coupled device |
| DTFT | Discrete – time Fourier transform |
| EBSD | Electron backscatter diffraction |
| FEM | Finite element method |
| FFT | Fast Fourier transform |
| HDT | Hit definition time |
| IFFT | Inverse fast Fourier transform |
| PVDF | Polyvinylidene difluoride |
| Q&P | Quenching and partitioning |
| RMS | Root mean square value |
| SEM | Scanning electron microscopy |
| UHMWPE | Ultra-high molecular weight polyethylene |

# ORIGINAL PUBLICATIONS

Publication I Ylönen, M., Saarenrinne, P., Miettinen, J., Franc, J-P. & Fivel, M., 2018. Cavitation Bubble Collapse Monitoring by Acoustic Emission in Laboratory Testing. Proceedings of the 10th Symposium on Cavitation (CAV2018): May 14-16, 2018, Baltimore, Maryland, USA. Katz, J. (ed.). ASME, p. 179-184. 05037

Publication II Ylönen, M., Saarenrinne, P., Miettinen, J., Franc, J-P., Fivel, M. & Nyyssönen, T., 2018. Cavitation Erosion Resistance Assessment and Comparison of Three Francis Turbine Runner Materials. Materials Performance and Characterization. Volume 7, Issue 5, p. 1107-1126.

Publication III Ylönen, M., Saarenrinne, P., Miettinen, J., Franc, J-P., Fivel, M. & Laakso, J., 2019. Estimation of Cavitation Pit Distributions by Acoustic Emission. Journal of Hydraulic Engineering. Volume 146, Issue 2, p. 1-11.

Publication IV Ylönen, M., Saarenrinne, P., Miettinen, J., Franc, J-P & Fivel, M., 2019. Shedding Frequency in Erosion Evolution Tracking. International Journal of Multiphase Flow. Volume 118, p. 141-149.

Publication V Ylönen, M., Nyyssönen, T., Honkanen, M., Peura, P., Unpublished Manuscript.

# AUTHORS' CONTRIBUTION

Publication I The author carried out the cavitation and acoustic emission tests and developed the peak counting and enveloping method, with the help of the other authors. The author prepared the manuscript with the help of the others and presented the work in the 10th Symposium on Cavitation (CAV2018)

Publication II The author carried out the cavitation erosion tests and developed the method for calculating volume loss. The SEM images were captured in the SIMaP laboratory by a technician, and the author and Marc Fivel analyzed them. The author prepared the manuscript with the help of the others.

Publication III The author carried out the cavitation pitting tests, combined with the acoustic emission measurements. The author and Jean-Pierre Franc developed the mathematical formulation for the connection between cavitation pit diameters and peak voltage values of the acoustic emission signal. Jarmo Laakso measured the pitted surface using an optical profilometer. The author prepared the manuscript with the help of the others.

Publication IV The author carried out the cavitation erosion tests combined with the acoustic emission measurements. Jouni Elfvengren proposed the AE signal demodulation process, and it was further developed to suit the needs of this study by the author. The video recordings were a courtesy of Fabio Villa, who had recorded them earlier. The videos and the AE signals were analysed by the author. The author prepared the manuscript with the help of the others.

Publication V The author carried out the cavitation erosion tests and analysed the cavitation-related part of the manuscript. Mari Honkanen performed the EBSD measurements and Tuomo Nyyssönen analysed the microstructures of the steels and drew the conclusions regarding the reasons behind cavitation erosion resistance for the martensitic stainless steels. The manuscript was prepared equally by the author, Tuomo Nyyssönen and Mari Honkanen, and it was widely commented by Pasi Peura.

# 1 INTRODUCTION

## 1.1 Background

Cavitation is a major source of damage and vibrations in many modern hydro machines. Cavitation occurs when the static pressure of a liquid drops below a certain threshold, leading to the evaporation of the liquid. Typically, this threshold is the saturated vapor pressure of the liquid. It may also be lower, if there are no nucleation sites for the evaporation to commence. When cavitation occurs in a liquid flow, in a low static pressure region, there is a chance that the vapor bubbles travel to a higher-pressure region and violently collapse. If these collapses occur near a solid boundary, material damage may occur. This damage is called cavitation erosion. Typically, monitoring cavitation and cavitation erosion during machine operation is difficult, or even impossible. (Brennen 1995; Franc & Michel 2005)

This thesis addresses the issue of cavitation monitoring by presenting novel methods related to acoustic emission (AE) measurement. The aim is to monitor only damaging cavitation: Damage in the form of individual pits or damage in the form of cumulating material loss. AE measurement differs from acoustic sound measurement, as AE refers to elastic waves traveling in a solid, rather than waves traveling in a fluid. The source of these elastic waves can be internal stresses in a material, external impacts, or surface contacts leading to energy release in the material structure. Their expected frequency range is typically from 100 kHz to 1 MHz. Typically, they have a wide frequency band, as the elastic waves are the result of events intrinsically of wide frequency range. (Holroyd 2000; Grosse 2008).

The current work concentrates on laboratory measurements, performed at the LEGI laboratory, using a high-speed cavitation tunnel (PREVERO 2018). The laboratory measurements provided an environment where the primary AE source was cavitation, while all other sources were irrelevant in magnitude. In a hydraulic machine environment, other sources such as rolling bearings or flow related impacts might distract the measurements. In a laboratory environment, there was no doubt

that the AE signal source was cavitation, and more importantly, that the damage to the specimens was due to cavitation impacts. AE does not properly detect cavitation events that occur far from surfaces, as the directed impacts towards walls lead to significantly higher AE responses (van Rijsbergen et al. 2012). For this reason, the potentially damaging events are detected, while the non-damaging events occurring in the free fluid are excluded. With this approach, the AE response of erosive and non-erosive cavitation was identified, thus providing a baseline for the extension to a hydraulic machine, in possible future applications.

To study the possibilities of AE in cavitation monitoring, two approaches were chosen: Cavitation pitting tests to detect individual impacts and their magnitudes, and cavitation erosion tests to study if AE could reveal parameters that change when the material erodes further. In the pitting tests, the cavitation collapses affected a limited area on the specimen, leading to elastic and plastic deformation and pits with no significant overlapping. It was expected that the impact strength would be connected to the AE response magnitude. These pitting tests had a short duration, typically a few minutes, while the erosion tests had a duration of tens of hours. In the erosion testing, individual impacts were not detected, as the damage overlapping begins to change the material and therefore AE responses so that it was not possible to characterize the impacts. It was expected that parameters would be found that change during the erosion tests, as the surface geometry changes and the material strain-hardens significantly; therefore, affecting the bubble – surface interaction, and possibly the resulting AE signal.

## 1.2 Objectives and Scientific Contribution

The main research objectives and research questions of this thesis were:

1. How fast do the studied steels, used in Francis turbine runner blades, erode in a cavitation tunnel?

2. What are the main reasons behind the differing cavitation erosion rates?

3. Can individual, damaging cavitation impacts be detected and characterized via acoustic emission?

4. Can acoustic emission be used in tracking the erosion process of a material experiencing cavitation erosion?

The main approach was to study the material specimens in a cavitation tunnel, combined with AE measurements. A vast campaign of experiments was carried out, with no prior knowledge if the research questions could be answered. Three different materials, specimens from runner blades of Francis turbines, were subjected to cavitation both in pitting tests and in erosion tests. The pitting tests were expected to provide information about individual cavitation impacts and about the impact load distributions. The aim of the erosion tests was to seek knowledge about erosion rates, and more importantly, to find if acoustic emission could be used in tracking the erosion evolution. The main scientific contributions of this thesis were:

1. characterizing the cavitation erosion rates of the turbine steels and identifying the main erosion mechanisms and the reasons behind the differing erosion resistances (Publications II and V);

2. linking the cavitation pit diameter distributions to the acoustic emission peak voltage distributions, thus creating a method to characterize a cavitation field in terms of resulting pit diameters, regardless of cavitation intensity (Publications I and III); and

3. proposing a method to identify the cavitation cloud shedding frequency by acoustic emission, and finding a way to track erosion evolution through the changes in this frequency (Publication IV).

The author's initial work with cavitation begun in (Ylönen 2016). In this master's thesis, one of the steel specimens was eroded, while recording AE with a setup inferior in performance to that used in later work. This initial work allowed the author to acquire the basic skills to properly run the cavitation tunnel and perform the erosion tests. The gained knowledge was also used in defining the required performance of the new AE setup.

The pitting tests are a well established method in cavitation research. However, combining these tests with AE and counting the AE peak voltages was a novel approach. Publication I explains how the AE peak voltages were extracted from enveloped AE signals, and how they were distributed, depending on the cavitation intensity. Publication III utilizes this method in combining pit distributions and AE

peak distributions, thus finding a way to estimate the cavitation intensity in the cavitation tunnel without access to the pitted surface of the specimens.

During all the erosion tests, AE was measured along with the volume loss process of the specimens. Publication II studies the erosion rates of all the three studied materials, the erosion process, and the reasons behind the differing rates. The AE part of the erosion studies is discussed in Publication IV, where the tracking of the cavitation cloud shedding frequency was introduced, in order to first identify this frequency, and then use it in erosion evolution tracking. Publication V concentrates on the differences in microstructure between two of the studied steels, the main finding being that residual austenite seems to reinforce martensitic stainless steels against cavitation impacts.

# 2 CAVITATION AND CAVITATION EROSION

## 2.1 Cavitation

According to (Arndt 2014) Froude was the first to use the term cavitation, probably in 1895. Euler was first to study and problematize cavitation, without using the term, in his 1754 memoir and Reynolds was the first to carry out a study about cavitation in a constricted tube. Cavitation was for the first time found problematic in ship propellers, as their rotation speed begun to exceed the critical values for cavitation to occur. Rayleigh was the first to calculate, in 1917, the erosion potential of an individual bubble. Obviously, the early models were simplified, and insufficient in properly assessing the complex process of, for example, bubble cloud formation, cavitation inception, collective bubble collapses and material resistance and response to cavitation impacts. Cavitation remains an important topic, as modern hydraulic machines tend to be operated at their maximum performance and utility, often in the vicinity of damaging cavitation.

The basic knowledge and understanding of cavitation and cavitation erosion is best found from several textbooks. Young's book *Cavitation (Young 1989)* offers a lot of knowledge on the basic principles behind the phenomenon. Brennen's *Cavitation and Bubble Dynamics* (Brennen 1995) and Franc and Michel's *Fundamentals of Cavitation* (Franc & Michel 2005) both present all the required basic knowledge and they offer supplemental information about some of the more advanced features. Kim et al. wrote the *Advanced Experimental and Numerical Techniques for Cavitation Erosion Prediction* (K. H. Kim et al. 2014). It concentrates more on the advanced features of cavitation, most notably cavitation erosion. Half of it is studies and conclusions presented by the authors and half of it is selected papers from the most recent and advanced studies of cavitation erosion. All these were important sources for this thesis.

Cavitation may occur in a static or a moving liquid, although cavitation in a liquid flow is more representative of the case of hydro machines. The drop in pressure leads to the breakdown of the bonds between molecules that compose a liquid, i.e. it vaporizes. The vapor-liquid equilibrium pressure is the saturated vapor pressure.

For water, it is 2315 Pa at 293 K temperature (Mills 1999). However, the nucleation of vapor bubbles require nucleation sites, such as non-condensed gas or other impurities. In absence of these nucleation sites, a static liquid may experience a metastable state at negative absolute pressure, called tension (Berthelot 1849-1858; Caupin & Herbert 2006; Heyes 2008). In the case of hydraulic machines, nucleation sites are often abundant. Therefore, it is often practical to consider the critical pressure for cavitation to be the saturated vapor pressure.

Rayleigh (Rayleigh 1917) first mathematically described the growth – collapse cycle of a spherical bubble in an infinite liquid. Plesset (Plesset 1949) improved the formulation, and thus found further insights regarding the life of a cavitation bubble (Plesset 1970; Plesset & Chapman 1971; Plesset & Prosperetti 1977). Several authors continued the mathematical formulation of the process, thus generating fundamental knowledge about the lifetimes and sizes of idealized bubbles (Knapp et al. 1970); Acosta & Parkin 1975; Hammitt 1979). These mathematical formulations are the basis of cavitation research and they offer guidelines of what to expect from bubbles; therefore, they are worth mentioning. This thesis, however, concentrates on empirical studies, and these equations were never used.

The collapse process of a cavitation bubble in free liquid is symmetrical: The vapor bubble collapses towards its center, and finally it generates a shock wave, when the bubble walls collide. The driving force is the pressure difference: Inside the bubble the pressure is initially saturated vapor pressure, while outside the pressure is the ambient liquid pressure. The more interesting case is the bubble collapse near a boundary. Due to an asymmetrical pressure field, the bubble wall away from the boundary begins to collapse first. This leads to a liquid jet traversing the bubble and directed to the boundary. The liquid jet gains a significant velocity, and hits the boundary, potentially causing damage. In addition to that, the formed bubble ring collapses violently, also potentially causing damage. (Zhang et al. 1993; Zhang et al. 1994; Brujan et al. 2002; Obreschkow 2012)

An essential parameter in many cavitation studies is the cavitation number. The cavitation number is a non-dimensional parameter that is essentially the ratio between the difference of a reference pressure in a hydraulic system and saturated vapor pressure, and the pressure difference over the system. It is useful in defining the inception or closure of cavitation in the system, as they typically occur at the same cavitation number regardless of pressure level. Additionally, cavitation in a

system tends to have same characteristics, such as the closure location of cavitation, with the same cavitation number but different overall pressure or flow velocity. The pressure difference is related to the flow velocity of the system; therefore, the ratio is between static pressure and dynamic pressure. The cavitation number $\sigma$ is generally defined as (Franc & Michel 2005):

$$\sigma = \frac{p_r - p_v(T)}{\Delta p} \qquad 1$$

where $p_r$ is the reference pressure, $p_v(T)$ is the saturated vapor pressure at the flow temperature and $\Delta p$ is the pressure difference over the system. The reference pressure is typically a pressure conveniently measurable, such us the downstream pressure of the system. The cavitation number is a relative parameter, so the exact value alone gives no insight if there is cavitation in the system or not. The cavitation tunnel used in this study has its cavitation inception at $\sigma \approx 2.8$, and the erosion tests were done at $\sigma \approx 0.87$, where cavitation may be considered fully developed.

This thesis concentrates in experiments carried out in a hydrodynamic cavitation tunnel (PREVERO 2018). The tunnel produces a cavitation type typical to hydrofoils: The cloud cavitation. Traveling bubbles, which is the first main type of cavitation, may form in a low-pressure region and then travel to a higher-pressure region and disappear either by collapsing or by slow reduction of size. These transient isolated bubbles are usually less erosive than attached or sheet cavities, which are the second main cavitation type. The attached cavities form in the leading edges of hydrofoils or blades. They follow the flow towards the trailing edge, and potentially collapse near the foil surface, thus promoting damage. An oscillating sheet cavity is called a cloud cavity, discussed in more detail in section 2.2. The last main type of cavitation are the cavitating vortices. A vortex core has a lower pressure than the rest of the vortex. With high enough vorticity, the core may cavitate. These cavitating vortices may for example form between turbine blades, if the water flow angle of attack is not optimal. It has the potential to be highly damaging. (Avellan 2004; Franc & Michel 2005; Escaler et al. 2006).

## 2.2 Cloud Cavitation Shedding Frequency

Cloud cavitation is characterized by an oscillating growth-collapse cycle of a group of cavitation bubbles. This cloud typically grows attached to a surface, until it reaches

a critical length for a liquid counter-current flow to form between the cavity and the surface. This counter-current flow detaches the cloud from the surface, leading to the near-simultaneous collapse of all the bubbles in the cloud. The bubble collapses tend to initiate further collapses, thus the collapse of the cloud is self-driven, after it has begun. If the collapse occurs sufficiently near to the surface, damage may occur. The main parameters affecting the formation of such clouds are the flow velocity, overall pressure, liquid quality, flow geometry and surface quality. By increasing flow velocity around a hydrofoil, starting from no-cavitation state, cavitation typically begins as individual bubbles, followed by a sheet cavity with no periodical cloud formation. With more velocity, a cloud pattern begins to appear, and with a sufficiently high velocity, super cavitation occurs, where cavitation closure is outside the hydrofoil. (Brennen et al. 2000; Franc & Michel 2005; Nishimura et al. 2014; Gnanaskandan & Mahesh 2016; Hsiao et al. 2017)

The transition from sheet to cloud cavitation occurs at a critical cavitation number. The cavitation number for cavitation inception is the number where the initial individual bubbles begin to form. The inception of cavitation may be pinned to quite an exact cavitation number, but the transition from sheet to cloud cavitation includes a transient area. Additionally, the cavitation number for the transition is also dependent of the flow Reynolds number. (Pelz et al. 2017) mapped the transition in their testing geometry that was a converging-diverging nozzle. With a low Reynolds number, the cavitation remains a sheet even with low cavitation numbers, and increasing the Reynolds number increases the critical cavitation number. A narrow transition region is found between the sheet and cloud cavitation regions. (Keil et al. 2012)

The frequency of the cloud formation and collapse cycle is dependent of the Reynolds number, cavitation number and channel geometry. Typically, the frequency is expressed through the Strouhal number, which is a dimensionless number defined as (Pelz et al. 2014):

$$St(Re, \sigma, k_i) = \frac{f_s H}{V} \qquad 2$$

where $Re$ is the Reynolds number, $k_i$ is the group of geometry parameters, for example related to channel curvature, $f_s$ is the shedding frequency, $H$ is the length parameter, for example channel height, and $V$ is the flow velocity. Above a critical

Reynolds number, the Strouhal number is no longer dependent on the Reynolds number, only on the cavitation number and channel geometry (Pelz et al. 2014).

The geometry parameter could include the surface roughness of a channel. This notion is interesting in the scope of this thesis, as an increase in roughness would correspond to increased cumulative erosion, as explained in Publication IV. This is supported by the observations of (Hao et al. 2017), who found a shedding frequency of 17 Hz for a smooth hydrofoil, while that of a rough hydrofoil was 20 Hz, in equal flow conditions. (Stutz 2003) found no influence of roughness to the sheet cavity shape, void fraction or time-averaged velocity. This suggests that the roughness influences the circulation of the counter-current flow between the cloud cavity and the surface, but not the cavity itself.

One of the main goals in this thesis was to monitor the evolution of cavitation erosion. Monitoring this shedding frequency proved to be the most reliable way, as the frequency was consistently found using acoustic emission measurements. The shedding frequency is not particularly difficult to find in general, via for example video analysis, but measuring it by AE provides a way to define the frequency during operation and without visual access to the flow. A pressure sensor in the channel wall sufficed for (Keil et al. 2012) and (Pelz et al. 2014), but AE has the advantage that it is installed outside the flow, to a solid surface that has a solid transfer path to the cavitating region. However, correlating the shedding frequency changes to erosion evolution was a novel approach, as far as the author of this thesis is aware of, and it was first presented in Publication IV.

The most reliable way to study the cloud cavitation phenomenon in a laboratory environment is filming it with a high-speed video camera. This approach was also used for Publication IV, to verify that the frequencies defined through AE are the correct ones. The videos were kindly provided by (Gavaises et al. 2015), who also had analyzed them. They were reanalyzed for Publication IV with a slightly different approach. The simulation results for the cavitation tunnel geometry by (Gavaises et al. 2015) were also compared to the frequencies defined by AE and the video analysis, and all three were consistent with each other.

The high-speed videos from cavitation were recorded so that the cloud length is well captured. They were filmed only from one direction, so no accurate imaging of the cloud structures was available. The experimental procedure is explained in more

detail in (Gavaises et al. 2015). The 2-D image was sufficient for finding the main frequencies associated to the cavitation, as long as there was a cloud structure. Several overall pressures and cavitation numbers were included, with cavitation numbers where assumedly the structure was sheet cavitation rather than cloud cavitation.

The videos were filmed in grayscale. The method for this thesis was to track the grayscale value of all the 256 x 128 pixels through all the frames in each video, and then calculate the fast Fourier transformation (FFT) and thus transform the grayscale value evolution to frequency domain. In Figure 1, the grayscale value of a single location in one of the videos is plotted, along with the frequency domain analysis.

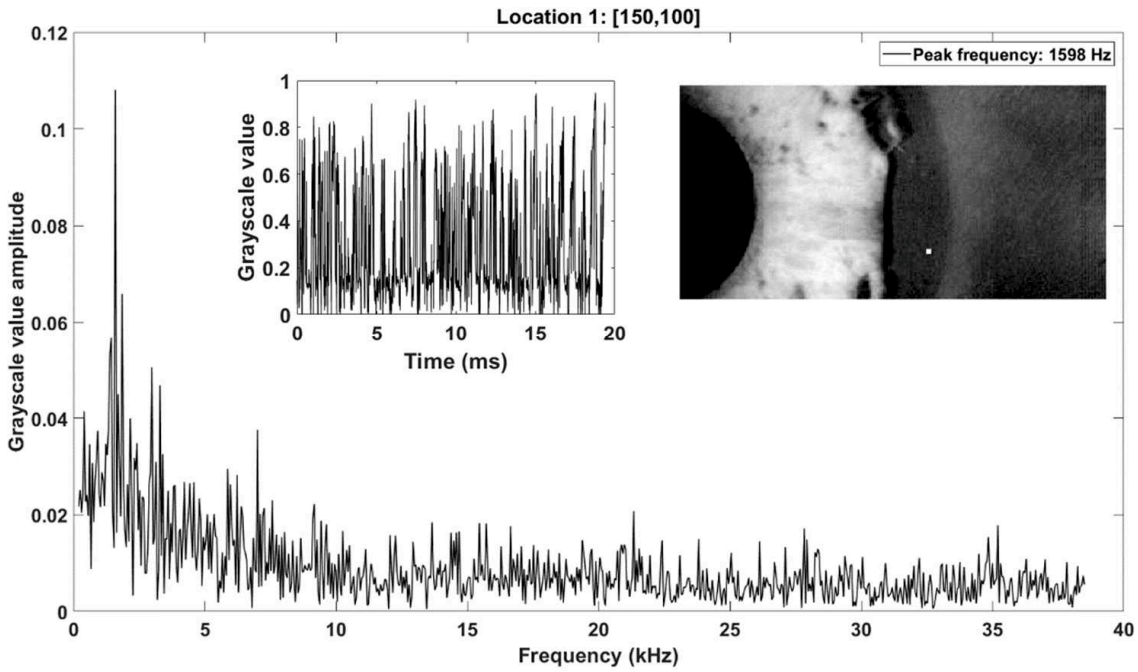


**Figure 1.** Grayscale value in time and frequency domain for $\sigma = 0.908$ and an upstream pressure of 4 MPa from the high-speed videos of PREVERO cavitation tunnel.

The location marked by the small white square in Figure 1 is in the area that the clouds typically reach when they are fully-grown. Interestingly, the dominating frequency is found from most of the locations where there is any cavitation. Only the masked area in the left side of the images and the right side that cavitation does not reach, do not reveal any important frequencies. The mapped frequencies from the full image for five different cavitation numbers were presented in Publication IV, where also the AE based frequencies were compared to these and the results from simulations by (Gavaises et al. 2015). This method of capturing the shedding

frequencies by video analysis proved to be a simple, effective and fast method to decipher if there is an oscillating cloud cavity in the system, at least in the limited scope of the laboratory tests in the tunnel. Probably, in a more complex geometry, the cloud cavitation phenomenon would have to be filmed with stereoscopic imaging to capture the periodicity properly.

## 2.3 Cavitation Pitting

If a flat surface with minimal roughness, such as a mirror-polished metal surface, experiences cavitation, the initial damage is observed as individual pits. An individual bubble collapse may lead to pressures up to several GPa (Hsiao et al. 2014; Roy et al. 2015; Roy et al. 2015). This well exceeds the yield stresses of most materials. However, a single impact rarely leads to mass loss, in the case of engineering metals. When the pits begin to accumulate, the mass loss occurs through fatigue. The formation of an individual pit includes elastic and plastic deformation, the plastic part forming the remaining pit when the loading has disappeared. Studying these individual pits may reveal the magnitudes of the loadings required to create them. An example of such a pit is presented in Figure 2, imaged using scanning electron microscopy (SEM).

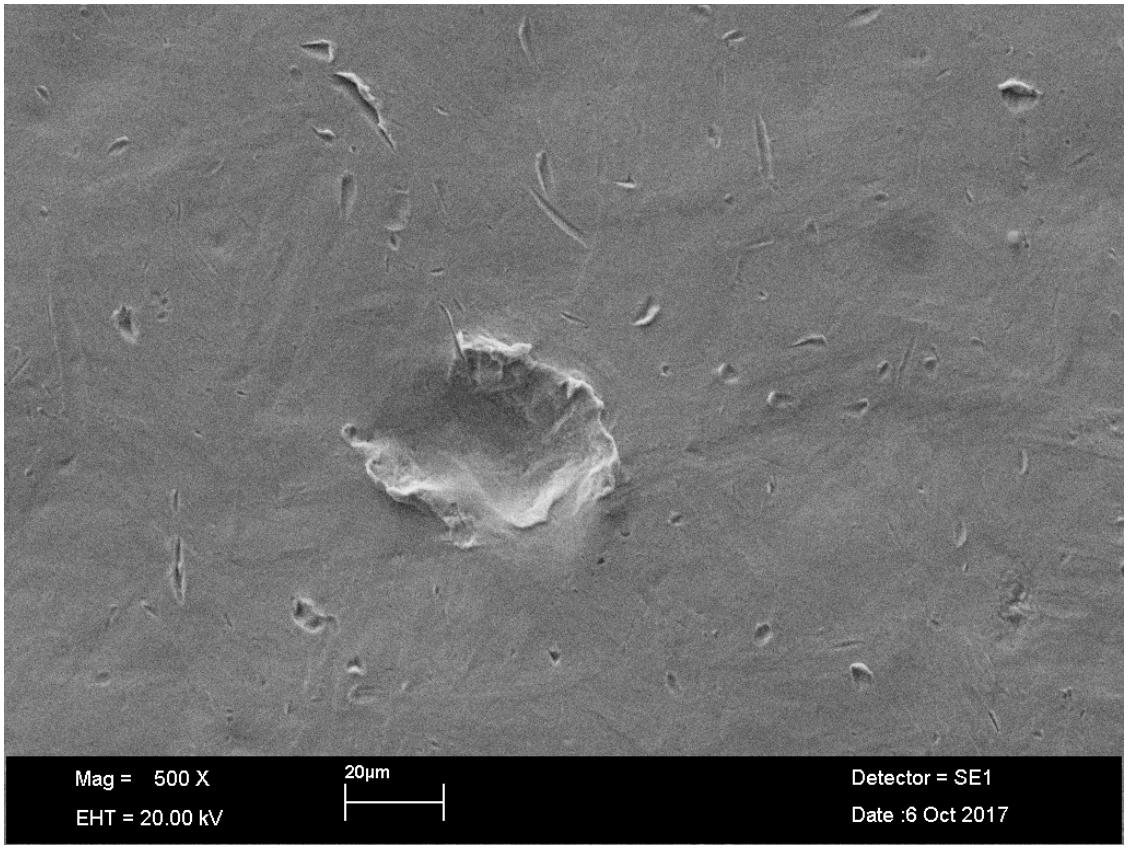


**Figure 2.** A SEM image of a single cavitation pit on a stainless steel surface.

One approach to study the magnitudes of the loadings is via inverse finite element method (FEM). (Roy 2015) was able to define impact loads in the same cavitation tunnel that was used in the studies behind this thesis. Another approach is the modelling of the cavitation bubbles through computational fluid dynamics, either with or without fully coupled interaction with the bubble and the material surface (Chahine & Kalumuck 1998; Hsiao & Chahine 2013; Hsiao et al. 2014). The relation between cavitation pits and impact loads is usually considered strong, but (Choi & Chahine 2015) stated that a pit of a certain shape might be formed from various types of loadings. Another important factor of cavitation pitting in real materials is the often microscopic size of the impacts. If the impact is small enough in area, the attack may be directed not to the bulk material, but to an individual grain in the surface (Carnelli et al. 2012).

Experimental studies related to pitting and impact loads are numerous. (Franc 2009; Franc et al. 2011; Franc et al. 2012) studied the velocity and material effects in a cavitation tunnel, the same that was used in this thesis. They studied the impact loads by conventional pressure sensors and they found power laws that govern the

pit distributions, with normalized flow velocities. A different approach was by (Hujer et al. 2015; Hujer & Muller 2018), who fitted specimens with polyvinylidene difluoride (PVDF) pressure sensors. Additionally, (Carrat et al. 2017) utilized the same sensors to study the impacts on a hydrofoil experiencing cavitation. The PVDF sensors are well suited for defining the actual impulse pressures in a cavitation test (Kang et al. 2018). A common factor in the studies in this particular cavitation tunnel, regardless of methods, was that the pit and impact distributions followed an exponential law: The larger the pit diameter or the impact strength, less numerous they are in a statistical analysis.

The fact that the expected distribution is exponential was helpful in determining firstly if measurements were likely to be correct. In the AE measurements especially, there were occasions that the measured distributions were far from exponential. Further analysis showed problems such as signal saturation or sensor malfunction. The exponential distribution of pits can be well expressed as a mathematical formula, and its properties may be easily compared, especially when a similar distribution is found from pressure or AE measurements. The distributions were found to be more practical to present as cumulative distributions. An exponential cumulative distribution in cavitation pitting is expressed as:

$$\dot{N}_{pit} = \dot{N}_{0,pit} e^{-\frac{D}{D_0}} \qquad 3$$

where $\dot{N}_{pit}$ is the cumulative pitting rate, $\dot{N}_{0,pit}$ is the reference pitting rate, $D$ is the pit diameter and $D_0$ is the reference pit diameter. The diameter was defined as the equivalent diameter of a circle, calculated from the pit surface area. The reference pit diameter $D_0$ is the mean value of pit diameters over the distribution. The reference pitting rate $\dot{N}_{0,pit}$ is the pitting rate when $D = 0$. It is possible to quantify the pit size accurately for a single pit. However, for a pit distribution to be statistically valid, one needs to measure at least hundreds of pits. This leads to practical limitations in the measurement setup. In Publication III, the pits were detected using an optical profilometer with a 3.5226 μm x 3.5226 μm measurement grid. The grid resolution was a compromise between accuracy and measurable surface size. With this resolution, the minimum observable pit diameter was 15 μm, but the complete eroded surface could be analyzed. This minimum pit diameter effectively leads to the ignoring of smaller pits, as observed in Figure 3. The diameters were sorted into bins and afterwards sorted according to their sizes. This makes the figures clearer, as each bin may contain tens to hundreds of measured diameters.

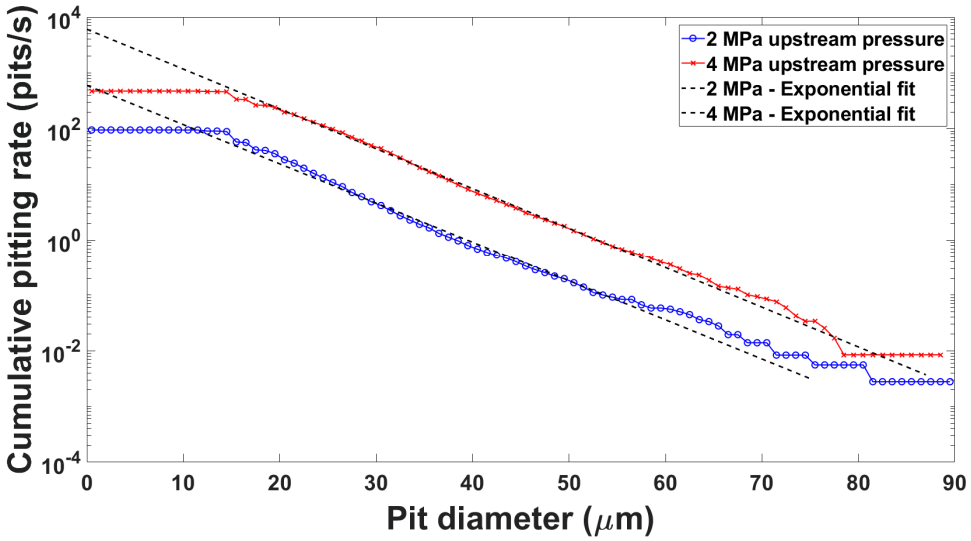


**Figure 3.** Cumulative pitting rate as a function of pit diameter for 2 MPa and 4 MPa upstream pressures. There are no detected pits below the 15 µm limit, observed as flattening of the linear curves. The diameter bin size was 1 µm. The scale is linear – logarithmic.

The ignored small pits of diameter less than 15 µm are observed as a flat part in the measured curve. It does not mean that they would not exist in the eroded surface. An assumption was made that the exponential distribution follows equation 3 globally. This assumption is based on the measurements by (Franc et al. 2012), who measured the same types of samples using a different profilometer. They had a better resolution with a smaller measured surface, and they found pits of the size of a few µm, still following the exponential distribution. The linear part of the plot in Figure 3, which is in linear – logarithmic scale, corresponds to an exponential distribution. According to this assumption, the linear trend continues below the profilometer-based limit of about 15 µm. The 2 MPa and 4 MPa upstream pressures correlate with the cavitation velocity, overall cavitation tunnel pressure and cavitation intensity, as further explained in section 4.1.

## 2.4 Cavitation Erosion

The evolution of cavitation erosion in metals may be divided into three or four stages, depending on the case: 1) The incubation period, 2) the acceleration period, 3) the steady state period and 4) the deceleration. The incubation period is the period where a virgin material starts to experience cavitation erosion and the impacts cause mostly plastic deformation in the form of pits, such as presented in section 2.3. As

the pits begin to overlap, cracking and rupture starts to occur and the erosion moves through acceleration period to steady state period, where the material loss rate is relatively constant. In the deceleration period, the material surface is filled with structural cavities that begin to damp the incoming cavitation impacts, thus reducing material loss rate. In cavitation testing, the deceleration period is not always reached due to limitations in the testing procedures. (Zhou & Hammitt 1983; Berchiche et al. 2002; Franc 2009; Franc et al. 2014; Chahine et al. 2014)

Cavitation erosion often cumulates slowly in hydraulic machines, as strong cavitation is normally detected as machine vibration, noise and performance drop. Therefore, these operating conditions are naturally avoided. However, slowly cumulating erosion processes lead to a loss of structural integrity, lowered performance and in the worst case, in machine breakdown, if they are not assessed properly. Cavitation and cavitation erosion may be avoided by machine design, but it is not desirable to design machines too safely out of range for cavitation to happen, due to lowered performance. Therefore, somehow knowing the extent of erosion in long-term operation is important. (Arndt et al. 1989; Farhat & Bourdon 1998; Bourdon et al. 1999)

In designing machines that can endure cavitation, material resistance to cavitation erosion is an important parameter. The resistance to cavitation is often closely linked to the material strength in terms of typical mechanical parameters, as in studies by (Hammitt 1979; Zhou & Hammitt 1983; Hattori & Nakao 2002; Hattori et al. 2004; Hattori & Ishikura 2010). This is not always true, as cavitation impacts may erode an area smaller than the material grain size, thus attacking also the softer grains in an isolated manner. For this reason, the macro-scale parameters might not provide information about the strength against cavitation. Additionally, the impacts have a high strain rate of up to $10^6$ 1/s (Karimi & Leo 1987). This means that the strain rate dependency of the material has an important role. Additionally, the erosive potential of cavitation depends on the cavitation type. (Carnelli et al. 2012; Roy 2015)

Considering all these factors, the resistance to cavitation may be stated as case-dependent, and there is no single exact parameter to define the goodness of a material in hydraulic channels potentially experiencing cavitation, even though stronger material usually means better resistance. There are multiple cavitation testing methods to compare materials. The test methods differ in how they generate cavitation and in which form. Some of these testing methods are listed here:

- The (ASTM G32-10, Standard Test Method for Cavitation Erosion Using Vibratory Apparatus 2010) is a vibrating horn for basic and relatively low cost cavitation testing. The material specimens are attached to a vibrating horn that is in a static liquid. Cavitation is created as the pressure field around the specimen oscillates, thus creating tension in the liquid. This type of testing was done for example by (Kendrick et al. 2005; Hattori & Kitagawa 2010; Hattori et al. 2010; He & Shen 2012; Pöhl et al. 2015).

- The (ASTM G134-95(2010)e1, Standard Test Method for Erosion of Solid Materials by a Cavitating Liquid Jet 2010) is a system that directs a liquid jet on a specimen resting in static liquid. Cavitation is created in the shear layer between the moving jet and the static liquid. It was used for example by (Soyama & Futakawa 2004; Soyama 2013; Nishimura et al. 2014).

- Different types of rotational setups that are based on periodically opening and closing valves. Cavitation forms due to expansion waves that this motion creates. Some examples are presented in (Karimi 1987; Auret et al. 1993).

- Cavitation tunnels of various types. Cavitation tunnels are utilized both to study cavitation structures and cavitation erosion. Cavitation structures were studied for example by (Steller et al. 2005; Arabnejad et al. 2018; Chen et al. 2018) and erosion in a cavitation tunnel by (Dular et al. 2006; Dular & Osterman 2008; Franc et al. 2012).

The ASTM G32 typically involves weighing the specimens. The specimens are small, about 10 mm high and about 10 mm diameter cylinders, and the eroded surface represents a relatively significant amount of the total specimen mass. Therefore, the measurement resolution is sufficient. However, for example in the tunnel used for this thesis, weighing the specimens would be impractical. The eroded area does not cover the whole specimen, which is a 20 mm high and 100 mm diameter cylinder. Measuring milligrams of erosion would be difficult from a specimen that weighs more than 1 kg, if it is steel. For this reason, and also to provide additional information about the erosion profile, measuring surface profiles is a better option compared to weighing. Material loss may be simply calculated from the surface profiles.

In this thesis, the surface profiles were measured using a contact profilometer. The eroded surface was a circle, with a ring shaped cavitation pattern that has a maximum erosion rate approximately in the radial distance of 22 mm from the specimen center. The entire eroded area ranges from 19 mm to 32 mm radius, as observed in Figure 4. Initially the specimen was mirror polished, and it remained so through the test campaign outside the area of effect of cavitation.

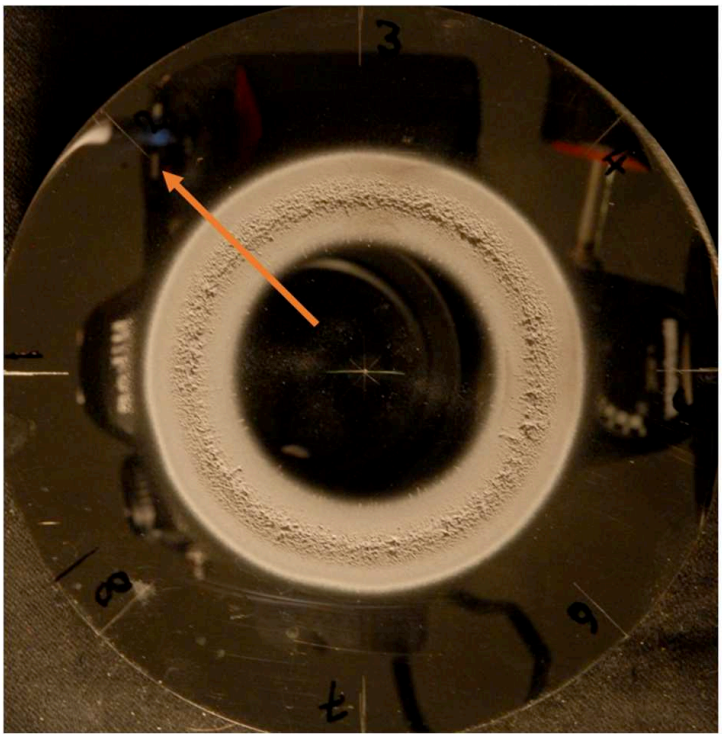

**Figure 4.** Eroded stainless steel specimen after 65 hours of cavitation. The arrow indicates the profile measured for Figure 5.

The specimen in Figure 4 corresponds roughly to the maximal erosion that was reached in the tests for this thesis. The erosion profile in the direction of the arrow is presented in Figure 5. Eight such profiles were measured for each specimen and each time step, and the results were averaged. The erosion rate was observed to significantly change depending on the measurement direction, as explained in more detail in section 5.1.

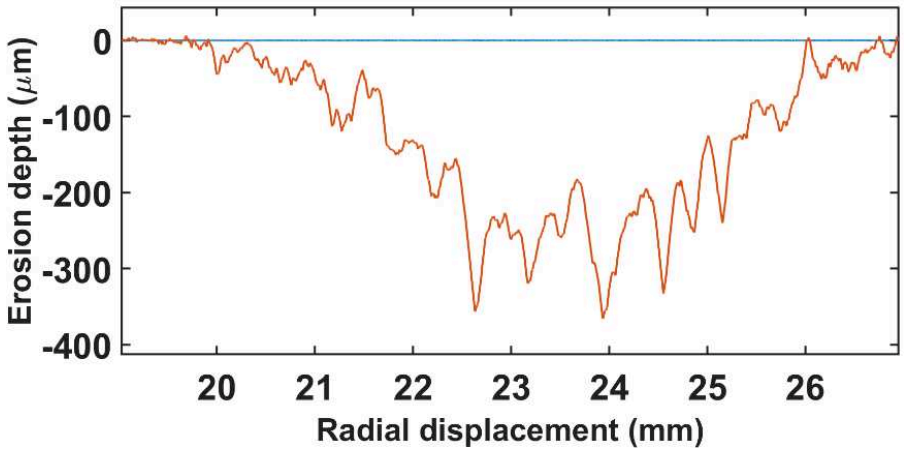


**Figure 5.** Surface profile of the eroded stainless steel specimen in Figure 4. The initial profile is virtually flat, compared to the significantly eroded surface after 65 hours of cavitation at maximum aggressiveness.

The initial surface profiles were almost flat, compared to the eroded profiles. The variation from the zero level due to imperfect polishing in the eroded area was typically less than one μm. Therefore, in terms of volume loss the initial profile had no significance when calculating the volume loss of evolved erosion stages. Anyhow, the initial profile was measured and the volume losses of later stages were corrected by subtracting that of the initial stage.

# 3 CAVITATION DETECTION BY ACOUSTIC EMISSION MEASUREMENTS

## 3.1 Acoustic Emission

Acoustic emission is defined as elastic waves that travel in a solid material. The waves are the result of material internal stresses, external impacts or surface contacts. They usually have a wide frequency band, resulting from the wide frequency band of the AE event. Typically, AE is sought from the range of 100 kHz to 1 MHz, but in some applications, wider ranges may be useful. Piezoelectric sensors are used in measuring AE. They are attached to a surface that has a good transfer path to the expected AE source. AE measurements could be compared to seismic measurements, as AE sensors measure the surface motion, as do the seismograms, but the scale being in the micro rather than the macroscale. (Achenbach 1975; Holroyd 2000; Grosse 2008; Ohtsu et al. 2016)

Cavitation is typically considered as noise in AE measurements, as they are often used in structural integrity monitoring. That monitoring suffers greatly if there is cavitation near the target AE source, as it tends to bury all other signals underneath it due to its larger magnitude. In this thesis however, cavitation is the target parameter. Cavitation was found to induce AE voltages of about 100 times larger than the signal from a flow without cavitation. Therefore, it was practical to assume that all strong signals were directly or indirectly the result of cavitation.

An AE signal is typically symmetrical around zero volts and the positive and negative voltages measure the same phenomenon. AE signals may be divided into two main categories: burst signals and continuous signals. Continuous AE may be for example the result of friction in a sliding contact, such as in a bearing, and it is typically harder to characterize (Grosse 2008). Burst signals result from short duration releases of energy, such as in crack propagation, or relevant to this thesis, short duration impacts such as from cavitation bubble collapses. The burst signals are typically relatively rare, representing only a tiny fraction of the total measurement

time. However, in the cavitation tunnel used in this thesis, they were so numerous that they almost overlapped. Publication III presents these results.

In addition to the categories of burst signals and continuous AE, another important classification is the sensor types. The two main types are the resonance type sensor and the broadband sensor. Both of them are in similar casing, typically a metal cylinder of about 20 mm high and 20 mm diameter, with the detection face made of a ceramic material. The resonance type sensor has a distinct resonance frequency that is amplified inside the sensor. The resonance frequency is dependent on the piezoelectric element size and material. The broadband sensor design differs from the resonance type only so that it has a damping material around the piezoelectric element. This damping suppresses wave reflections inside the sensor, thus reducing the resonance frequency amplification and leading to a flatter frequency response. (Ohtsu 2008; Inaba 2016)

AE is often treated in separate "hits". A hit is an event of AE activity that begins with the crossing of a voltage threshold that is either preselected, or tied to the current average signal level. The hit ends, when a preselected time, called the hit definition time (HDT), has passed without any threshold crossings. The parameters defining AE activity are usually calculated over these hits. Typical parameters, according to (Ohtsu et al. 2016), are listed here:

1) AE signal amplitude. The peak amplitude of the hit is the maximum absolute voltage of the hit, expressed either in volts or in decibels. In decibels, the amplitude is calculated as:

$$Amplitude\ (dB) = 20log\left(\frac{U}{U_{ref}}\right) \qquad 4$$

where $U$ is the peak voltage value and $U_{ref}$ is the AE system reference voltage, usually 1 μV.

2) AE count expresses the amount of threshold passings in a hit. AE count rate is the AE count divided by hit length.

3) AE energy is either the time integral of the absolute values or the time integral of the squares of the absolute values over the hit. The squared integral produces values in Joules, if it is divided by an assumed system impedance, for example 10 kΩ in many systems.

4) Hit duration is the time from trigger to end of hit.

5) Rise time is the time it takes from the trigger to maximum amplitude.

6) Ratio of rise time to amplitude. This parameter provides insight on how short the event is compared to its amplitude. This may also be expressed in terms of counts before peak amplitude.

7) AE root mean square (RMS) value. RMS value is the square root of the mean value of the squared voltage values over a hit.

8) Average signal level (ASL). ASL differs from RMS so that the mean value is taken from the absolute values instead of their squared values.

The AE setup calculates these parameters by default, in one form or another, along with some other additional parameters. Spectral parameters, such as peak frequency, average frequency or frequency centroid, are often recorded as well. AE setups often save the data as parameter groups defining each hit, but they might also be able to record full waveforms, either for a short period or continuously, depending on hardware capability. These full waveforms allow any imaginable parameters to be calculated in post-treatment, which was found very useful in this thesis.

## 3.2 Cavitation and Acoustic Emission

As already mentioned in section 3.1, the cavitation tunnel used in this thesis provided cavitation intense enough for the events to almost overlap in the AE signal. Two sensor types were used in all measurements: One resonance type sensor and one broadband sensor. The resonance type sensor was found to be more sensitive to the burst signals resulting from the cavitation bubble collapses. This is probably due to the structure of the sensors. While the damping in the broadband sensor flattens the frequency response, it also probably increases the rise time of the sensor response. This is well perceived in Figure 6, where broadband and resonance sensor signals are compared.

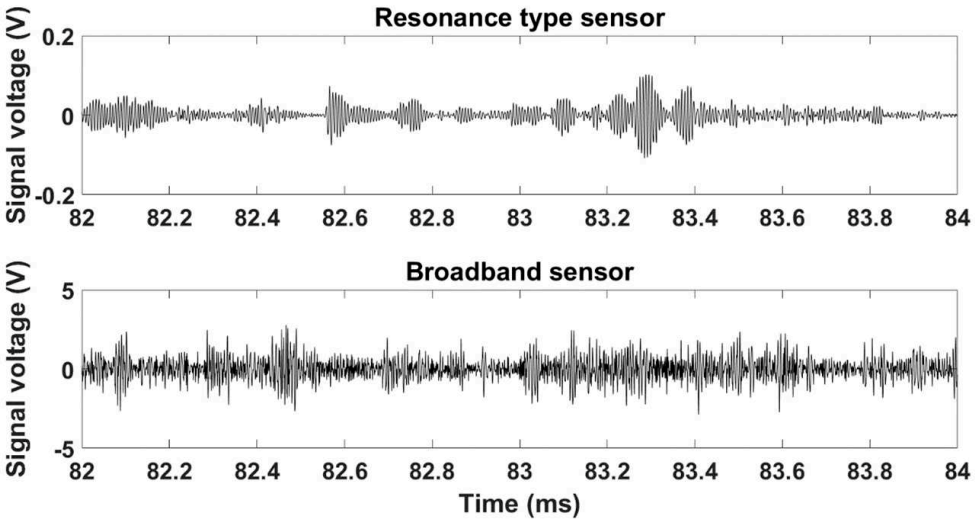


**Figure 6.** Comparison of sensor responses of an AE signal resulting from cavitation. The resonance type sensor was a PAC R15D and the broadband sensor was a PAC D9203b. The sampling rate for both was 5 MHz.

The nature of the signal is not so easily deciphered for the broadband sensor. It is safe to assume that cavitation creates burst signals, as cavitation events are typically several microseconds long (Chahine et al. 2014). Therefore, it was assumed in this thesis that the separate bursts in the resonance signal represented individual cavitation bubble collapses. The AE responses to bubble collapses and their cumulative distributions was studied in Publication III, in which only resonance type sensor results were found useful. Both the broadband and the resonance sensors were able to measure the same frequencies for cloud shedding, presented in Publication IV. Detecting cavitation impacts and detecting the erosion evolution required different tools, but both of them required developing new ways to treat the AE signals, as the default parameters provided by the AE setup were not sufficient for these studies, as described in section 3.5.

## 3.3 Cavitation Impulse Detection

This section describes a method to analyze statistically the cavitation impulses via AE. The enveloping and peak counting method presented here was the approach in Publication III. In cavitation research, the method as presented here has not been previously used, as far as the author of this thesis is aware of. The method produced statistical distributions of the impacts that were possible to connect with the cavitation pitting distributions, described in section 2.3. The relation to the statistical

distributions was not dependent of cavitation intensity, only of the AE setup and its transfer path, and probably the specimen material. This suggests that the AE peak voltage values have a direct connection to the actual impact loads induced by cavitation, but the scaling of AE voltages to impact pressures was out of the scope of this study. The results in this thesis were compared to those of (Hujer et al. 2015; Hujer & Muller 2018), who utilized PVDF sensors for the same purpose and in the same cavitation tunnel. Additionally, the work by (Franc et al. 2011; Franc et al. 2012) provided the baseline in what to search from the AE signals in the tunnel.

The principal assumption in this thesis is that the burst signals in AE represent cavitation impulses, resulting either from single bubbles collapsing or from bubble clouds in which individual bubbles collapse virtually simultaneously. A single burst in AE lasted in the order of 0.1 to 1 ms. Therefore, a collective bubble collapse with μs timescale differences would not be differentiated in these measurements. For the purpose of impulse detection, only the results from the analysis of the resonance type sensor were used, as they were better separated in the signal.

The AE signals in the cavitation pitting tests had the same appearance than those in Figure 6. The approach in Publication III was rather simple: If a single bubble collapse induces a fairly well distinguishable burst in the AE signal, the maximum amplitude of that burst could correlate with the impact load. The AE signals were relatively long, with different burst durations, so a reliable method to detect the peaks was required. Enveloping the absolute values of the signal and then counting the envelope peaks proved effective. The envelope was a peak envelope that utilized spline interpolation, with a pre-defined minimum distance between the peaks. The minimum distance in this thesis was chosen to be 80 samples, which corresponds to 16 μs of signal. This is about 5 times the wavelength corresponding to double the resonance frequency of the sensor. As the absolute signal was calculated before the enveloping, the original wave minima turned to maxima, leading to a doubled apparent frequency. This value of minimum distance was found to properly filter out the sensor resonance effects, while still following the overall signal shape and not creating false peaks. Figure 7 presents an extract of an AE signal absolute value with a fitted envelope.

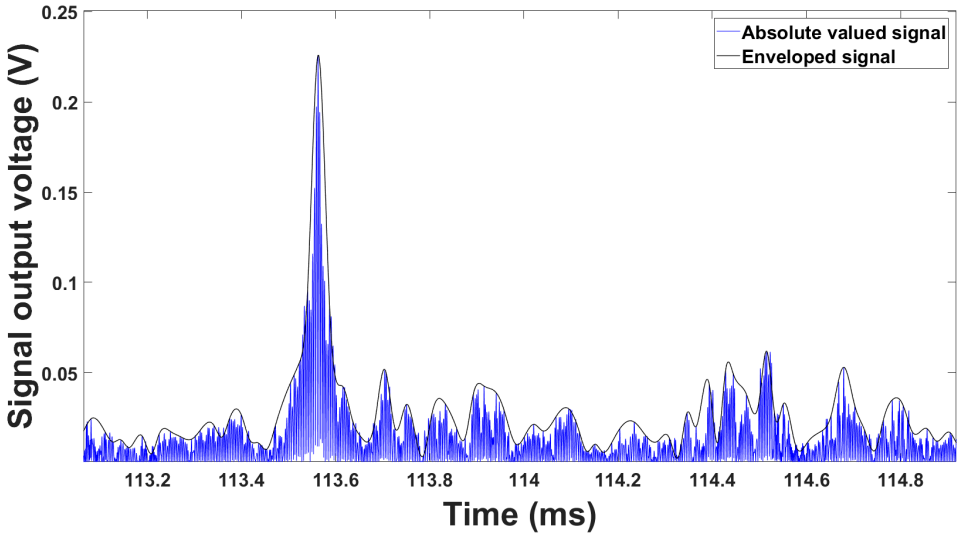


**Figure 7.** The enveloped signal. The peaks from the enveloped signal are detected through regular peak counting methods.

This type of approach detects the relatively high peaks extremely effectively, but it tends to create a large quantity of small peaks. These peaks are however insignificant in the final analysis, as an assumption was made that AE contains more peaks than there are pits in the pitting distributions. Therefore, it was safe to assume that voltage peaks under a certain threshold were either from noise or from events insignificant in damage accumulation. The total peak rate was in this thesis in the order of 10,000 peaks per second, dropping quickly if a threshold value was applied. Interestingly, even the assumed noise and small impacts followed the same exponential distribution in some of the measurements.

To analyze the distributions, it was chosen to display them as cumulative, as with the pitting distributions in section 2.3. The cumulative distributions for the peak voltages may be expressed similarly as for pits in equation 3:

$$\dot{N}_{peak} = \dot{N}_{0,peak} e^{-\frac{U}{U_0}} \qquad 5$$

where $\dot{N}_{peak}$ is the cumulative peak rate, $\dot{N}_{0,peak}$ is the reference peak rate, $U$ is the peak voltage and $U_0$ is the reference peak voltage. The reference peak voltage is the mean voltage over the whole distribution and the reference peak rate is the peak rate when $U = 0$, assuming the distribution is valid over the whole range of voltage values. It was found practical to define a cut-off voltage $U_{cutoff}$, which is the voltage limit with only noise and non-damaging impacts below it. It was assumed that the

cut-off voltage was a material and setup dependent parameter that is essential to define for a system of this kind. Equation 5 can be expressed with the cut-off voltage applied to it:

$$\dot{N}_{peak} = \dot{N}_{0,pit} e^{-\frac{U-U_{cutoff}}{U_0}} \quad 6$$

In this form, the equation is only valid for voltages above the cut-off limit. The Y-axis intersection is at $\dot{N}_{0,pit}$, which replaces $\dot{N}_{0,peak}$ in equation 5. This formulation was found beneficial, as described in section 5.3. Figure 8 presents the peak voltage value distribution with the cut-off voltage applied. The peak voltage values were arranged to bins, such as in Figure 3 with the diameters, to improve readability.

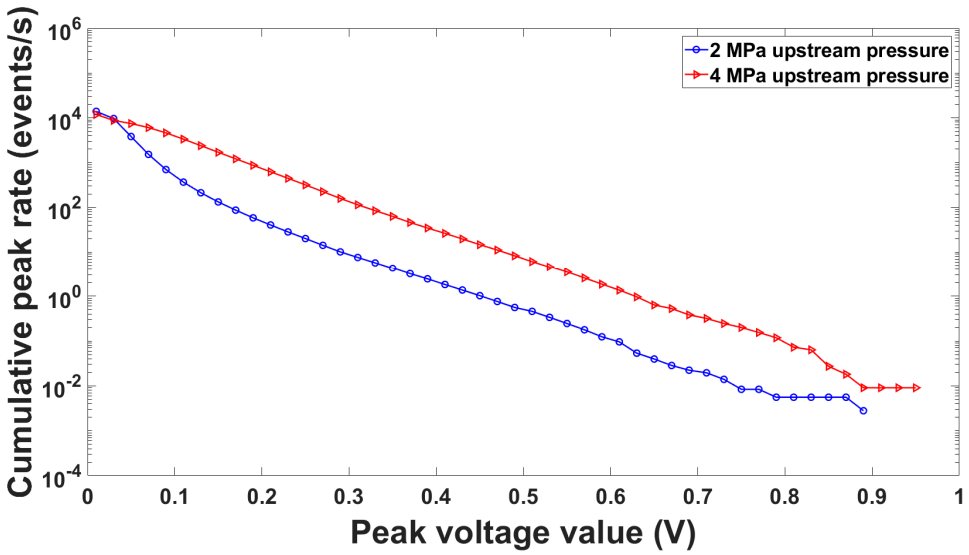


**Figure 8.** Peak voltage distributions for the 2 MPa and 4 MPa upstream pressures in the cavitation tunnel. The scale is linear – logarithmic. The voltage bin size was 0.2 V.

The cut-off voltage was about 0.05 V for both upstream pressures, but it is discussed in more detail in section 5.3. The linear part in the linear – logarithmic scale was assumed to hold true globally, even for the 2 MPa case, even though Figure 8 suggests that below 0.1 V, the peak voltage data becomes less reliable. The most important data, lays in the truly exponential part, as it is assumed that the small impacts do not contribute that much in the damage accumulation. Additionally, the 4 MPa plot seems to be linear until 0 V, while the 2 MPa plot converges towards the 4 MPa value. Therefore, it was assumed that the 2 MPa plot below 0.1 V consists

mostly of noise, generated already in the sensor or in the enveloping process, and it can safely be excluded from the impulse distribution estimation.

## 3.4 Acoustic Emission Responses of Steel Ball Impacts

In an attempt to study the dependency of the impact location on the specimen surface, a series of tests was conducted, including steel balls dropped to the surface. This section provides no answer to how this would affect measurements in a hydraulic machine. Even though adding some doubt in the applicability of AE amplitude based cavitation monitoring, it does not negate the results of Publication III. The ball drop tests points out that the results in Publication III are well applicable in an axisymmetric geometry as in PREVERO, since the AE responses may be statistically regarded as an average of the whole surface. Further studies of this phenomenon would have required research out of the scope of this thesis. However, it is important to point this out for the sake of possible future research and development.

The AE sensors were placed behind the specimens, described in section 4.1. They capture all the events occurring in the specimen surface, as the elastic waves radiate well in the solid material. However, the waveguide is located in a certain position on the surface, and therefore a question can be asked: Are cavitation impacts falling on different locations of the specimen surface equal in their AE responses? In an attempt to answer this question, a test campaign of dropping steel balls on specimen surface was realized, while recording AE from the sample.

The specimens were attached to the specimen holder, but not in the cavitation tunnel. Two steel balls of different weights were dropped on the sample surface to different locations from a height of 35 mm, using a fixed altitude screw system. This allowed fast repeating of loadings, even while manually returning the ball to the system, while assuring that the balls were at the same height and that they had no significant rotational movement when they were released. The results, presented in Figure 9, were obtained as peak voltages of the burst AE signals generated by the ball impact on the surface. The specimen surface was mirror-polished and non-eroded. In total, 50 impacts were recorded for each of the 13 locations, for two different steel ball weights.

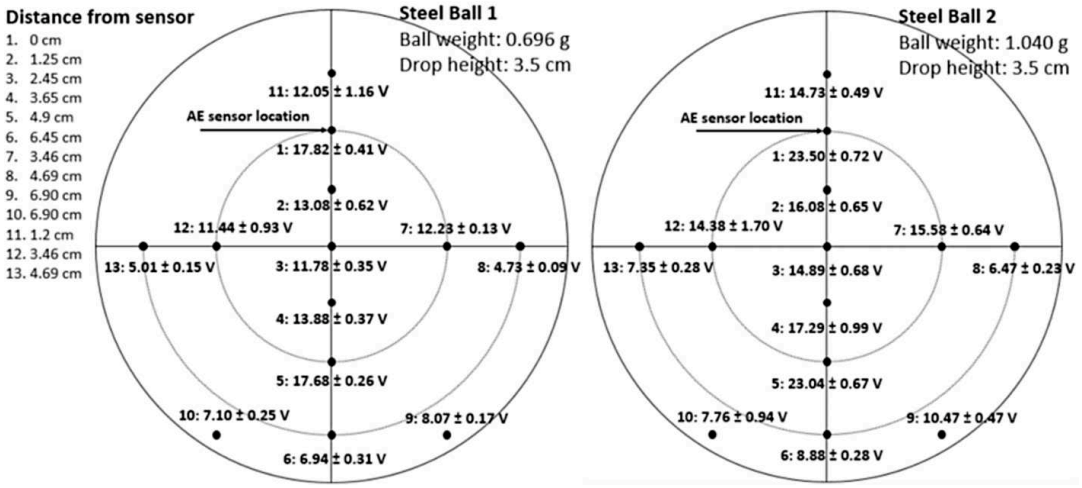


**Figure 9.** AE peak voltages resulting from steel ball impacts. The maximum voltage is highly dependent of the impact location in respect to the sensor location.

The inner circle represents the radius of 24.5 mm, which is the distance of the AE waveguide from the specimen centre. This radius is also roughly equal to the maximum erosion rate in the cavitation tunnel, when the cavitation number $\sigma \approx 0.9$. The peak voltages presented in Figure 9 could be expected to have the highest values as close to the sensor as possible (location 1). This indeed was true, but also the opposite position had almost equal values (location 5). Locations 7 and 12 also have relatively high values, compared to the low values of locations 8 to 10 and 13. The axis consisting of locations 1 to 6 and 11 and the radius of 24.5 mm have the highest values. In the far locations, the values seem to reduce symmetrically from the axis. This is true for both the 0.696 g and 1.040 g balls.

As the values are symmetric around an axis, it is suggested that the effect may be a result of wave propagation in a certain geometry, here a circle. When the specimen holder is attached rigidly to the cavitation tunnel, the geometrical complexity further increases. Considering this, it is unknown how the peak amplitude distribution on the specimen surface would be during a cavitation test. This leaves an open question if cavitation impacts occurring for example in location 1 lead to a different response than those in location 7. There was no way of finding this out in the scope of this thesis. As the responses are more or less symmetric, it was concluded that even if the responses do differ, the results in Publication III are valid, especially as they follow the expected exponential distributions. However, slight doubt is cast on the applicability of the peak count method, and this geometry effect might be worth studying in the future. At least it would be required to study the effects of sensor

location, if one was to attempt hydraulic machine monitoring using the presented method. The shedding frequencies in Publication IV are not dependent of impact amplitudes, so these results do not cause any doubt towards the validity of the presented erosion tracking method.

## 3.5 Acoustic Emission Parameter Analysis

The usual approach in AE studies is the tracking of the parameters for hits. It is a convenient way, as most AE setups save the parameters calculated from hits by default. Additionally, the parameters take much less storage size than the full waveforms. For example in the pitting tests in this thesis, the combined hard disk usage for a 6-minute run was about 62 MB for the parameter-based text file, while it was 43 GB for the same duration of waveforms, captured with a 5 MHz sampling frequency per sensor and for two sensors. The sizes depend on the choices made for the threshold levels in the parametric approach and the sampling frequency, but at least a hundred-fold increase in hard disk usage is expected when capturing the waveforms in full.

The parametric approach has some limitations, at least in cavitation research. They may be overcome, if sufficient experience from the application is available. In the research behind this thesis, the parameter approach was attempted in both the pitting tests and the erosion tests. Especially the erosion monitoring was expected to be possible by following the changes in some parameters. However, in this thesis, no proper correlation was found. Figure 10 and Figure 11 present the four parameters for the resonance type sensor, while Figure 12 and Figure 13 present the same parameters for the broadband sensor. All plots have the volume loss of the stainless steel specimen plotted along with the parameters.

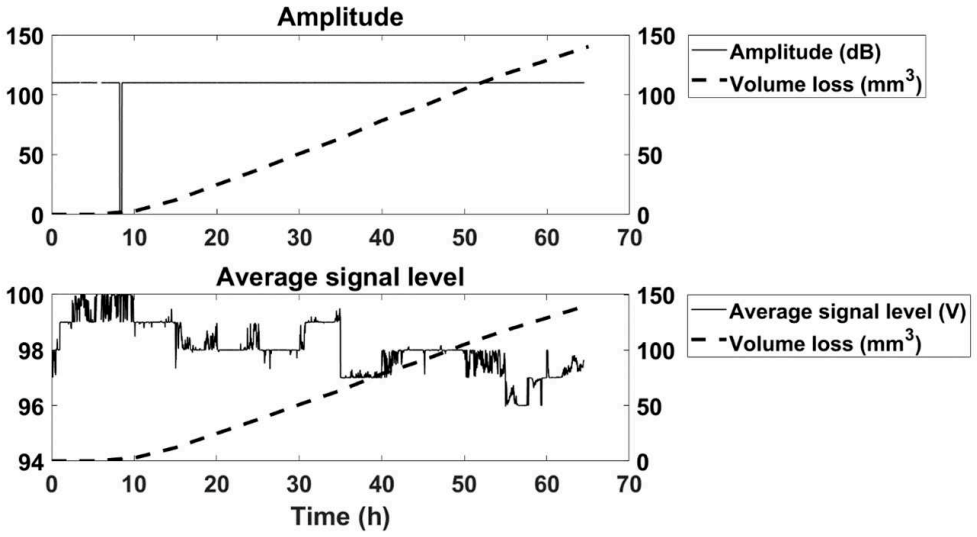


**Figure 10.** Resonance type sensor, amplitude and average signal level as a function of erosion time.

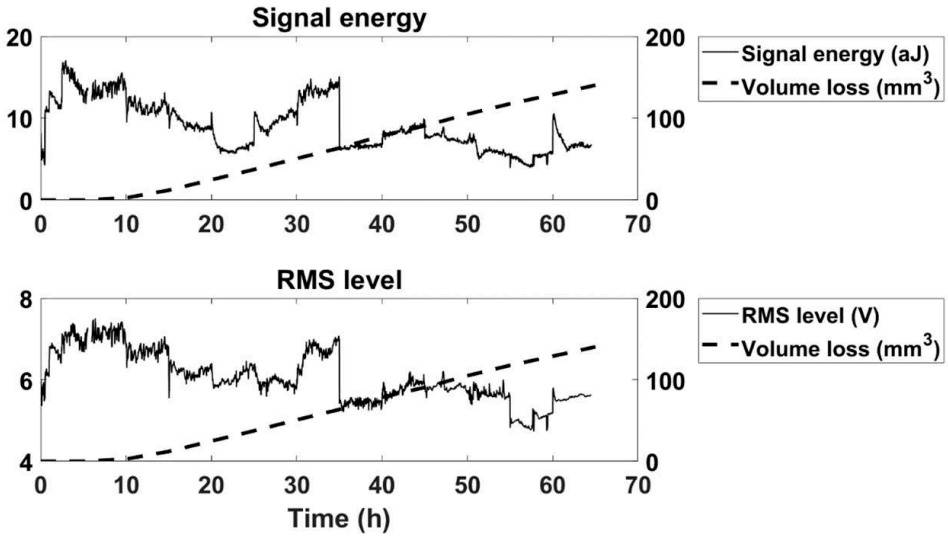


**Figure 11.** Resonance type sensor, signal energy and RMS level as a function of erosion time.

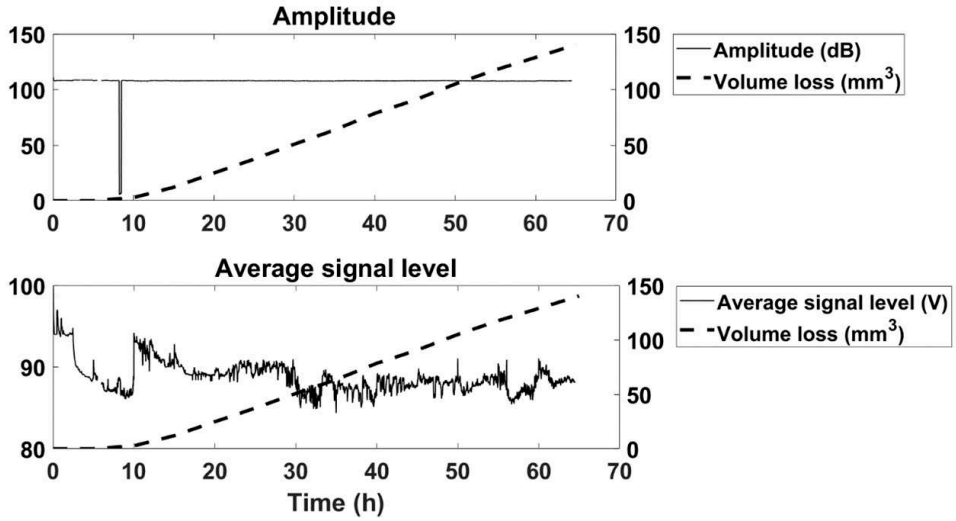


**Figure 12.** Broadband sensor, amplitude and average signal level as a function of erosion time.

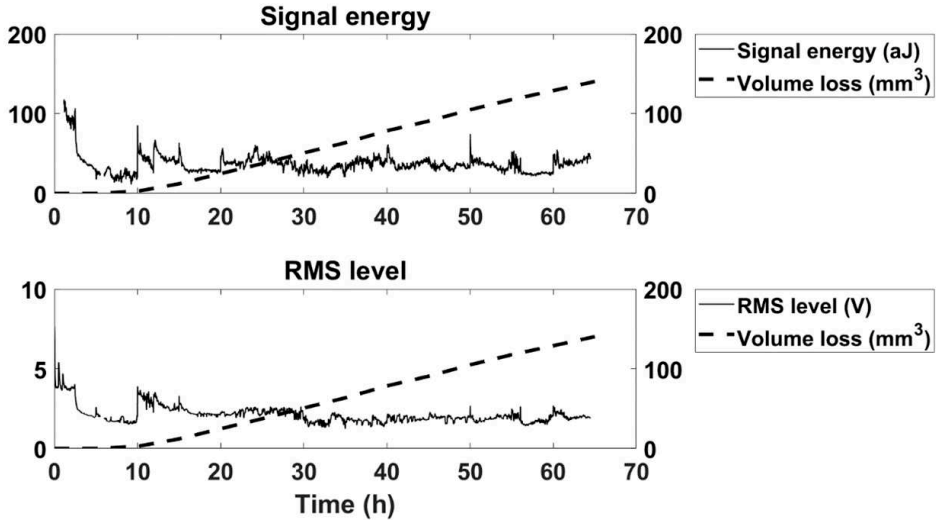


**Figure 13.** Broadband sensor, signal energy and RMS level as a function of erosion time.

All the other calculated parameters show similar trends, with no clear indicators to define a reliable correlation. Notably, the parameters for the resonance type sensor have sharp rises and drops in the parameter levels. The times for these events match with the times that the specimen was removed from the specimen holder for profile measurements. The profile measurements were executed every five hours after an initial sequencing of 4x30 minutes and 4x2 hours. It was assumed that the sharp rises and drops are somehow due to the removal of the AE sensor waveguide from the specimen. The signal level is highly sensitive to the transfer path, so even while executed with care, it is probable that the waveguide to specimen coupling was not always identical.

Despite its limitations, the parametric approach has been successfully used in cavitation research by other authors. The failure of the parametric approach in this thesis proves in no way that the approach could not work. Using machine learning algorithms, neural networks or some other approaches, the trends in the parameters might be revealed better than in the basic analysis in this thesis. Most of the other authors, however, concentrated on determining cavitation occurrence and intensity, rather than erosion evolution. A good example of an advanced approach was by (Look et al. 2018), who did not predefine any features to be tracked. They used convolutional neural networks that were able to detect cavitation in a turbine with high accuracy, with an estimate of the cavitation intensity.

Another example of a successful parametric approach was by (Schmidt et al. 2014; Schmidt et al. 2015). They categorized Kaplan turbine and pump turbine cavitation into four states from no cavitation to severe cavitation. Their experiments included turbines fitted with AE sensors and means to observe visually the state of cavitation. The classification was based on the rise of AE energy and RMS value, and the increased fluctuation of both, when moving towards increased cavitation. (He & Shen 2012) experimented AE and erosion evolution in the ASTM G32 vibratory cavitation testing apparatus. They also tracked the RMS value and the signal energy and they concluded that the average energy shows increase when the specimen mass loss is pronounced. This relation was not found in the current study.

## 3.6 Cavitation Shedding Frequency Detection

As the parametric approach was found not to be suitable for the goals in this thesis, another method, based on spectrum analysis, was developed for the tracking of erosion evolution. As the cavitation produced in the tunnel in this thesis is cloud cavitation, the cavitation impacts attacking the specimen surface have a periodic nature. This was described in detail in section 2.2 and in Publication IV. The shedding frequency in the cavitation tunnel was expected to be between a few hundred Hz to a few kHz (Peters et al. 2015; Gavaises et al. 2015). The AE sensor sensitivity drops rapidly below 100 kHz and the preamplifiers used in this thesis had an analogue band-pass filter with a 100 kHz lower limit and a 400 or 1200 kHz upper limit. Additionally, the measurement system had a digital high-pass filter of a 100

kHz limit. Therefore, the direct spectrum computing methods were not able to detect the shedding frequency, as later observed.

The AE signal strength is highly dependent of the energy and impact strength induced by cavitation events to the specimen surface. Cavitation bubble collapses occurring far from the surface do not significantly raise AE signals (van Rijsbergen et al. 2012). Therefore, it could be assumed that even when the frequencies induced in a collapse of a group of bubbles leads to frequency responses in the measurement range of the AE sensors, these clustered collapse events occur at a much lower rate: the shedding frequency.

A typical acoustic emission signal consists of continuous emission and burst emissions (Kaiser 1950). The cloud collapses are a good example of bursts that produce a strong response. In rolling bearing fault detection, a high-frequency enveloping and demodulation technique may be used (Berry 1997a; Berry 1997b). This approach was found to also serve well for the purposes of cavitation cloud collapse detection. In the case of rolling bearings, the high frequency carrier signal is the resonance frequency of the mounted bearing, while in the case of cloud collapse detection; the high frequency carrier signal is the resulting signal from the sensor resonance. In this thesis and in Publication IV, the technique was carried out using the method presented by (Marple Jr 1999). The idea was to form a "time-analytic" signal of the original signal, which is essentially a way to envelope the signal and to shift the high frequency vibration into low frequencies, from which the shedding frequency can be found via FFT analysis. The steps of the process are the following:

1. The signal was zero-averaged by subtracting the signal mean value.

2. The discrete –time Fourier transform (DTFT) $X(m)$ was formed through FFT for $N$ amount of samples in each signal. In Publication IV, $N$ was 157275000 samples, corresponding to 31.455 seconds of signal with a 5 MHz sampling frequency.

3. A one-sided $N$-point discrete-time analytic signal was formed using the following formulation:

$$z(m) = \begin{cases} X(0), \ for\ m = 0 \\ 2X(m), \ for\ 1 \leq m \leq \frac{N}{2} - 1 \\ X\left(\frac{N}{2}\right), \ for\ m = \frac{N}{2} \\ 0, \ for\ \frac{N}{2} + 1 \ \leq N \leq N - 1 \end{cases} \quad 7$$

4. An inverse $N$-point DTFT was calculated via inverse FFT (IFFT). Adding the original mean signal to this value yields the discrete-time analytic signal.

5. The analytic signal was then decimated and low-pass filtered. The low-pass filter was an eighth order Chebyshev type 1 filter, default in the Matlab function *decimate*. The decimation reduces the sampling rate, in order to reduce sample size and to remove the unnecessary high frequency residuals. The decimation ratio was 250 in this thesis, leading to a new sampling frequency of 20 kHz.

6. To obtain the new demodulated frequency spectra, the spectral density was calculated by Welch's method. Welch's method was chosen because it reduces signal noise. The loss of resolution was not an issue, as the samples were relatively long.

Figure 14 presents a short interval of an AE signal from a pitting test, with an upper envelope that attempts to follows the overall level of the signal. The envelope in Figure 14 was created following steps 1-4 in the demodulation process. Steps 5-6 include the low-pass filtering and transformation to frequency domain. All the data handling for these results was done in Matlab®.

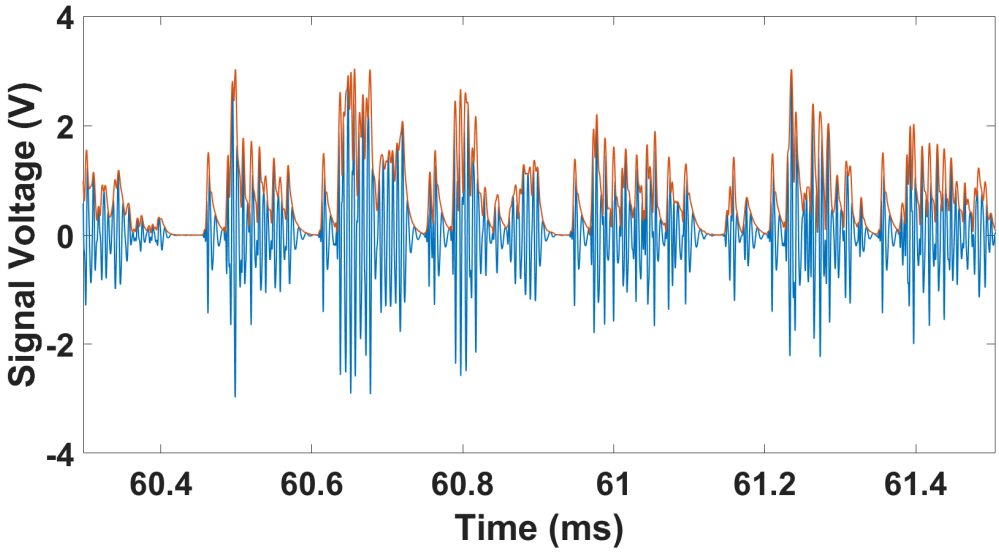


**Figure 14.** The envelope visualization of the high frequency signal acting as a carrier wave to the shedding frequency. The discrete-time analytic signal follows the original signal (blue) as an envelope (orange).

The resulting spectra contained consistently the dominating low frequency spectra. The method proved to be highly effective in promoting the cloud shedding frequencies in the cavitation signals. Spectrum calculation via Welch's method or simple low-pass filtering with decimation of the original signal was not sufficient in promoting the low frequency content, as visualized in Figure 15, which compares the original, decimated and demodulated signals through their spectra. The decimated signal was multiplied by 1000, for the purpose of visualization. Without the multiplication, the decimated signal overlapped the original spectrum so that they were not discernible.

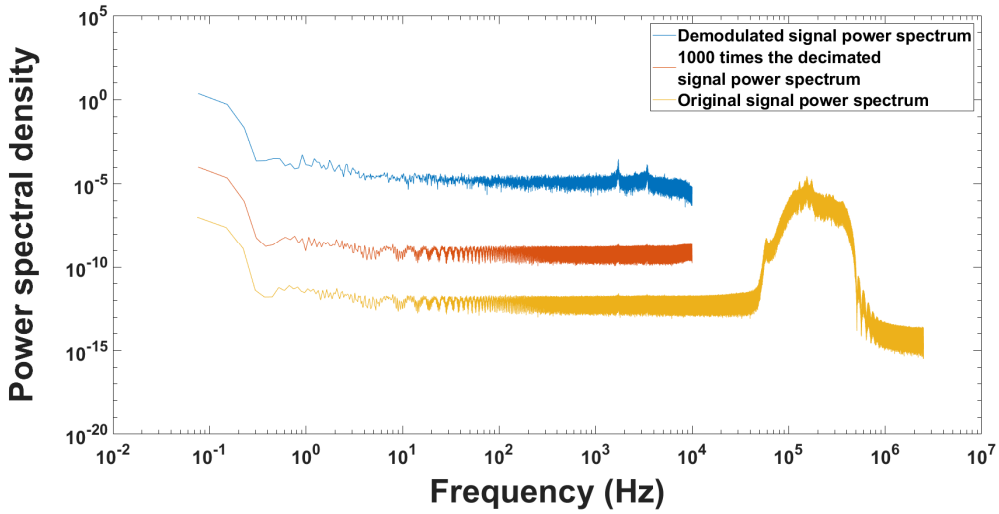


**Figure 15.** Comparison of the original, the decimated and the demodulated signal spectra. The decimated signal was multiplied by 1000 only for visualization purposes, and in reality, it would overlap almost perfectly with the original signal spectrum. All spectra were calculated using Welch's method.

The peaks in the low frequency range are well recognizable from the demodulated and decimated spectrum. The original spectrum and the decimated spectrum do still contain the same peaks, but they are so vague that it would be uncertain to attempt the detection of the shedding frequency from them. Figure 16 is the detailed observation of the peak frequencies, assumed to be the cavitation cloud shedding frequency and its first harmonic frequency.

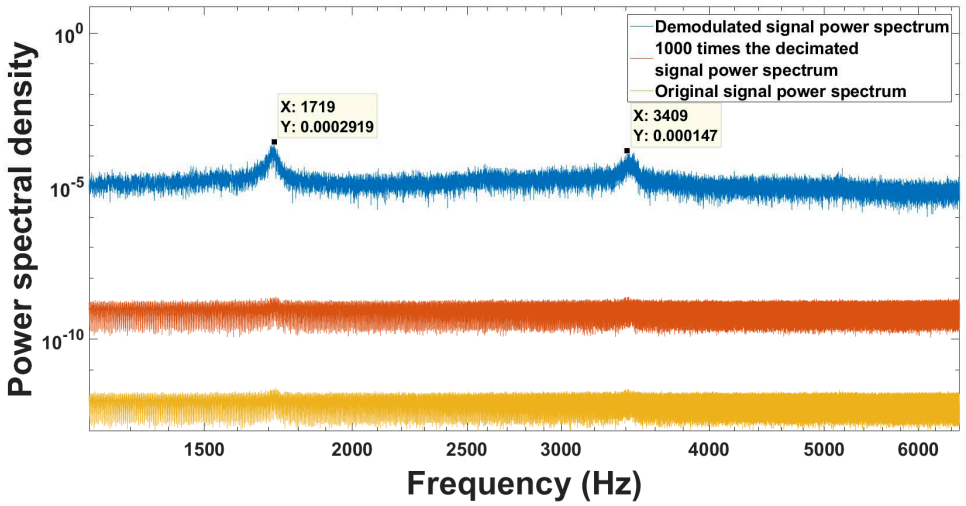


**Figure 16.** Comparison detail of the original, the decimated and the demodulated signal spectra.

The decimation process includes the low-pass filtering of the original signal. It is clear from the previous figures that this is an insufficient approach, while the demodulation, which is effectively enveloping combined with decimation, provides good results in terms of promoting low frequency contents. This was the approach in Publication IV, also described in section 5.4.

# 4 METHODOLOGY AND EXPERIMENTS

## 4.1 The PREVERO Cavitation Tunnel

All the main results in this thesis were obtained from experiments with the PREVERO cavitation tunnel that is situated in the LEGI laboratory, in Grenoble, France (PREVERO 2018). The tunnel is mostly utilized in cavitation erosion testing, in either short-duration pitting tests, or long-duration erosion tests. The duration of the tests is highly dependent of the specimen material and the tunnel operation point. The tunnel circulates water through a test section, with the possibility to control the pressure downstream of the test section by a pressurized nitrogen tank and upstream by a pump that has a frequency regulator to control rotation speed. The tunnel operation is thoroughly explained in Publications II, III and IV, and in (Franc 2009; Ylönen 2016). This section, however, also explains the basic operation.

The material specimens are 20 mm thick and 100 mm diameter cylinders that have a polished circular face towards the flow. The other face is towards the specimen holder, and it has a screw thread for fixing it to place. A 16 mm diameter nozzle feeds water to the test section that is a radially diverging channel of 2.5 mm thickness. The water jet from the nozzle stagnates in the middle of the material specimen and the water flow turns 90 degrees and begins to flow in all directions in the plane. Cavitation inception occurs as the flow cross-section area drops to 62.5 % at 8 mm radius, where the nozzle ends and the 2.5 mm thick channel begins. As the channel further diverges and the cross-section area increases, the static pressure also increases and the formed cavitation clouds collapse and damage the sample, in the area between 19 mm and 32 mm radius.

The flow velocity in the cavitating area and in the nozzle are major contributors to the aggressiveness of the cavitation field. The relevant velocity is the reference velocity calculated from the Bernoulli equation, assuming that the pressure inside the cavitation cloud is the vapor pressure. The vapor pressure is negligent compared to the upstream pressure, so the cavity velocity $V_c$ may be calculated from: (Franc 2009)

$$V_c \approx \sqrt{\frac{2p_u}{\rho_w}} \quad (8)$$

where $p_u$ is the upstream pressure of the tunnel and $\varrho_w$ is the water density. The erosion tests were conducted with a 4 MPa upstream pressure in this thesis, which is the maximum allowed pressure. This corresponds to approximately 90 m/s cavity velocity. The 2 MPa upstream pressure used in the other pitting test corresponds to a cavity velocity of about 63 m/s. (Franc et al. 2012) reported the following dependency between coverage time $\tau$ and cavity velocity $V_c$:

$$\tau \sim V^{-6.5} \quad (9)$$

The coverage time is the theoretical time that would be taken for a surface experiencing cavitation to be totally covered once by non-overlapping pits. In practice, it is calculated through a pitting test where only separate pits are formed. For example, if a surface would be covered 10 % in area with pits in 2 minutes, the coverage time would be 20 minutes. The coverage time is linked to the erosion rate, the exact relation being dependent on the cavitation erosion test setup (Hammitt 1979; Zhou & Hammitt 1983; Franc 2009). For this thesis, it is sufficient to estimate the aggressiveness to have roughly the same dependency as the coverage time. As the cavity velocity is dependent of the square root of the upstream pressure, the coverage time is dependent on the upstream pressure as:

$$\tau \sim \left({p_u}^{-6.5}\right)^{0.5} = {p_u}^{-3.25} \quad (10)$$

The 4 MPa upstream pressure is double the 2 MPa upstream pressure. Therefore, it has a coverage time of $2^{-3.25} \approx 0.11$ times the coverage time of the 2 MPa pressure. This means that the 4 MPa operation point is about 10 times more aggressive than the 2 MPa operation point. The cavitation number in the tunnel is defined as:

$$\sigma = \frac{p_d - p_v}{p_u - p_d} \quad (11)$$

where $p_d$ is the downstream pressure and $p_v$ is the saturated vapor pressure. Generally $p_v$ is negligible and therefore left out from the calculation. A constant cavitation number, regardless of the pressure levels, leads to same type of cavitation and the same closure point in the diverging channel (Gavaises et al. 2015). The

cavitation number is related to the occurrence of cavitation and it has no well-defined connection with the erosive potential.

## 4.2 Acoustic Emission Setups

The choice of acoustic emission setup has a large influence on the applicability of the results. In this thesis, the most important functionality was the recording of long full waveforms with a high sampling frequency. The most important results in Publications III and IV rely on waveforms recorded continuously for up to 6 minutes, with 5 MHz sampling frequency per sensor, and with two sensors. For the resonance type sensor, which had bandwidth of 100 kHz to 400 kHz, the sampling frequency was overly sufficient. The broadband sensor had a bandwidth of 100 kHz to 900 kHz, but in the upper range, no significant information was found. Therefore, probably the same results would have been obtained using for example a 2 MHz sampling frequency.

The initial setup used in (Ylönen 2016) was an IOtech WaveBook/512, which is a system having a 12-bit voltage resolution and a maximum sampling frequency of 1 MHz. One of the main limitations in that system was the limited acquisition time of 30 seconds with the maximum sampling frequency, after which the system required several minutes to save the data. The other severe limitation was that the signal tended to saturate, as cavitation induced a much higher AE signal than in the usual applications that the system was designed for. The original fix for this was to utilize a 550 kΩ resistance in the signal electrical circuit. This is a highly suspicious way to control the saturation problem, as the additional resistor might modify the signal shape with no true possibilities to estimate how. Fortunately, a new acquisition system solved both the problems.

The setup used in all the results listed in this thesis was a PAC PCI-2 acquisition system. It had an 18-bit voltage resolution and a maximum sampling frequency of 40 MHz. Continuous waveform acquisition was possible with either 10 MHz sampling with one sensor, or divided to two sensors, 5 MHz each. The sensors had PAC 2/4/6 preamplifiers, with the 20 dB amplification option always chosen for these measurements. The acquisition system had a PCI express connection to a 1 TB SSD hard drive, allowing direct saving to the drive. The practical upper limit to the size of waveform files was about 7 minutes, as overly large stream files were

unpractical to open in post-processing. This was solved by taking for example subsequent 30-second streams. The signal saturation problem was solved through the option of having smaller amplifications and larger range in the system. Signal attenuators of 40 dB (signal strength divided by 100) were also tested, but in the end, they were not required, as the signal upper values were below the saturation limit.

The sensor used for measurements in Publications I and III was the resonance type sensor PAC R15. A broadband sensor PAC LNWDI was also tested, but it broke down due to the vibrations caused by the cavitation tunnel. It was larger, as it had a built-in preamplifier, and it was more rigidly fixed to the material specimen than the other sensor. The sensors had to be fixed to the specimen with the aid of a waveguide that was a steel rod with the sensor fixed to it by a spring load (R15) or by glue (LNWDI). The waveguide was fixed to the sensor by a screw thread. The screw thread had a 90° countersink to enhance the wave transfer from signal source to sensor. Grease was applied to all interfaces to decrease wave attenuation. Figure 17 is the photograph of the two waveguide setups, with the sensors included.


**Figure 17.** Two options for the waveguide setup. A) The failed LNWDI sensor and B) the one used in most tests, with a regular size sensor fixed inside the waveguide, and another similar sensor outside the casing.

The sensors in Publication IV were a PAC R15D resonance type sensor and a PAC D9203B broadband sensor. The R15D differs from the R15 in Publication III only by its differential voltage measurement. The frequency response was virtually the same, with about 160 kHz resonance frequency. The D9203B was a differential

sensor as well, with a relatively flat response from 100 kHz to 900 kHz. They were both small sensors, similar in appearance than those in Figure 17B.

## 4.3 Contact profilometer

The requirements for the profilometer measurements differ in the erosion tests and in the pitting tests. The pitting tests require the measurement of a continuous surface, as large as practically possible. Therefore, they are more demanding than the erosion tests that require only one-dimensional measurements. For the results in Publications II and IV, the erosion profiles were measured using a contact profilometer able to measure 1-D profiles and limited size 2-D profiles. Due to the limited surface size of the contact profilometer, the results in the pitting tests in Publication III were obtained using an optical profilometer able to cover the whole cavitation closure area.

The contact profilometer (Form Talysurf 50, Taylor Hobson) had a planar resolution of 1 μm x 0.5 μm, and a theoretical depth resolution of 3.2 nm. Figure 18 is a photograph of the profilometer measuring a specimen profile. The profilometer tip was a 90° cone, with a 2-μm radius sphere in its end. The profiles were measured in the radial direction, and five parallel profiles were measured each time. The parallel profiles were 1 μm apart and they were measured to exclude the effects of possible local anomalies. The average of the five profiles represented each measurement. For each time step in the erosion process, the profiles were measured along eight radial lines, called azimuthal angles, from the specimen center. The process involved turning the sample manually between measurements.

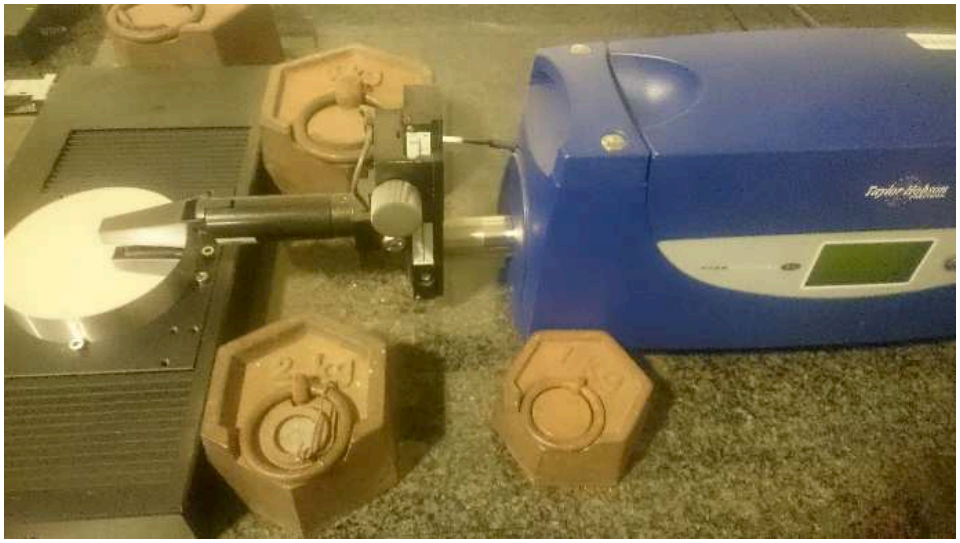

**Figure 18.** The contact profilometer measuring a specimen profile. The stainless steel specimen is in the left and the profilometer measures the radial profile.

The result was eight profiles per time step, a full erosion test having about 15 time steps in this thesis. From an erosion profile, such as in Figure 5, the surface loss may be calculated as a sum of the depth values multiplied by the radial resolution:

$$A_{loss}(t_n) = A_e(t_n) - A_e(t_0) = \sum_{i=1}^{m} s_r\{h_m(r,t_n) - h_m(r,t_0)\} \quad 12$$

where $A_{loss}(t_n)$ is the loss of area at a time instance, $A_e(t_n)$ is the area of the profile, $A_e(t_0)$ is the area of the profile before any erosion, $s_r$ is the resolution in the radial direction, 0.5 μm in this thesis and $h_m(r,t_n)$ is the depth at a certain radial location and time instance. The volume loss representing a profile was chosen to be the equivalent volume loss, if the whole sample would have exactly the same profile. As the measurement is along a radial line, the circumference of the specimen is dependent on the radial location of the measurement point. Therefore, the volume loss is calculated as:

$$V_{loss}(t_n) = V_e(t_n) - V_e(t_0) = \sum_{i=1}^{m} 2\pi r s_r\{h_m(r,t_n) - h_m(r,t_0)\} \quad 13$$

where $V_{loss}(t_n)$ is the volume loss at a given time instance, $V_e(t_n)$ is the volume of the profile and $V_e(t_0)$ is the volume of the profile before any erosion. The volume losses were averaged for the final results over all the sample azimuthal angles. Volume loss rate was calculated by dividing the volume loss difference by time passed between two measurements.

## 4.4 Optical profilometer

The contact profilometer was found to be efficient in the erosion profile measurements, as described in section 4.3. In measuring pitting patterns, the practical maximum area was about 4 mm x 4 mm with a 1 μm x 1 μm resolution measurement grid. An optical profilometer (Alicona Infinitefocus G5) was also available and it had the possibility of scanning larger areas than these. Using a 3.5226 μm x 3.5226 μm measurement grid, the entire impacted area of the specimen could be measured. What was lost in resolution was gained in covered area. It was also found that in the pitting tests, the pit coverage rate was not axisymmetric, as visualized in Publication III. As the AE measurements are assumed to detect all cavitation impacts, detecting all pits in the specimen was beneficial in determining the relation between AE and pit diameters.

The basic functionality of the optical profilometer is that it has a charge-coupled device (CCD) camera combined with a microscope. The specimens were illuminated by a white light source and the reflected light revealed the surface topology. Changing the vertical focal position enhanced the images, making them sharper. As the surface was initially polished, the profilometer failed to measure the depth values of the non-eroded surface. Fortunately, the pits were well captured, as they were less reflective and they had distinguishable shapes.

The profilometer generated text files that contained the depth information along with location of all the measured points, but it excluded the non-eroded points that were not captured. As the code to detect pits from the surface expected continuous measurement data, the non-eroded areas had to be interpolated between successive measured points. After the interpolation process, the surface was divided into rectangles of less than 1 $mm^2$, with shapes as close to a square as possible. This was done to reduce file size and to rectify locally the surface to be horizontal. The whole specimen was slightly curved, so rectifying the specimen plane at once to be horizontal would not work. A local plane rectification of each small area led to virtually no error.

After the profilometer-generated surface profiles were rectified and modified to be compatible with the pit detection code, each pit was detected and characterized. The pit detection code was used to analyse the less than 1 $mm^2$ surfaces. It required a user defined depth threshold, which was chosen as 0.5 μm, following the example

of (Franc 2009). The pit detection code then calculated the mean depth level and detected areas that were more than the depth threshold below the mean level. The image generated with these definitions was turned to binary. A disk with a radius of two pixels was used as the structuring element of morphological closing of the image. After these steps, the pit boundaries were detected and pit surface area, maximum depth, volume, and circularity were calculated. The circularity is a parameter that defines a shapes closeness to circle. This was used to omit scratches, which have a much lower circularity than pits caused by cavitation impacts. After the detection of pits, the pit depths were corrected by calculating the non-eroded surface level and adding it to the pit depths calculated initially. All the data were treated in Matlab®.

## 4.5 Microscopy and EBSD

The erosion rate tests answer the question of how the materials compare in their cavitation erosion resistance. They however do not answer the question of why. Between very different materials, this might be answered easily. For example, it is expected that a soft plastic would be inferior to stainless steels, as its mechanical strength is in every way inferior. Pure aluminum is also weaker than stainless steel in most ways, as also in its resistance to cavitation. However, comparing two stainless steels with a similar yield stress and other macroscopic mechanical properties, but with differing erosion rates, requires studies that are more advanced. This was the case with the stainless steels in this thesis, as explained more in section 5.1 and in Publications II and V. Publication II included also the erosion testing of a low-alloy steel, which was compared to others in erosion rates, but was not interesting enough to properly study its microstructure.

The first approach was to film the eroded and non-eroded specimen surface by SEM. The SEM images provided insight on the erosion process, but they were alone insufficient in determining the differences between two materials that are similar in many ways. The SEM imaging of the eroded material surface was studied in Publication II. The SEM image analysis, however, did not provide the reasons behind the erosion rates. In the next step, which could have as well been the first one, the stainless steels specimens were etched and imaged through conventional microscopy.

Optical microscopy revealed that both the stainless steels had a martensitic microstructure, with small amounts of precipitates. The optical microscopy allowed determining the prior austenite grain size of steel 1, but not of steel 2. This information was still not totally sufficient in answering the question of why steel 1 is so much stronger against cavitation. The third tool in searching this information was SEM imaging combined with electron backscatter diffraction (EBSD). These results are presented in section 5.2 and in Publication V.

SEM combined with EBSD enables the determining of grain orientations inside individual grains. Phase identification is also possible, along with other useful features not relevant to this thesis. The method is thoroughly explained in (Schwarzer et al. 2009). EBSD generates diffraction patterns that allow grain orientation and phase detection. The resolution is relatively good and the method may be automated in many cases. The effective determination of grain orientations and phases required an automated algorithm developed by (Nyyssönen et al. 2016; Nyyssönen 2017). The detailed understanding of the EBSD method along with the algorithms were out of the scope of this thesis, as the expertise of the author is too limited for these methods. The difference between these three microscopy methods are compared in Figure 19.

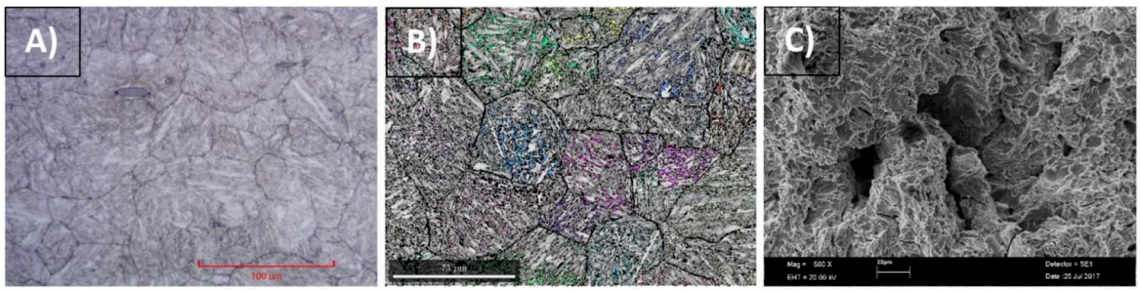


**Figure 19.** Comparison of the three different microscopy methods: A) Optical microscopy, 200 X magnification, B) SEM with EBSD mapping of the prior austenite orientations, 500 X magnification, and C) SEM image with a 500 X magnification of the eroded surface.

The optical microscope image reveals the prior austenite grains and precipitates, for the steel in Figure 19, but the EBSD image contains more explanations for defining the reasons behind differing erosion rates. The SEM images from the eroded region, without EBSD, provide only qualitative information of the erosion process, and they are insufficient in determining the true reasons behind the erosion rates. More detailed images and descriptions are presented in Publications II and V.

# 5 MAIN RESULTS

## 5.1 Cavitation Erosion Resistance

The cavitation erosion resistance of a material may either be:

1. The materials capability to resist the onset of material loss. A resistant material has a long incubation time, which is defined as how long it takes to the process being dominated by material loss rather than plastic deformation; or

2. The materials capability to resist material loss when the erosion has reached a relatively steady state of impacts leading to rupture, material loss and revealing of new material surface. The erosion rate may either be defined as volume and mass loss or as the rate of penetration depth.

It is often considered that these two are closely connected, as they are parameters that are inherited from the materials mechanical strength. No single or easily definable mechanical parameter is sufficient in predicting the incubation time or the erosion rate with good accuracy. The yield stress and the ultimate stress, along with hardness, have generally a good correlation to erosion resistance when comparing metals, but this was not true for example comparing a low-alloy steel and an aluminum alloy in (Ylönen 2016). An important phenomenon is also that highly elastic materials, such as plastics or rubbers, may resist cavitation extremely well due to the attenuation of the impact loads when the material strains. This could be interpreted as the material escaping the loading and thus increasing the impulse time and reducing the true stress. This is exceptionally true for example for UHMWPE coatings that exceeded the erosion resistance of high quality stainless steels in (Deplancke et al. 2015).

In this thesis, the incubation times were not studied in detail, and the erosion resistance was defined through volume loss of the specimens. The volume loss was considered a suitable parameter, as it defined the damage the entire cavitation field

induces to the specimen. The penetration depth would have been an equally representative parameter and it was used in tests with the same cavitation tunnel for example in (Franc 2009).

Cavitation erosion resistance may be defined as the inverse of the erosion rate: a material with a low erosion rate exhibits a good resistance to cavitation. It was observed that the shape of the erosion pattern differed slightly between materials, as presented in Figure 20. This was the main reason to compare rather the volume losses than the erosion depths.

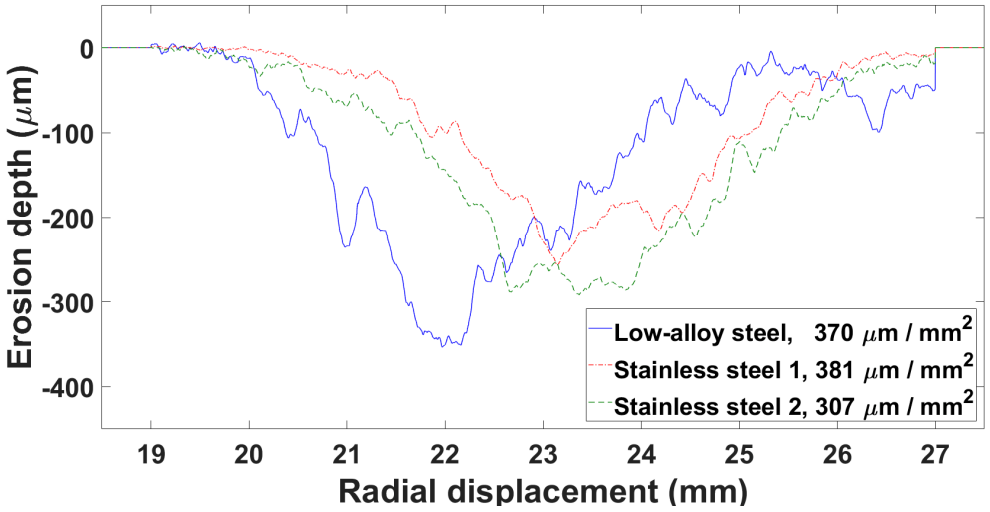


**Figure 20.** Average erosion patterns of three different steels. The exposure times were 25 hours for the low-alloy steel and 65 hours for both stainless steels. The erosion depth divided by eroded cross-section area highlights the differences in erosion shape.

The ratio of the erosion depth to the eroded area is significantly different for stainless steel 2, compared to stainless steel 1 and low-alloy steel. The profiles are the averaged profiles of all the different azimuthal angles, so they do not represent any of the actual measured profiles. However, the average profiles are useful in comparing the overall differences in the shape of the erosion pattern. Additionally, the minimum depth location differs between low-alloy steel and the stainless steels. The differences in profiles were also observed in the panorama SEM images in Publication II.

In addition to the differences in profile shape, the specimens experienced different erosion rates depending on the sample azimuthal angle. This is most probably not due to possible differences in the cavitation field that the tunnel produces. To begin with, the cavitation field may be assumed axisymmetric if the

feed nozzle is not overly damaged. Additionally, the specimens were turned 90 degrees after every time that they were removed from the tunnel for profile measurements. Therefore, the discrepancies in the cavitation field from axisymmetric shape would be negated in the end. The volume losses for the three studied materials, with all the azimuthal angles, are plotted in Figure 21.

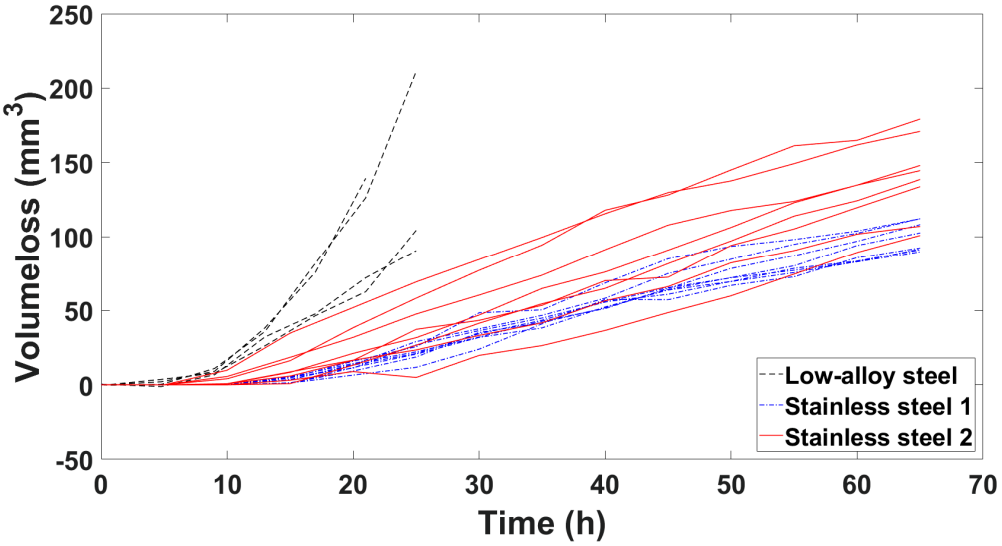


**Figure 21.** Volume loss dependency on azimuthal angle. The azimuthal angle is explained in section 2.4.

As the plots overlap significantly, it would be difficult to mark the azimuthal angles in the figure. Therefore, the final volume losses are presented in Table 1. Its main purpose is to support Figure 21, as the volume loss rates in Table 2 represent better the erosion resistances of the materials.

**Table 1.** Final volume loss values for the erosion tests as a function of the azimuthal angle. The angle represents the measurement direction in relation to the one defined to be at 0° angle.

| Material | 0° $mm^3$ | 45° $mm^3$ | 90° $mm^3$ | 135° $mm^3$ | 180° $mm^3$ | 225° $mm^3$ | 270° $mm^3$ | 315° $mm^3$ |
|---|---|---|---|---|---|---|---|---|
| Low-alloy steel | 211.2 | | 90.5 | | 139.4 | | 104.2 | |
| Stainless steel 1 | 89.7 | 92.3 | 102.5 | 112.2 | 91.0 | 91.6 | 112.1 | 108.1 |
| Stainless steel 2 | 179.2 | 144.5 | 148.0 | 138.5 | 170.9 | 100.7 | 133.7 | 106.9 |

The volume loss rate is difficult to estimate directly from the figure. It could be interpreted that the volume loss curves just have a different offset, depending on the incubation period length of each angle. However, as explained in Publication II, the rates do differ significantly. Table 2 presents the erosion rate dependency on azimuthal angle, and the average erosion rates of all the three materials.

**Table 2.** Erosion rate dependency on specimen azimuthal angle. The angle represents the measurement direction in relation to the one defined to be at 0° angle.

| Material | 0° $mm^3$ /h | 45° $mm^3$ /h | 90° $mm^3$ /h | 135° $mm^3$ /h | 180° $mm^3$ /h | 225° $mm^3$ /h | 270° $mm^3$ /h | 315° $mm^3$ /h | Mean $mm^3$ /h |
|---|---|---|---|---|---|---|---|---|---|
| Low-alloy steel | 11.62 | | 5.44 | | 12.38 | | 3.63 | | 8.95 |
| Stainless steel 1 | 1.40 | 1.70 | 2.02 | 2.24 | 1.52 | 1.58 | 2.30 | 2.21 | 1.79 |
| Stainless steel 2 | 4.02 | 2.94 | 3.02 | 2.95 | 3.56 | 2.66 | 2.43 | 2.27 | 2.72 |

These differences were explained to result from local differences in the material microstructure in Publication II. The mean erosion rates were also compared to several other materials measured by other researchers in the same cavitation tunnel. An interesting detail is that stainless steel 1 was from a turbine manufactured in the 1970's, while stainless steel 2 was from a modern turbine manufactured in 2010's. The reasons behind the differences were identified in Publication V.

## 5.2 Microstructure and Erosion Resistance

The low-alloy steel had a significantly higher erosion rate, probably due to the combined effect of oxidation and cavitation erosion, along with its inferior mechanical properties. The oxidation process weakens the materials surface against cavitation impacts that in turn expose new non-oxidized surface, thus increasing oxidation rate (Kwok et al. 2006; Ryl et al. 2011). The SEM images in Publication II were insufficient for finding the true reason behind the differing erosion resistances of the two stainless steels. The main result from them was that the erosion process is probably low-cycle fatigue. Typical to this type of fatigue, examples were found of crack front propagation, with "beach-marks" marking the successive positions of the crack front. The crack propagation of this type is illustrated in Figure 22.

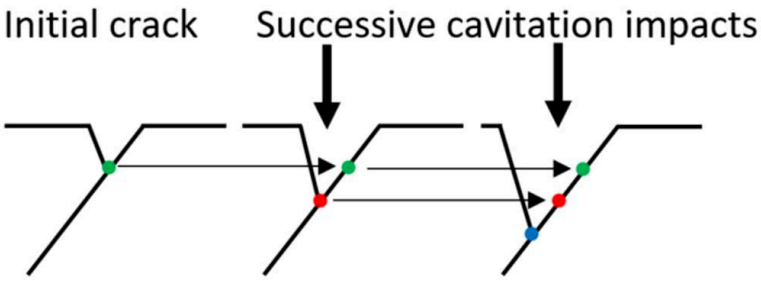


**Figure 22.** Crack propagation in low-cycle fatigue.

Low-cycle fatigue is expected from cavitation erosion processes with high impact loads (Fortes Patella et al. 2013). Low-cycle fatigue occurs when the impacts lead to plastic deformation and the crack fronts advance rapidly (Bathias & Pineau 2010). In low-cycle fatigue, the amount of cycles is in the order of few to some tens.

The first observations providing insight into the reasons behind erosion resistance was the optical microscope images. The material specimens from the erosion tests were cut to pieces so that the cross section of the eroded surfaces was accessible. The cross section surfaces were polished and etched before microscopy. Stainless steel 1 revealed its prior austenite grains, while stainless steel 2 did not. Both of them were identified as martensitic stainless steels. Images are available in Publication II.

The prior austenite grain size has an effect on the impact strength and plasticity of martensitic steels (H. J. Kim et al. 1998; Zavaleta Gutiérrez et al. 2013). From the optical microscope images, it could be estimated that stainless steel 2 has a larger prior austenite grain size. The estimate was based on the apparent martensite lath structure orientation. This estimate however lacked proper proof, so the advanced approach of SEM combined with EBSD was taken. It was efficient in determining the martensite block and packet sizes and their orientations, along with prior austenite grain sizes.

The EBSD measurements proved that stainless steel 1 had a significant amount of retained austenite in the microstructure. It also had a significantly smaller packet and block sizes, as well as a smaller prior austenite grain size. The retained austenite fraction was up to 9 vol - % for steel 1, while it was zero for steel 2. The retained austenite may transform to martensite through cavitation impacts. This was observed in the edge regions of steel 1, in the about 200-μm transition region from the edge to bulk material. In the edge, where erosion has significantly hardened the

material, all the austenite had transformed to martensite. The transition region depth correlates well with that measured by (Berchiche et al. 2002), who measured the hardened layer by micro-hardness measurements for a 316L specimen that had experienced cavitation erosion.

The interesting thing about the microstructure of steel 1 is that it resembles that of steels that have been processed by quenching and partitioning (Q&P). The Q&P process was not a known process, according to (Edmonds et al. 2006), before 2006. However, steel 1 was from a turbine manufactured in the 1970's. This indicates that the Q&P microstructure was perhaps accidentally achieved for the steel, or that some other treatment has provided a similar microstructure. The further analysis of these factors are far beyond the scope of this thesis. It may be however concluded that the microstructure for stainless steel 1, presented in Publication V, is a desired one in manufacturing cavitation resistant steels.

## 5.3 Defining Cavitation Intensity by Acoustic Emission

The main result in this thesis relating to the estimation of the impacts strengths was discussed in Publication III. Publication I presents the basic principles in utilizing AE in cavitation testing and in using the enveloping method to detect peaks and determine their amplitudes. Publication III combined this information to pit distributions and presented a correlation between AE peak voltage value and pit diameter. The cumulative pit diameters and the peak voltage values both had a long linear range in the linear – logarithmic scale. Normalizing pit diameters with the reference pit diameter, explained in section 2.3, and then normalizing also AE peak voltage values with the reference peak voltage value led to almost overlapping cumulative distributions. When corrected by first subtracting the cut-off voltage from the voltage values, the distributions overlapped almost perfectly. The normalized, overlapping cumulative distributions are presented in Figure 23. The voltage values below the cut-off limit were omitted, as they are assumed to be either from noise or from non-damaging impacts.

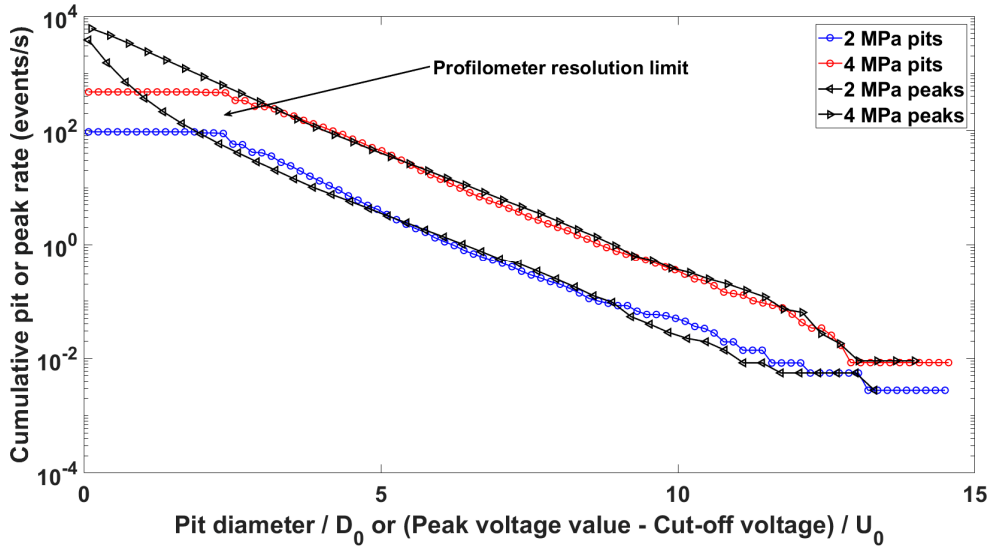


**Figure 23.** Pit and peak cumulative distributions. The normalization causes the curves to overlap to a high degree. The pit diameters and peak voltage values were arranged into bins, with the same bin sizes as in Figure 3 and Figure 8.

These results were already thoroughly discussed in Publication III, where it was stated that pit diameter distributions could be estimated from AE, using the following relation:

$$\frac{D}{D_0} = \frac{U - U_{cutoff}}{U_0} \qquad 14$$

In this section, this relation is used to simulate pit diameter distributions from imagined AE distributions, as the only measured AE distributions are those already presented. The parameters $D_0$, $U_0$ and $U_{cutoff}$ were found to remain virtually constant between the 2 MPa and the 4 MPa upstream pressures. Only the parameters $\dot{N}_{0,peak}$ and $\dot{N}_{0,pit}$ change, depending on the aggressiveness of cavitation. They determine the intersection of the Y-axis in the cumulative distributions.

Here, it is assumed that one would have AE peak voltage distributions from the cavitation tunnel, but no way to measure the pit diameter distribution. This would correspond to measuring AE in an operating hydraulic machine and attempting to know what happens inside without any access to the eroding surface. The pit diameters have a correlation between the impact loads and thus cavitation intensity, but this correlation is not clear and is not discussed further, as the expansion from laboratory results to hydraulic machines is out of the scope of this thesis.

The relation between coverage time and upstream pressure was already presented in equation 10. An assumption is made that the reference peak rate $\dot{N}_{0,pit}$ follows a similar law. The exponent is not exactly the same, if calculated from the reference pit rates in Table 3. The power law may be expressed here as:

$$\dot{N}_{0,pit} \sim {p_u}^{3.34} \quad 15$$

The exponent 3.34 is close to the exponent 3.25 in equation 10. The difference is so small that further measurements might prove that it is only due to lack of a large number of tests. However, assuming that the relation in equation 15 holds true, the simulated reference pit rates may be listed in Table 3.

**Table 3.** Reference values and simulated distribution values for the connection between peak voltage values and pit diameters.

| | 2 MPa, measured | 4 MPa, measured | Average | 1 MPa, simulated | 1.5 MPa, simulated | 3 MPa, simulated |
|---|---|---|---|---|---|---|
| $U_{autoff}$ (V) | 0.045 | 0.062 | 0.054 | 0.054 | 0.054 | 0.054 |
| $U_0$ (V) | 0.064 | 0.065 | 0.064 | 0.064 | 0.064 | 0.064 |
| $D_0$ (µm) | 6.17 | 6.08 | 6.13 | 6.13 | 6.13 | 6.13 |
| $U_0/D_0$ (V/µm) | 97.28 | 94.22 | 95.75 | 95.75 | 95.75 | 95.75 |
| $\dot{N}_{0,pit}$ (1/s) | 598 | 6070 | - | 59 | 229 | 2320 |
| $\dot{N}_{0,peak}$ (1/s) | 1232 | 15958 | - | - | - | - |

With the parameters in hand, the simulated peak voltage distributions can be plotted using equation 6. Additionally, the pit distributions can be plotted using equation 3. These distributions are presented in Figure 24.

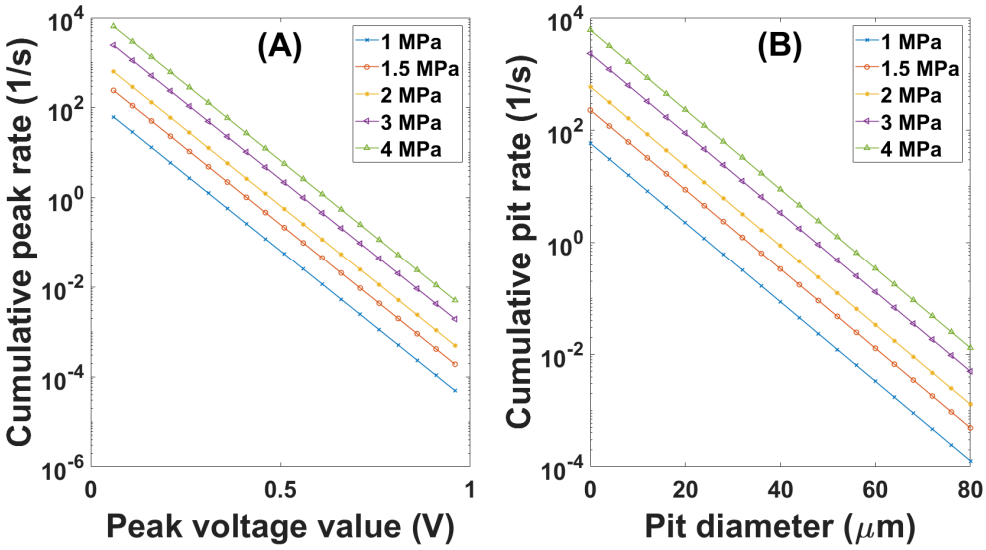


**Figure 24.** Simulated peak (A) and pit (B) distributions for several cavitation tunnel upstream pressures. The scale is linear – logarithmic.

The cumulative rates estimated in this manner require the exponential relation in the reference pit rate to be true. This is however not required, if there are AE measurements available for different cavitation intensities. This would be the case in an imagined hydraulic machine monitoring system. This type of approach relies in the measurement of AE and pit diameter distribution in the machine, be it a cavitation tunnel or a hydraulic machine, at least at one operation point. It requires the assumption that the reference parameters and the cut-off voltage are not dependent on operation point, as it was in the cavitation tunnel. In the tunnel, the cavitation type remains the same as long as the cavitation number stays the same. This thesis does not have an answer if these relations would still hold true and be applicable, if the cavitation number would change. It is implied that AE peak voltage values would be directly linked to the damage potential and pit diameter the cavitation impacts induce, but no further verification is available.

## 5.4 Tracking Cavitation Erosion via Shedding Frequency

In this thesis, the changes in cavitation cloud shedding frequency were found to correlate with evolving cavitation erosion. AE was found to detect the shedding frequency robustly, as explained in section 3.6. A method to track the erosion evolution via AE measurements, which do not require direct access to the eroding surface, was presented in Publication IV. The AE methods capability of detecting

the shedding frequency was confirmed by comparing the frequencies to those obtained through video analysis and those from simulated results by (Gavaises et al. 2015). The frequencies correlated well for a range of cavitation numbers, from $\sigma = 0.87$ to $\sigma \approx 1.8$. For values above 1.8, the cloud cavitation phenomenon began to disappear, and the cavitation transitioned to sheet cavitation, which is not possible to characterize through shedding frequency as it lacks periodic growth and collapse cycles. With the proof that AE properly catches the shedding frequency, if properly treated as explained in section 3.6, the AE data was utilized in connecting the shedding frequency to erosion evolution.

The cloud to sheet cavitation transition occurs when the Reynolds number or the cavitation number increases over a certain threshold. A transition region lies between clearly defined structures (Pelz et al. 2014; Pelz et al. 2017). The exact values of the dimensionless numbers depend on the flow geometry and the flow medium. The transition region lies somewhere between $\sigma = 1.5$ and $\sigma = 1.9$ in the operation conditions in Publication IV. This is clear from the video analysis, and it is also observed in AE measurements and in the simulations by (Gavaises et al. 2015).

Surface roughness has been demonstrated to increase the cloud shedding frequency (Hao et al. 2017). The erosion process in the cavitation tunnel can be compared to the increase of roughness. When the initially mirror-polished surface begins to erode, it first turns “frosty”, after which material loss begins to occur. In the end of the test, when the maximum erosion depth is about 0.5 mm, erosion is so pronounced that it could be described as transformed channel geometry rather than roughness. The change in the shedding frequency is connected to the change in vorticity of the flow. In Publication IV, the evolution of the shedding frequency was plotted against time, with another plot for the erosion evolution. In Figure 25, the X-axis is changed to erosion volume.

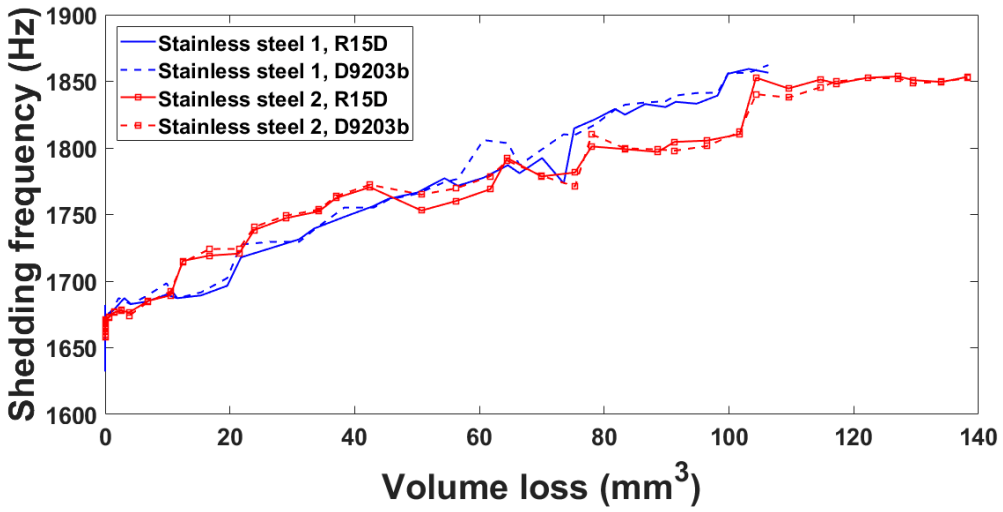


**Figure 25.** Shedding frequency as a function of eroded volume.

When the erosion time is changed to volume loss, the plots for the two materials overlap significantly. For stainless steel 2, which experiences more total erosion, the shedding frequency begins to remain constant independent of the erosion volume, after the about 100 $mm^3$ limit. This would probably be observed for stainless steel 1 as well, but unfortunately, the test was ended too soon to confirm this. The two stainless steels have significantly different steady state erosion rates, as describes in Publications II, IV and V, so it may be concluded that the change in the shedding frequency indeed is a geometry and roughness related phenomenon. This means that the tracking of erosion evolution using the presented method is probably not dependent of the materials experiencing cavitation, as long as the cloud shedding frequency is captured via AE. This method could be used in hydraulic machine monitoring, if cloud cavitation occurs and if AE sensors could be placed so that they properly capture the shedding frequency.

# 6 CONCLUDING REMARKS

The research questions investigated in this thesis were listed in section 1.2. This section aims to evaluate what were the concise answers to these questions and if these answers are adequate. The thesis was divided into two main problems: characterizing erosive cavitation and tracking the evolution of cavitation erosion. The attempt to solve both problems included acoustic emission measurements in a cavitation tunnel. The used AE data was in the end similar in both approaches; it was just treated differently. Along with these results, knowledge was gained of the erosion properties of three Francis turbine steels used in runner blades. A secondary goal was to study if the microstructure-level reasons could be found behind the difference in erosion rates of two stainless steels that were studied.

The first research question concerned the cavitation erosion resistances of steels used in runner blades. This was studied through erosion tests in a cavitation tunnel and the main results were discussed in Publication II. Three materials were studied: A low-alloy steel and two stainless steels from different turbines. Stainless steel 1, which was from a turbine manufactured in the 1970's, performed the best from these three materials. It also compared well to other steels measured by other authors. The measure of cavitation erosion resistance was the steady-state volume loss rate. The lower this rate, the better the materials resistance. The volume loss rate was chosen over the mass loss rate, as cavitation damage is typically a volume-related problem, as the structural integrity of the machines degrade based on changes in geometry.

The second question of the reason behind the differing rates culminated in the microstructure analysis of the two studied stainless steels. These two steels had a martensitic microstructure, observed from the optical microscope images in Publication II. Steel 2, which was from a turbine commissioned in 2010's, and also performed worse that steel 1, seemed to have a larger prior austenite grain size. Optical microscopy did not reveal the accurate grain size, nor any other effects that might contribute to the difference. The SEM images from the eroded area in Publication II did not give any insight to this, and they only highlighted that the erosion process is dominated by low-cycle fatigue.

The EBSD measurements, presented in Publication V, provided an accurate answer to this question. Steel 1, while having a prior austenite grain size about half of that of steel 2, had other advantages as well. It had smaller martensite packet and block sizes, and most importantly, it had up to 9 vol-% of retained austenite, well dispersed between packets and blocks. This significantly increases the impact strength, and additionally, it enables an austenite – martensite transformation, contributing to strain-hardening and increased resistance. This transformation was observed in the edge regions where cavitation had damaged the specimens.

The third question was about detecting and characterizing individual cavitation impacts via AE. This method was first discussed in Publication I, where the AE enveloping and peak counting method was presented. The method was further developed and the results were compared to pitting measurements in Publication III. The cumulative distributions of both the AE peak voltage values and the cavitation pit diameters, measured through optical microscopy, had a clear correlation. A correlation was found between AE peak voltage value and the resulting pit diameter. This allows the estimation of pit distributions through AE measurements in the cavitation tunnel, using parameters that are AE setup and material dependent. The pit sizes are generally related to the cavitation impact strengths, but this relation was not further discussed in this thesis. The presented method was criticized in section 3.4, as impacts generated by dropping steel balls on the specimen surface was observed to produce varying AE voltages, depending on impact location. This does not prove the method false, as the ball drop test might not imitate cavitation impacts properly, as the specimens were not attached in the cavitation tunnel, nor did they create identical loadings compared to cavitation impacts. However, this effect should be further studied to remove doubt.

The fourth research question concentrated on the cavitation erosion tracking via AE. As the erosion progresses, the specimen surface both hardens and changes in geometry, through roughness and material loss. The main results were presented in Publication IV. Initially, parameters such as AE event energy and RMS value were studied as potential indicators of erosion, but they did not provide any clear results. The type of cavitation created in the tunnel is cloud cavitation, which is characterized by periodical formation and collective collapse of clouds of cavitation bubbles. The frequency of these events was assumed to be in the order of several kHz, which was far below the AE sensor operation range. However, it was found that the process of

demodulation may be used to promote these frequencies in the AE data, as they were modulated in the high frequency signal. The demodulated frequencies were compared to those from video analysis and to those from simulations by another author, thus proving that the AE effectively does capture the shedding phenomenon. It was observed that after the cavitation incubation period, the shedding frequency increases with increasing volume loss, until it reaches a quasi-stationary level.

In the author's opinion, these three results are the key findings of this thesis:

1) Martensitic steels with a small prior austenite grain size, a small packet and block size and a good fraction of retained austenite dispersed in the microstructure have a higher cavitation erosion resistance. This provides one way to rank martensitic steels regarding material choices in hydraulic machines.

2) The AE enveloping and peak counting method may be used in estimating cavitation pit diameter distributions.

3) Cloud cavitation shedding frequency increases with increasing volume loss, at least in a simple geometry as in the PREVERO cavitation tunnel, and the changes in the frequency may be tracked via high frequency AE measurements that are demodulated and low-pass filtered before transforming them to the spectral domain.

To conclude this thesis, the certainty of these three methods need to be discussed. The results in Publication V are rather well founded, so finding 1 is considered to have a high certainty and it could be used as a guideline for turbine manufacturers or operators commissioning turbines. The results in Publication III and the statement in finding 2 are less certain in the author's opinion, but they might provide insight in comparing cavitation intensity levels even in hydraulic machines. The method seems to perform well in the cavitation tunnel, but additional measurements with different operation points would be beneficial. Expanding it to hydraulic machines would require significant work. Finding 3 was considered to have a high certainty, as the results in Publication IV are consistent and they compare well with other methods. Expanding the method to measure erosion progression in hydraulic machines would require knowledge of the cavitation types in the machines. Without the periodicity in cloud cavitation, the method has no use. Therefore, in the limited

case of cloud cavitation and of transitioning from sheet to cloud cavitation, the method might prove highly efficient, even in hydraulic machines.

# REFERENCES


ACHENBACH, J.D. (1975). WAVE PROPAGATION IN ELASTIC SOLIDS, 1ST ED., NORTH HOLLAND PUBLISHING.

ACOSTA, A.J. & PARKIN, P.R. (1975). CAVITATION INCEPTION - A SELECTIVE REVIEW, JOURNAL OF SHIP RESEARCH, VOL. 19(4), PP. 193-205.

ARABNEJAD, M.H., AMINI, A., BENSOW, R. & FARHAT, M. (2018). EXPERIMENTAL AND NUMERICAL INVESTIGATION OF THE CAVITATING FLOWS OVER A MODIFIED NACA0009 FOIL, PROCEEDINGS OF THE 10TH INTERNATIONAL SYMPOSIUM ON CAVITATION (CAV2018), 2019/02, ASME, NEW YORK, NY, PP. 1-5.

ARNDT, R. (2014). FOREWORD, IN: KIM, K., CHAHINE, G.L., FRANC, J. & KARIMI, A. (ED.), ADVANCED EXPERIMENTAL AND NUMERICAL TECHNIQUES FOR CAVITATION EROSION PREDICTION, SPRINGER DORDRECHT HEIDELBERG, PP. V-VI.

ARNDT, R., VOIGT, R., SINCLAIR, J., PETER, R. & ANTONIO, F. (1989). CAVITATION EROSION IN HYDROTURBINES, JOURNAL OF HYDRAULIC ENGINEERING, VOL. 115(10), PP. 1297-1315.

ASTM G134-95(2010)E1, STANDARD TEST METHOD FOR EROSION OF SOLID MATERIALS BY A CAVITATING LIQUID JET (2010).

ASTM G32-10, STANDARD TEST METHOD FOR CAVITATION EROSION USING VIBRATORY APPARATUS (2010).

AURET, J.G., DAMM, O.F.R.A., WRIGHT, G.J. & ROBINSON, F.P.A. (1993). THE INFLUENCE OF WATER AIR CONTENT ON CAVITATION EROSION IN DISTILLED WATER, TRIBOLOGY INTERNATIONAL, VOL. 26(6), PP. 431-433.

AVELLAN, F. (2004). INTRODUCTION TO CAVITATION IN HYDRAULIC MACHINERY, THE 6TH INTERNATIONAL CONFERENCE ON HYDRAULIC MACHINERY AND HYDRODYNAMICS.

BATHIAS, C. & PINEAU, A. (2010). LOW-CYCLE FATIGUE, IN: FATIGUE OF MATERIALS AND STRUCTURES - FUNDAMENTALS, JOHN WILEY & SONS, PP. 113-116.

BERCHICHE, N., FRANC, J.-. & MICHEL, J.-. (2002). A CAVITATION EROSION MODEL FOR DUCTILE MATERIALS, JOURNAL OF FLUIDS ENGINEERING, VOL. 124(3), PP. 601-606.

BERRY, J.E. (1997A). HIGH FREQUENCY ENVELOPING AND DEMODULATION TECHNIQUES USING INSTRUMENTS FROM VARIOUS VENDORS, 1ST ED., TECHNICAL ASSOCIATES OF CHARLOTTE, P.C.

BERRY, J.E. (1997B). TRACKING OF ROLLING ELEMENT BEARING FAILURE STAGES USING BOTH VIBRATION SIGNATURE ANALYSIS AS WELL AS HIGH FREQUENCY ENVELOPPING AND DEMODULATION SPECIAL TECHNIQUES, 3RD ED., TECHNICAL ASSOCIATES OF CHARLOTTE, P.C.

BERTHELOT, M. (1849-1858). SUR QUELQUES PHENOMENES DE DILATION FORCEE DE LIQUIDES.

BOURDON, P., FARHAT, M., MOSSOBA, Y. & LAVIGNE, P. (1999). HYDRO TURBINE PROFITABILITY AND CAVITATION EROSION, WATERPOWER '99: HYDRO'S FUTURE: TECHNOLOGY, MARKETS, AND POLICY, 2018/11, PP. 1-10.

BRENNEN, C.E. (1995). CAVITATION AND BUBBLE DYNAMICS, 1ST ED., OXFORD UNIVERSITY PRESS, OXFORD, UNITED KINGDOM.

BRENNEN, C.E., COLONIUS, Y.C., WANG, A. & PRESTON, A. (2000). CLOUD CAVITATION PHENOMENA, TWENTY-SECOND SYMPOSIUM ON NAVAL HYDRODYNAMICS, PP. 239-253.

BRUJAN, E.A., KEEN, G.S., VOGEL, A. & BLAKE, J.R. (2002). THE FINAL STAGE OF THE COLLAPSE OF A CAVITATION BUBBLE CLOSE TO A RIGID BOUNDARY, PHYSICS OF FLUIDS, VOL. 14(1), PP. 85.

CARNELLI, D., KARIMI, A. & FRANC, J. (2012). APPLICATION OF SPHERICAL NANOINDENTATION TO DETERMINE THE PRESSURE OF CAVITATION IMPACTS FROM PITTING TESTS, JOURNAL OF MATERIALS RESEARCH, VOL. 27(1), PP. 91-99.

Carrat, J., Fortes-Patella, R. & Franc, J. (2017). Assessment of Cavitating Flow Aggressiveness on a Hydrofoil: Experimental and Numerical Approaches, ASME 2017 Fluids Engineering Division Summer Meeting, pp. V01AT05A013.

Caupin, F. & Herbert, E. (2006). Cavitation in water: a review, Comptes Rendus Physique, Vol. 7(9–10), pp. 1000-1017.

Chahine, G.L., Franc, J. & Karimi, A. (2014). Cavitation and Cavitation Erosion, in: Kim, K., Chahine, G.L., Franc, J. & Karimi, A. (ed.), Advanced Experimental and Numerical Techniques for Cavitation Erosion Prediction, Springer Dordrecht Heidelberg, pp. 3-20.

Chahine, G.L., Franc, J. & Karimi, A. (2014). Mass Loss and Advanced Periods of Erosion, in: Kim, K., Chahine, G.L., Franc, J. & Karimi, A. (ed.), 10.1007/978-94-017-8539-6, Springer Dordrecht Heidelberg, pp. 97-121.

Chahine, G.L. & Kalumuck, K.M. (1998). The Influence of Structural Deformation on Water Jet Impact Loading, Journal of Fluids and Structures, Vol. 12(1), pp. 103-121.

Chen, T., Liang, W., Zhang, M., Huang, B. & Wang, G. (2018). Cavitating Flows of Varying Temperature Liquid Nitrogen in Converging-diverging Nozzle, Proceedings of the 10th International Symposium on Cavitation (CAV2018), 2019/02, ASME, New York, NY, pp. 1-6.

Choi, J.-. & Chahine, G.L. (2015). Quantitative evaluation of erosive cavitation pressure field from pits in material: fact or myth? 9th International Symposium on Cavitation (CAV2015), pp. 1-4.

Deplancke, T., Lame, O., Cavaille, J., Fivel, M., Riondet, M. & Franc, J. (2015). Outstanding cavitation erosion resistance of Ultra High Molecular Weight Polyethylene (UHMWPE) coatings, Wear, Vol. 328–329, pp. 301-308.

Dular, M. & Osterman, A. (2008). Pit clustering in cavitation erosion, Wear, Vol. 265(5–6), pp. 811-820.

DULAR, M., STOFFEL, B. & ŠIROK, B. (2006). DEVELOPMENT OF A CAVITATION EROSION MODEL, WEAR, VOL. 261(5–6), PP. 642-655.

EDMONDS, D.V., HE, K., RIZZO, F.C., DE COOMAN, B.C., MATLOCK, D.K. & SPEER, J.G. (2006). QUENCHING AND PARTITIONING MARTENSITE—A NOVEL STEEL HEAT TREATMENT, MATERIALS SCIENCE AND ENGINEERING: A, VOL. 438-440, PP. 25-34.

ESCALER, X., EGUSQUIZA, E., FARHAT, M., AVELLAN, F. & COUSSIRAT, M. (2006). DETECTION OF CAVITATION IN HYDRAULIC TURBINES, MECHANICAL SYSTEMS AND SIGNAL PROCESSING, VOL. 20(4), PP. 983-1007.

FARHAT, M. & BOURDON, P. (1998). EXTENDING REPAIR INTERVALS OF HYDRO TURBINES BY MITIGATING CAVITATION EROSION, CEA ELECTRICITY '98 CONFERENCE AND EXPOSITION.

FORTES PATELLA, R., CHOFFAT, T., REBOUD, J. & ARCHER, A. (2013). MASS LOSS SIMULATION IN CAVITATION EROSION: FATIGUE CRITERION APPROACH, WEAR, VOL. 300(1), PP. 205-215.

FRANC, J. & MICHEL, J. (2005). FUNDAMENTALS OF CAVITATION, 1ST ED., SPRINGER SCIENCE + BUSINESS MEDIA, INC.

FRANC, J., RIONDET, M., KARIMI, A. & CHAHINE, G.L. (2011). IMPACT LOAD MEASUREMENTS IN AN EROSIVE CAVITATING FLOW, JOURNAL OF FLUIDS ENGINEERING, VOL. 133(12), PP. 121301-1-121301-8.

FRANC, J., CHAHINE, G.L. & KARIMI, A. (2014). PITTING AND INCUBATION PERIOD, IN: KIM, K., CHAHINE, G.L., FRANC, J. & KARIMI, A. (ED.), 10.1007/978-94-017-8539-6, SPRINGER DORDRECHT HEIDELBERG, PP. 37-69.

FRANC, J. (2009). INCUBATION TIME AND CAVITATION EROSION RATE OF WORK-HARDENING MATERIALS, JOURNAL OF FLUIDS ENGINEERING, VOL. 131(2), PP. 021303.

FRANC, J., RIONDET, M., KARIMI, A. & CHAHINE, G.L. (2012). MATERIAL AND VELOCITY EFFECTS ON CAVITATION EROSION PITTING, WEAR, VOL. 274–275, PP. 248-259.

Gavaises, M., Villa, F., Koukouvinis, P., Marengo, M. & Franc, J. (2015). Visualisation and les simulation of cavitation cloud formation and collapse in an axisymmetric geometry, International Journal of Multiphase Flow, Vol. 68, pp. 14-26.

Gnanaskandan, A. & Mahesh, K. (2016). Large Eddy Simulation of the transition from sheet to cloud cavitation over a wedge, International Journal of Multiphase Flow, Vol. 83, pp. 86-102.

Grosse, C. (2008). Introduction, in: Grosse, C. & Ohtsu, M. (ed.), Acoustic emission testing, Springer Berlin Heidelberg, pp. 3-10.

Hammitt, F.G. (1979). Cavitation Erosion: the State of Art and Predicting Capability, University of Michigan.

Hao, J., Zhang, M. & Huang, X. (2017). The influence of surface roughness on cloud cavitation flow around hydrofoils, Acta Mechanica Sinica, Vol. 34(1), pp. 10-21.

Hattori, S., Hirose, T. & Sugiyama, K. (2010). Prediction method for cavitation erosion based on measurement of bubble collapse impact loads, Wear, Vol. 269(7–8), pp. 507-514.

Hattori, S. & Ishikura, R. (2010). Revision of cavitation erosion database and analysis of stainless steel data, Wear, Vol. 268(1–2), pp. 109-116.

Hattori, S., Ishikura, R. & Zhang, Q. (2004). Construction of database on cavitation erosion and analyses of carbon steel data, Wear, Vol. 257(9–10), pp. 1022-1029.

Hattori, S. & Kitagawa, T. (2010). Analysis of cavitation erosion resistance of cast iron and nonferrous metals based on database and comparison with carbon steel data, Wear, Vol. 269(5–6), pp. 443-448.

Hattori, S. & Nakao, E. (2002). Cavitation erosion mechanisms and quantitative evaluation based on erosion particles, Wear, Vol. 249(10–11), pp. 839-845.

He, Y. & Shen, Z. (2012). Experimental Research on Cavitation Erosion Detection Based on Acoustic Emission Technique, 30th European Conference on Acoustic Emission Testing & 7th International Conference on Acoustic Emission, pp. 1-8.

Heyes, D.M. (2008). Liquids at positive and negative pressure, physica status solidi (b), Vol. 245(3), pp. 530-538.

Holroyd, T. (2000). Acoustic Emission and Ultrasonics Handbook (Coxmoor's Machine & System Condition Monitoring), Coxmoor Publishing Co., Moreton-in-Marsh, United Kingdom.

Hsiao, C., Jayaprakash, A., Kapahi, A., Choi, J. & Chahine, G.L. (2014). Modelling of material pitting from cavitation bubble collapse , Journal of Fluid Mechanics, Vol. 755, pp. 142-175.

Hsiao, C. & Chahine, G.L. (2013). Development of Compressible-Incompressible Link to Efficiently Model Bubble Dynamics Near Floating Body Flow Stage Fluid Code Interface Structure Code, Beteq 2013 XIV International Conference on Boundary Element & Meshless Techniquies.

Hsiao, C., Ma, J. & Chahine, G.L. (2017). Multiscale tow-phase flow modeling of sheet and cloud cavitation, International Journal of Multiphase Flow, Vol. 90, pp. 102-117.

Hujer, J., Carrat, J., Müller, M. & Riondet, M. (2015). Impact load measurements with a PVDF pressure sensor in an erosive cavitating flow, Journal of Physics: Conference Series, Vol. 656(012051), pp. 1-4.

Hujer, J. & Muller, M. (2018). Spatial Distribution of the Cavitation Aggressiveness in a High Speed Cavitation Tunnel, 10th International Symposium on Cavitation (CAV2018), pp. 939-942.

Inaba, H. (2016). AE Sensor (AE Transducer), in: Practical Acoustic Emission Testing, The Japanese Society for Non-Destructive Inspection, pp. 35-45.

KAISER, J. (1950). UNTERSUCHUNGEN ÜBER DAS AUFTRETEN VON GERÄUSCHEN BEIM ZUGVERSUCH (A STUDY OF ACOUSTIC PHENOMENA IN TENSILE TESTS), DOCTORAL THESIS, TECHNISCHE HOCHSCHULE MÜNCHEN, GERMANY.

KANG, C., LIU, H. & SOYAMA, H. (2018). ESTIMATION OF AGGRESSIVE INTENSITY OF A CAVITATING JET WITH MULTIPLE EXPERIMENTAL METHODS, WEAR, VOL. 394-395, PP. 176-186.

KARIMI, A. (1987). CAVITATION EROSION OF A DUPLEX STAINLESS STEEL, MATERIALS SCIENCE AND ENGINEERING, VOL. 86, PP. 191-203.

KARIMI, A. & LEO, W.R. (1987). PHENOMENOLOGICAL MODEL FOR CAVITATION EROSION RATE COMPUTATION, MATERIALS SCIENCE AND ENGINEERING, VOL. 95, PP. 1-14.

KEIL, T., PELZ, P.F. & BUTTENBENDER, J. (2012). ON THE TRANSITION FROM SHEET TO CLOUD CAVITATION, PROCEEDINGS OF THE 8TH INTERNATIONAL SYMPOSIUM ON CAVITATION.

KENDRICK, H., LIGHT, M.S. & CACCESE, V. (2005). DEVELOPMENT OF A CAVITATION EROSION RESISTANT ADVANCED MATERIAL SYSTEM.

KIM, K.H., CHAHINE, G., FRANC, J.P. & KARIMI, A. (2014). ADVANCED EXPERIMENTAL AND NUMERICAL TECHNIQUES FOR CAVITATION EROSION PREDICTION, 1ST ED., SPRINGER, 399 P.

KIM, H.J., KIM, Y.H. & MORRIS, J.J.W. (1998). THERMAL MECHANISMS OF GRAIN AND PACKET REFINEMENT IN A LATH MARTENSITIC STEEL, ISIJ INTERNATIONAL, VOL. 38(11), PP. 1277-1285.

KNAPP, R.T., DAILY, J.W. & HAMMITT, F.G. (1970). CAVITATION, MCGRAW-HILL, NEW YORK, 578 P.

KWOK, C.T., CHENG, F.T. & MAN, H.C. (2006). CAVITATION EROSION AND CORROSION BEHAVIORS OF LASER-ALUMINIZED MILD STEEL, SURFACE AND COATINGS TECHNOLOGY, VOL. 200(11), PP. 3544-3552.

LOOK, A., KIRSCHNER, O., RIEDELBAUCH, S. & NECKER, J. (2018). DETECTION AND LEVEL ESTIMATION OF CAVITATION IN HYDRAULIC TURBINES WITH CONVOLUTIONAL NEURAL NETWORKS, THE 10TH INTERNATIONAL SYMPOSIUM ON CAVITATION (CAV2018), PP. 1-4.

MARPLE JR, L. (1999). COMPUTING THE DISCRETE-TIME "ANALYTIC" SIGNAL VIA FFT, IEEE TRANSACTIONS ON SIGNAL PROCESSING, VOL. 47, PP. 2600-2603.

MILLS, A.F. (1999). BASIC HEAT & MASS TRANSFER, 2ND ED., PRENTICE HALL.

NISHIMURA, S., TAKAKUWA, O. & SOYAMA, H. (2014). EFFECT OF NOZZLE GEOMETRY ON AGGRESSIVITY OF CAVITATING JET FOR CAVITATION EROSION TEST AND APPLICATIONS, IN: KIM, K., CHAHINE, G., FRANC, J. & KARIMI, A. (ED.), ADVANCED EXPERIMENTAL AND NUMERICAL TECHNIQUES FOR CAVITATION EROSION PREDICTION, SPRINGER NETHERLANDS, DORDRECHT, PP. 283-302.

NYYSSÖNEN, T., ISAKOV, M., PEURA, P. & KUOKKALA, V. (2016). ITERATIVE DETERMINATION OF THE ORIENTATION RELATIONSHIP BETWEEN AUSTENITE AND MARTENSITE FROM A LARGE AMOUNT OF GRAIN PAIR MISORIENTATIONS, METALLURGICAL AND MATERIALS TRANSACTIONS A, VOL. 47(6), PP. 2587-2590.

NYYSSÖNEN, T. (2017). QUENCHING AND PARTITIONING OF HIGH-ALUMINUM STEELS; QUENCHING AND PARTITIONING OF HIGH-ALUMINUM STEELS, TAMPERE UNIVERSITY OF TECHNOLOGY.

OBRESCHKOW, D. (2012). ANALYTICAL APPROXIMATIONS FOR THE COLLAPSE OF AN EMPTY SPHERICAL BUBBLE, PHYSICAL REVIEW.E, STATISTICAL, NONLINEAR, AND SOFT MATTER PHYSICS, VOL. 85(6), PP. 066303.

OHTSU, M., ENOKI, M., MIZUTANI, Y. & SHIGEISHI, M. (2016). PRINCIPLES OF THE ACOUSTIC EMISSION (AE) METHOD AND SIGNAL PROCESSING, IN: PRACTICAL ACOUSTIC EMISSION TESTING, THE JAPANESE SOCIETY FOR NON-DESTRUCTIVE INSPECTION, PP. 5-35.

OHTSU, M. (2008). SENSOR AND INSTRUMENT, IN: GROSSE, C. & OHTSU, M. (ED.), ACOUSTIC EMISSION TESTING, SPRINGER BERLIN HEIDELBERG, HEIDELBERG, GERMANY, PP. 19-40.

Pelz, P., Keil, T. & Groß, T. (2017). The transition from sheet to cloud cavitation, Journal of Fluid Mechanics, Vol. 817, pp. 439-454.

Pelz, P., Keil, T. & Ludwig, G. (2014). On the Kinematics of Sheet and Cloud Cavitation and Related Erosion, Fluid Mechanics and its Applications, Vol. 106, pp. 221-237.

Peters, A., Lantermann, U. & el Moctar, O. (2015). Numerical Modelling and Prediction of Erosion Induced by Hydrodynamic Cavitation, Journal of Physics: Conference Series, Vol. 656, pp. 012054.

Plesset, M.S. (1949). The Dynamics of Cavitation, Journal of Applied Mechanics, Vol. 16, pp. 277-282.

Plesset, M.S. (1970). Effect of Dissolved Gases on Cavitation in Liquids.

Plesset, M.S. & Chapman, R.P. (1971). Collapse of an initially spherical vapour cavity in the neighbourhood of a solid boundary, Journal of Fluid Mechanics, Vol. 47(2), pp. 283-290.

Plesset, M.S. & Prosperetti, A. (1977). Bubble Dynamics and Cavitation, Annual Review of Fluid Mechanics, Vol. 9, pp. 145-185.

PREVERO 2018. The PREVERO cavitation erosion tunnel, web page. Available (accessed 25/10/2019): http://web.archive.org/web/20180327065723/http://www.legi.grenoble-inp.fr/web/spip.php?article1265&lang=fr.

Pöhl, F., Mottyll, S., Skoda, R. & Huth, S. (2015). Evaluation of cavitation-induced pressure loads applied to material surfaces by finite-element-assisted pit analysis and numerical investigation of the elasto-plastic deformation of metallic materials, Wear, Vol. 330–331, pp. 618-628.

Rayleigh, L. (1917). Pressure Developed in a Liquid During the Collapse of a Spherical Cavity, Philosophical magazine, Vol. 34, pp. 504-507.

Roy, S.C. (2015). Modeling and analysis of material behavior during cavitation erosion, Doctoral Thesis, Université Grenoble Alpes, France.

ROY, S.C., FRANC, J. & FIVEL, M. (2015). CAVITATION EROSION: USING THE MATERIAL AS A PRESSURE SENSOR, JOURNAL OF APPLIED PHYSICS, VOL. 118(16), PP. 164905.

ROY, S.C., FRANC, J., RANC, N. & FIVEL, M. (2015). DETERMINATION OF CAVITATION LOAD SPECTRA—PART 2: DYNAMIC FINITE ELEMENT APPROACH, WEAR, VOL. 344-345, PP. 120-129.

RYL, J., DAROWICKI, K. & SLEPSKI, P. (2011). EVALUATION OF CAVITATION EROSION–CORROSION DEGRADATION OF MILD STEEL BY MEANS OF DYNAMIC IMPEDANCE SPECTROSCOPY IN GALVANOSTATIC MODE, CORROSION SCIENCE, VOL. 53(5), PP. 1873-1879.

SCHMIDT, H., KIRSCHNER, O. & RIEDELBAUCH, S. (2015). CAVITATION MEASUREMENTS ON A PUMP-TURBINE MODEL, JOURNAL OF PHYSICS: CONFERENCE SERIES, VOL. 656(012051), PP. 1-4.

SCHMIDT, H., KIRSCHNER, O., RIEDELBAUCH, S., NECKER, J., KOPF, E., RIEG, M., ARANTES, G., WESSIAK, M. & MAYRHUBER, J. (2014). INFLUENCE OF THE VIBRO-ACOUSTIC SENSOR POSITION ON CAVITATION DETECTION IN A KAPLAN TURBINE, IOP CONFERENCE SERIES: EARTH AND ENVIRONMENTAL SCIENCE, VOL. 22(052006), PP. 1-9.

SCHWARZER, R., FIELD, D., ADAMS, B., KUMAR, M. & SCHWARTZ, A. (2009). PRESENT STATE OF ELECTRON BACKSCATTER DIFFRACTION AND PROSPECTIVE DEVELOPMENTS, IN: SCHWARTZ, A., KUMAR, M., ADAMS, B. & FIELD, D. (ED.), ELECTRON BACKSCATTER DIFFRACTION IN MATERIALS SCIENCE, 2ND ED., SPRINGER SCIENCE + BUSINESS MEDIA, PP. 1-20.

SOYAMA, H. (2013). EFFECT OF NOZZLE GEOMETRY ON A STANDARD CAVITATION EROSION TEST USING A CAVITATING JET, WEAR, VOL. 297(1–2), PP. 895-902.

SOYAMA, H. & FUTAKAWA, M. (2004). ESTIMATION OF INCUBATION TIME OF CAVITATION EROSION FOR VARIOUS CAVITATING CONDITIONS, TRIBOLOGY LETTERS, VOL. 17(1), PP. 27-30.

STELLER, J., KRELLA, A., KORONOWICZ, J. & JANICKI, W. (2005). TOWARDS QUANTITATIVE ASSESSMENT OF MATERIAL RESISTANCE TO CAVITATION EROSION, WEAR, VOL. 258(1–4), PP. 604-613.

STUTZ, B. (2003). INFLUENCE OF ROUGHNESS ON THE TWO-PHASE FLOW STRUCTURE OF SHEET CAVITATION, JOURNAL OF FLUIDS ENGINEERING, VOL. 125(4), PP. 652-659.

VAN RIJSBERGEN, M., FOETH, E., FITZSIMMONS, P. & BOORSMA, A. (2012). HIGH-SPEED VIDEO OBSERVATIONS AND ACOUSTIC-IMPACT MEASUREMENTS ON A NACA 0015 FOIL, 8TH INTERNATIONAL SYMPOSIUM ON CAVITATION (CAV 2012), 01/01, PP. 958-964.

YLÖNEN, M. (2016). CAVITATION EROSION CHARACTERIZATION OF FRANCIS TURBINE RUNNER BLADE MATERIAL, MASTER OF SCIENCE THESIS, TAMPERE UNIVERSITY OF TECHNOLOGY, FINLAND.

YOUNG, R.F. (1989). CAVITATION, 1ST ED., MCGRAW-HILL.

ZAVALETA GUTIÉRREZ, N., LUPPO, M.I., DANON, C.A., TODA-CARABALLO, I., CAPDEVILA, C. & GARCÍA, D.A. (2013). HETEROGENEOUS AUSTENITE GRAIN GROWTH IN MARTENSITIC 9CR STEEL: COUPLED INFLUENCE OF INITIAL METALLURGICAL STATE AND HEATING RATE, MATERIALS SCIENCE AND TECHNOLOGY, VOL. 29(10), PP. 1254-1266.

ZHANG, S., DUNCAN, J.H. & CHAHINE, G.L. (1994). THE BEHAVIOR OF A CAVITATION BUBBLE NEAR A RIGID WALL, FLUID MECHANICS AND ITS APPLICATIONS, VOL. 23, PP. 429-436.

ZHANG, S., DUNCAN, J.H. & CHAHINE, G.L. (1993). THE FINAL STAGE OF THE COLLAPSE OF A CAVITATION BUBBLE NEAR A RIGID WALL, JOURNAL OF FLUID MECHANICS, VOL. 257, PP. 147-181.

ZHOU, Y. & HAMMITT, F.G. (1983). CAVITATION EROSION INCUBATION PERIOD, WEAR, VOL. 86, PP. 299-313.

# PUBLICATIONS

# PUBLICATION I

**Cavitation Bubble Collapse Monitoring by Acoustic Emission in Laboratory Testing**

Ylönen, Markku., Saarenrinne, Pentti., Miettinen, Juha., Franc, Jean-Pierre. & Fivel, Marc.

Proceedings of the 10th Symposium on Cavitation (CAV2018). 2018, p. 179-184. 05037 (https://doi.org/10.1115/1.861851_ch35)

10th International Symposium on Cavitation - CAV2018
Baltimore, Maryland, USA, May 14 – 16, 2018

CAV18-05037

# Cavitation Bubble Collapse Monitoring by Acoustic Emission in Laboratory Testing

[1]Markku Ylönen*; [1]Pentti Saarenrinne; [1]Juha Miettinen; [2]Jean-Pierre Franc; [3]Marc Fivel

*[1]Tampere University of Technology, 33720 Tampere, Finland; [2]Université Grenoble Alpes, CNRS, Grenoble INP, LEGI, 38000 Grenoble, France; [3]Université Grenoble Alpes, CNRS, Grenoble INP, SIMAP, 38000 Grenoble, France*

## Abstract

In order to investigate the potential of the acoustic emission technique in predicting cavitation erosion, laboratory tests were conducted in a high-speed cavitation tunnel. One face of a cylindrical stainless steel sample was subjected to an annular cavitation field created by the PREVERO cavitation tunnel [1]. Acoustic emission was measured from the back surface of the sample in order to detect impacts caused by cavitation bubble or cloud collapses. Cavitation aggressiveness was varied by changing the operating parameters of the cavitation tunnel. Two different operating points were compared. Collapsing cavitation bubbles lead to impacts towards the sample surface and they induce elastic waves in the material. A resonance type acoustic emission sensor with a resonance frequency of 160 kHz captured these waves during the cavitation tests. The acoustic emission waveform was measured with a sampling frequency of 5 MHz. The sensor was mounted behind the sample using a wave-guide that maintained a transfer path for the elastic waves to travel from the impacted surface to the sensor. The elastic waves reaching the sensor were observed as distinguishable bursts in the acoustic emission waveform. Acoustic emission from cavitation impacts was estimated to be about 100 times stronger than acoustic emission from other sources, such as hydrodynamic events or machine vibration. This means that the signal was almost entirely induced by cavitation. The bursts contain multiple reflections that attenuate in time and that have a frequency content corresponding to the sensor frequency response. The bursts attenuate quickly enough not to overlap, as the cavitation events occur with a large enough temporal separation. The hypothesis in this study is that the maximum amplitude of the acoustic emission event voltage correlates with the strength of the cavitation bubble collapse impacting the surface. Voltage peak value counting was applied to the acoustic emission waveform data. As the bursts contain multiple amplitude peaks due to sensor resonance, an envelope function was fitted to the waveform for peak counting. Using this method, each counted voltage peak value is expected to correspond to a single cavitation impact event. The pulse distribution shows an exponential decrease with a decreasing voltage peak value rate as the peak voltage increases. This compares well with earlier studies, such as [2] and [3], where an exponential distribution of bubble collapse amplitudes was found. The results of this study prove acoustic emission as a direct and non-intrusive method that can be used to monitor cavitation impacts from outside of the cavitation field.

**Keywords**: cavitation impact detection; acoustic emission; cavitation intensity;

## Introduction

The impact load induced by a cavitation bubble collapsing near a solid boundary has been studied by multiple methods, both experimental and computational. In a cavitating flow, the impact load determines material damage in a boundary caused by a single bubble or bubble cloud collapse. Another important factor in material damage is the impact frequency, as cavitation erosion tends to be a cumulative process [4-6]. The impact distribution that combines the impact frequency and amplitude of the cavitation impact loads is essential in determining the cavitation intensity of a flow.

Cavitation impact loads have been measured by various methods. Franc et al. [2] measured the impact loads in the PREVERO cavitation tunnel with conventional pressure sensors flush-mounted in the cavitation closure region. Hujer et al. [3] used PVDF pressure sensors, also flush-mounted in the same tunnel. Both of them observed exponential impact distributions. Hattori et al. [7] studied the impact pressures in an ASTM G-32 vibratory device and Okada et al. [8] used the same device to calibrate pressure sensors for a Venturi nozzle test. In the vibratory test, the impact distribution also follows an exponential law. Franc et al. [9] also observed the pits formed by cavitation impacts and they observed an exponential distribution in the pit size distribution. The pit shape factor or the ratio between pit depth and pit diameter increases with increasing cavitation intensity, meaning that larger impacts lead to deeper pits [10].

Several authors have studied acoustic emission (AE) as a method to detect and characterize cavitation and cavitation erosion. Boorsma and Fitzsimmons [11] created a cavitation monitoring method for ship rudders and propellers. Yongyong and Zaiyang [12] connected the AE-event energy to mass loss in an ASTM-G32 vibratory cavitation apparatus. Schmidt et al [13; 14] worked on a cavitation detection system based in AE on a prototype Kaplan turbine. They discovered that with properly placed sensors, cavitation leads to increase in AE root mean squared voltage value, event energy and fluctuation of both. Van Rijsbergen et al. [15] found that acoustic emission sensors in direct contact

*Corresponding Author, Markku Ylönen: markku.ylonen@tut.fi

with a hydrofoil capture bubble collapses near the foil surface and with the cavitation impact towards the foil, but not those that occur in the flow far from the foil. These studies encourage further development of cavitation monitoring by AE.

In this study, the same cavitation tunnel as used by Franc et al. [2] and Hujer et al. [3] was fitted with acoustic emission sensors. The difference between previous studies with the tunnel in question is that the AE sensors are placed outside of the liquid flow by placing them in the backside of the sample. Voltage peak values corresponding to individual cavitation events were classified by their quantity and voltage. The goal was to produce similar distributions for two different operating conditions from the acoustic emission voltage peak values and to correlate these distributions with those of previous works.

**Experiments**

The experiments were carried out in the PREVERO high-speed cavitation tunnel in LEGI laboratory. The tunnel circulates water through a radially diverging test section. Water comes in to the test section through a Ø 16 mm inlet nozzle and the flow stagnates in the middle of the test section where the sample is located and continues to diverge radially in a 2.5 mm thick channel. The samples are 20 mm thick cylindrical disks with a 100 mm diameter and placed so that the sample center is in the middle of the test section. Cavitation inception is located in the beginning of the radial section and cavitation closure is located between 21 and 26 mm radius of the disk when operating with the typical cavitation number σ = 0.9. Cavitation number in PREVERO is defined in equation 1:

$$. = \frac{P_d - P_v}{P_u - P_d} \quad (1)$$

where $P_d$ is the pressure after the test section, $P_u$ is the pressure before the test section and $P_v$ is the liquid vapor pressure.

The acoustic emission sensors were fitted to the sample using a waveguide that is fixed with a screw thread to the sample. Figure 1(a) shows the sample disk flush mounted to the sample holder and the AE sensors fitted to the sample from behind. Figure 1(b) presents the test section without the sample and the sample holder. The sample and the holder were fastened to the test section so that from the inlet nozzle, the flow radially diverges to a 2.5 mm thick channel.

Figures 1(a) and 1(b). 1(a): Sample mounted to the sample holder and fitted with an AE sensor and a waveguide. 1(b): PREVERO test section opened and with the inlet nozzle in the middle. The sample is flush mounted so that it forms a part of the other wall in the test section.

Cavitation inception occurs at the outlet of the cylindrical nozzle, as the cross section area of the flow drops to 62.5 % of that of the inlet nozzle. Cavitation closure occurs further downstream as the cross section area and therefore the static pressure of the flow increase. Tunnel downstream tank is pressurized by nitrogen and upstream section by a pump linked to a frequency transformer. Downstream pressure varies from ambient pressure to around 3 MPa and the maximum upstream pressure is 4 MPa. The cavitation tunnel is presented in more detail in [1; 4].

The acoustic emission setup was a PAC PCI-2 two channel acquisition card fitted with PAC R15 and D9203b sensors and 20/40/60 preamplifiers. The R15 sensor is a resonance type sensor with a resonance frequency of 160 kHz. A

band-pass filter from 100 kHz to 400 kHz was used. The D9203b sensor is a broadband sensor with a frequency range from 100 kHz to 900 kHz. In this study, only the data acquired with the R15 sensor were analyzed. The samples were made of a stainless steel used in Francis turbines and the waveguides were made of steel.

In this study, two samples were mirror polished with successive diamond pastes and a colloidal silica suspension. One sample was subjected to cavitation erosion for 2 minutes with a 4 MPa upstream pressure and the other for 6 minutes with a 2 MPa upstream pressure. The 4 MPa and the 2 MPa upstream pressures correspond to 89.4 m/s and 63.2 m/s cavity reference velocities, respectively. Cavity reference velocity is defined as the velocity in the test section where pressure is assumed as vapor pressure. A more detailed explanation of cavity reference velocity is in [4]. Pits with this type of exposure covered roughly 10 % of the surface of the cavitation closure area. The cavitation impacts were thus assumed to be hitting virgin material most of the time. Acoustic emission waveforms were acquired with a sampling frequency of 5 MHz for the full duration of the tests.

**Peak value distribution by an envelope function**

Impacts in the cavitation sample surface were observed in the AE waveform as quickly rising voltage peaks that diminish exponentially. The AE waveforms were analyzed in time-voltage space. Wave propagation in the sample and the waveguide may affect the waveforms, but this effect is not considered in detail in this study. The frequency content of each cavitation burst or AE-event resembles that of the sensor frequency response, meaning that the impacts provoke sensor resonance. This means that the events are mostly short duration impacts compared to the sensor time scales. It is assumed that each voltage peak value in the waveform, with its resonance effects, corresponds to one cavitation impact towards the sample surface. The length of a cavitation bubble collapse is in the range of some microseconds up to some tens of microseconds [2; 16]. Through waveform observations, impact overlapping seems not to be significant.

With the assumption that each measured maximum in the voltage peak value corresponds to a single cavitation event, there is a need to filter out the sensor resonance effects when peak counting is applied. In most cases in this study, the acoustic emission waveform contains more or less isolated events with breaks between them. Each event has a distinct maximum or sometimes two or more maximums. To negate the resonance effects, an envelope function is fitted to the waveform. As the signal is approximately symmetric around zero volts, the absolute value of the signal is calculated. After this, the envelope function was fitted to the waveform. The envelope was calculated by spline interpolation over local maximums. The minimum distance between local peaks was set to 16 µs, which is about five times the distance between peaks resulting from sensor resonance. This value was found to be suitable through trial and error method. Figure 2 presents a typical AE waveform sample fitted with an envelope function.

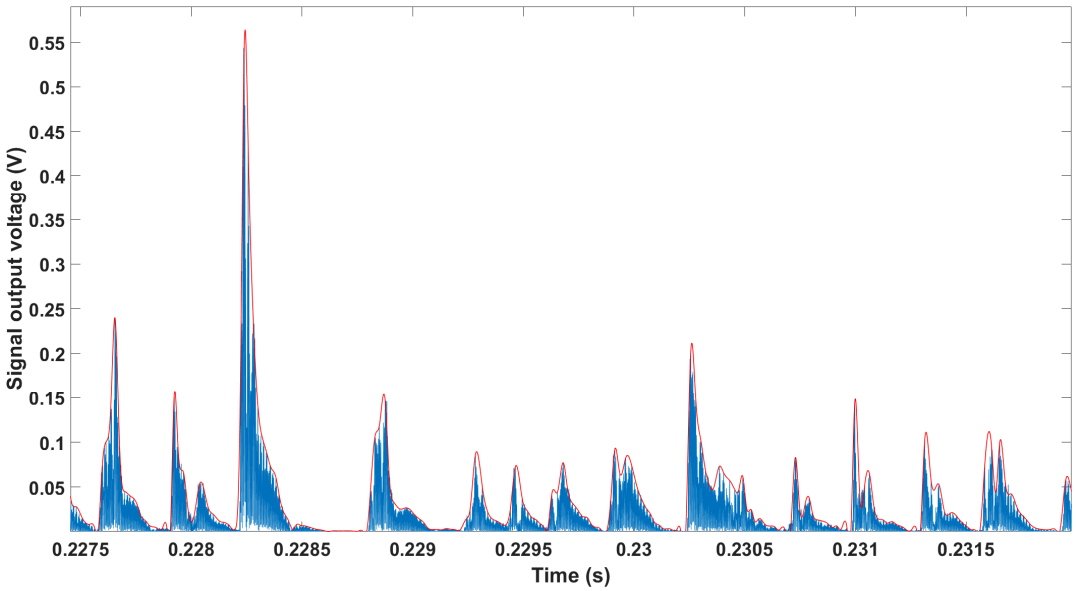


Figure 2. An extract of the AE waveform and the envelope function fitted to it.

As observed in figure 2, the envelope follows the waveform, properly addressing the maximum values of each event. If the event contains two distinct peaks, it is assumed that two events are overlapping and both are taken into account. In the area outside the events, the envelope function may create false peaks due to noise and the formulation of the function. This effect is negated in the results, as events falling below a certain threshold are considered as either static noise or bubble collapses too weak to be erosive.

**Results**

The peak value distributions for both the 2 MPa and the 4 MPa upstream pressure tests are presented in figure 3. The distributions are presented as cumulative so that each rate value represents the rate of voltage peak values larger than the corresponding voltage. The bin size for peak counting was 0.02 V. The rate was expressed in [3] and [4] in counts per second per area, with the area being the sensor active area. In this study, the sensor captures all events occurring in the sample, so the active area cannot be properly defined.

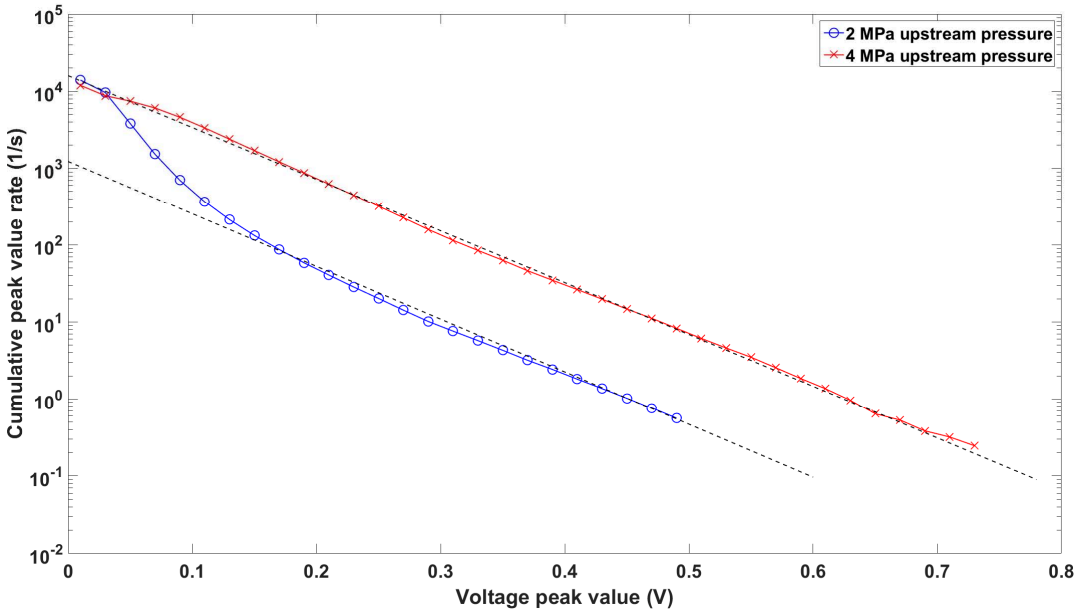


Figure 3. Cumulative peak rate vs. voltage peak value in linear-logarithmic scale. A linear fit was applied to the linear part of the curve.

The cumulative peak value distribution has a linear and a non-linear part in the linear-logarithmic scale. It was assumed that the non-linear part consists of static noise and insignificantly small bubble collapses. This study focuses only on the linear part of the distributions, corresponding to the expected exponential behavior of the cavitation impacts. The exponential law is presented in equation 2:

$$\dot{N} = \dot{N}_0 e^{-\frac{U}{U_0}} \tag{2}$$

where $\dot{N}$ is the peak rate, $\dot{N}_0$ is the reference peak rate, $U$ is the voltage peak value and $U_0$ is the reference voltage. The reference values $\dot{N}_0$ and $U_0$ are presented in table 1.

| **Upstream pressure/cavity reference velocity** | **Reference peak rate $\dot{N}_0$** | **Reference voltage $U_0$** |
|---|---|---|
| 2 MPa / 63.2 m/s | 1232 1/s | 0.063 V |
| 4 MPa / 89.4 m/s | 15958 1/s | 0.065 V |

Table 1. Cumulative distribution reference values

The linear parts of the cumulative distributions in figure 3 are essentially parallel. The reference voltages $U_0$ are calculated from the slope of the linear fits and are thus almost equal. The reference peak rate $\dot{N}_0$ follows the cavity reference velocity $V$ with a relation of $\dot{N}_0 \sim V^{7.4}$. As the slope of the linear fit in linear-logarithmic scale does not change with the change of operating point, it means that the ratio between cumulative impact rates remains constant and independent of voltage peak value.

In this study, the connection between AE voltage peak values and the impact magnitude or impact damage is not addressed. Cavitation pitting in a virgin sample tends to produce pit sizes following a same type of exponential distribution as results in this and previous studies such as [9]. This fact is encouraging and shows that the results presented in this study somehow represent the physical phenomenon of cavitation pitting.

## Conclusion

A method to monitor and characterize cavitation impacts by acoustic emission was presented. Acoustic emission was measured for two different operating conditions and envelope functions were fitted to the resulting waveforms. Voltage peak values were counted from the fitted envelope functions and cumulative distributions were calculated. Reference peak rates and reference voltages were calculated for both operating points. The reference voltage was about the same for both operating points and the reference peak rate had a relation of $\dot{N}_0 \sim V^{7.4}$.

Using the presented method, the cumulative distributions for acoustic emission voltage peak rate value may be calculated for any operating condition by calculating the reference peak rate $\bar{A}_0$ and reference voltage $U_0$ and then applying the relation between reference peak rates, if the distribution for one point is known. To validate the results, multiple operating points should be tested. With the assumption that the relation holds as stated, the acoustic emission distributions can be used in estimating cavitation pitting in the cavitation tunnel. The advantage of the presented method is that it is non-intrusive, as it does not require direct access to the flow. Future studies will address these issues in more detail. These results show the potential of using acoustic emission in cavitation detection and characterization in laboratory testing and eventually in actual hydro machines.

## Acknowledgements

The authors would like to thank Tekes (the Finnish Funding agency for Technology and Innovation), Fortum Power and Heat Oy, Sandvik Mining and Construction Oy, Valtra Oy and Teollisuuden Voima Oyj for funding the research and for providing technical support.

## References

[1] *The PREVERO cavitation erosion tunnel*. Web page. Available (accessed 13/12/2017): http://www.legi.grenoble-inp.fr/web/spip.php?article1265&lang=fr.
[2] Franc, J., Riondet, M., Karimi, A., Chahine, G. (2013). *Impact Load Measurements in an Erosive Cavitating Flow*. Journal of Fluids Engineering, 133(12).
[3] Hujer, J., Carrat, J., Müller, M., Riondet, M. (2015). *Impact load measurements with a PVDF pressure sensor in an erosive cavitating flow*. Journal of Physics: Conference Series, 656(012051).
[4] Franc, J. (2009), *Incubation Time and Cavitation Erosion Rate of Work-Hardening Materials*. Journal of Fluids Engineering, 131(2).
[5] Franc, J., Chahine, G., Karimi, A. (2014). *Pitting and Incubation period*. in: K. Kim, G.L. Chahine, J. Franc, A. Karimi (ed.), 10.1007/978-94-017-8539-6. Springer Dordrecht Heidelberg, pp. 37-69.
[6] Berchiche, N., Franc, J., Michel, J. (2002). *A Cavitation Erosion Model for Ductile Materials*. Journal of Fluids Engineering. 124(3).
[7] Hattori, S., Hirose, T., Sugiyama, K. (2010). *Prediction method for cavitation erosion based on measurement of bubble collapse impact loads*. Wear. 269(7-8).
[8] Okada, T., Iwai, Y., Hattori, S., Tanimura, N. (1995). *Relation between impact load and the damage produced by cavitation bubble collapse*. Wear. 184(2).
[9] Franc, J., Riondet, M., Karimi, A., Chahine, G. (2012). *Material and velocity effects on cavitation erosion pitting*. Wear. 274-275.
[10] Roy, S.C., Franc, J., Fivel, M. (2015). *Cavitation erosion: Using the material as a pressure sensor*. Journal of Applied Physics. 118(16).
[11] Boorsma, A., Fitzsimmons, P. (2009). *Quantification of Cavitation Impacts with Acoustic Emissions Techniques*. Proceedings of the 7th International Symposium on Cavitation (CAV).
[12] Yongyong, H., Zaiyang, S. (2012). *Experimental Research on Cavitation Erosion Detection Based on Acoustic Emission Technique*. 30th European Conference on Acoustic Emission Testing & 7th International Conference on Acoustic Emission.
[13] Schmidt, H., Kirschner, O., Riedelbauch, S., Necker, J., Kopf, E., Rieg, M., Arantes, G., Wessiak, M., Mayrhuber, J. (2014). *Influence of the vibro-acoustic sensor position on cavitation detection in a Kaplan turbine*. IOP Conference Series: Earth and Environmental Science. 22.
[14] Schmidt, H., Kirschner, O., Riedelbauch, S. (2014). *Cavitation measurements on a pump-turbine model.* Journal of Physics: Conference Series. 656(1).
[15] van Rijsbergen, M., Foeth, E., Fitzsimmons, P., Boorsma, A. (2012). *High-Speed Video Observations and Acoustic-Impact Measurements on a NACA 0015 Foil*. 8th International Symposium on Cavitation (CAV).
[16] Kim, K. Chahine, G., Franc, J., Karimi, A. (2014). *Advanced Experimental and Numerical Techniques for Cavitation Erosion Prediction*. 1st ed. Springer.

# PUBLICATION
# II

**Cavitation Erosion Resistance Assessment and Comparison of Three Francis Turbine Runner Materials**

Ylönen, Markku., Saarenrinne, Pentti., Miettinen, Juha., Franc, Jean-Pierre., Fivel, Marc. & Nyyssönen, Tuomo.

Materials Performance and Characterization. 2018, Volume 7, Issue 5, p. 1107-1126. (https://doi.org/10.1520/MPC20180015)

Materials Performance and Characterization

doi:10.1520/MPC20180015 / Vol. 7 / No. 5 / 2018 / available online at www.astm.org

Markku Ylönen,[1,2,3,4] Pentti Saarenrinne,[2] Juha Miettinen,[2] Jean-Pierre Franc,[3] Marc Fivel,[4] and Tuomo Nyyssönen[2]

# Cavitation Erosion Resistance Assessment and Comparison of Three Francis Turbine Runner Materials

## Reference

Ylönen, M., Saarenrinne, P., Miettinen, J., Franc, J.-P., Fivel, M., and Nyyssönen, T., "Cavitation Erosion Resistance Assessment and Comparison of Three Francis Turbine Runner Materials," *Materials Performance and Characterization*, Vol. 7, No. 5, 2018, pp. 1107–1126, https://doi.org/10.1520/MPC20180015. ISSN 2379-1365

## ABSTRACT

Cavitation erosion is the most important erosion mechanism in Francis turbine runner blades. For this reason, knowledge of a material's ability to resist cavitation is important in defining how suitable it is for use in a Francis turbine. In this study, three Francis turbine materials were subjected to cavitation erosion in a high-speed cavitation tunnel. One of the materials was a low-alloy steel, and the other two were stainless steels. The cavitation tunnel produced an annular cavitation field on one face of a cylindrical specimen. The test specimens underwent cavitation erosion until the erosion had reached a maximum penetration depth of about 0.5 mm. The material surface profiles were measured at regular intervals to calculate volume and mass loss. These losses were compared to those of several other materials that had undergone the same tests with the same setup and operational parameters. The materials were compared according to their steady-state erosion rates. The steady-state erosion rate represents a material's ability to resist cavitation erosion once cavitation damage has already started to develop. The low-alloy steel eroded four times faster than the two stainless steels. One of the stainless steels tested here (Stainless steel 1) had the lowest erosion rate, along with another previously tested stainless steel. The other stainless steel (Stainless steel 2) had a slightly greater erosion rate than the first, falling into the same class as other lower-grade stainless steels and a nickel aluminum bronze alloy. The results show that in choosing a turbine blade material, stainless steels outperform

Manuscript received January 30, 2018; accepted for publication August 8, 2018; published online October 26, 2018.

[1] Université Grenoble Alpes, 1209-1211 Rue de la Piscine, Saint-Martin-d'Heres, Grenoble 38400, France (Corresponding author), e-mail: markku.ylonen@tut.fi, https://orcid.org/0000-0002-0092-2537

[2] Tampere University of Technology, Korkeakoulunkatu 10, Tampere 33720, Finland

[3] Université Grenoble Alpes, CNRS, Grenoble INP, LEGI, 1209-1211 Rue de la Piscine, Grenoble 38400, France

[4] Université Grenoble Alpes, CNRS, Grenoble INP, SIMAP, 101 Rue de la Physique, Saint-Martin-d'Heres, Grenoble 38400, France

nonstainless ones. The choice of which type of stainless steel to use is significant in turbines with cavitation problems. The eroded surfaces were analyzed with scanning electron microscopy in order to study the erosion mechanisms, and these studies showed that most of the damage is probably due to low-cycle fatigue.

**Keywords**

cavitation, hydro turbine wear, cavitation erosion resistance

## Introduction

The use of renewable energy sources, such as wind or solar power, is increasingly common in electricity production, which means that a large amount of power with modifiable output is required. The current solution is to make more use of hydropower to regulate the power grid, as this can respond to the rapidly changing demands for power. However, when the hydropower turbines have to operate outside their optimum operational values, they experience cavitation and other disturbances. Cavitation erosion is one of the most significant mechanisms for wear in hydro machines. Therefore, information about the turbine material's ability to resist cavitation erosion is vital in avoiding damage or estimating its extent, or both, after it has occurred.

Cavitation occurs in a hydro machine when the local static pressure of a flow falls below a certain limit, typically close to liquid vapor pressure. At this point, the liquid evaporates, forming small vapor bubbles that go with the flow. As the static pressure recovers, these bubbles collapse violently. Cavitation erosion occurs when a cavitation bubble collapses near a boundary, such as a turbine blade. The presence of the boundary causes the cavitation bubble to collapse nonsymmetrically, which leads to the formation of a micro-jet of water that pierces the bubble and a shock wave caused by the collapsing bubble walls [1]. When this micro-jet of water combined with the collapsing bubble ring hits the boundary, the stress on the material exceeds its yield stress, resulting in microscopic damage. This microscopic damage accumulates on the material's surface, eventually leading to fatigue and rupture on a macroscopic scale.

The main parts of a Francis turbine that suffer from cavitation erosion, along with their cavitation types, are: (1) the blade suction-side walls, inlet edge cavitation; (2) the runner blade trailing edges, travelling bubble cavitation; (3) the runner hub walls, interblade cavitating vortices; and (4) the runner blades, leading edge cavitation [2–4]. An example of cavitation damage in Francis turbine runner blades, concentrated on the blade's trailing edges, is presented in **Fig. 1**. Cavitation may also occur in the draft tube vortex rope of a Francis turbine, but there the cavitation bubbles rarely collapse near any boundary structures.

The development of cavitation erosion in metals has three to four stages: incubation, acceleration, steady-state, and deceleration [5–9]. In the incubation period, an initially virgin material surface experiences plastic deformation, but there is negligible overlap of the cavitation pits. The material's ability to resist the onset of cavitation erosion is closely linked to the length of the incubation period. After the incubation period, the material erosion rate shifts to the acceleration period, when the initial pits start to overlap, and some of the material starts to rupture, i.e., break away. In the steady-state period, the material loss through rupture is in a balanced state. As material is removed, new material becomes exposed to cavitation damage. In the deceleration period, if it is reached, the geometry of the

**FIG. 1**

The red circles indicate cavitation damage in a Francis turbine runner blade's trailing edges.

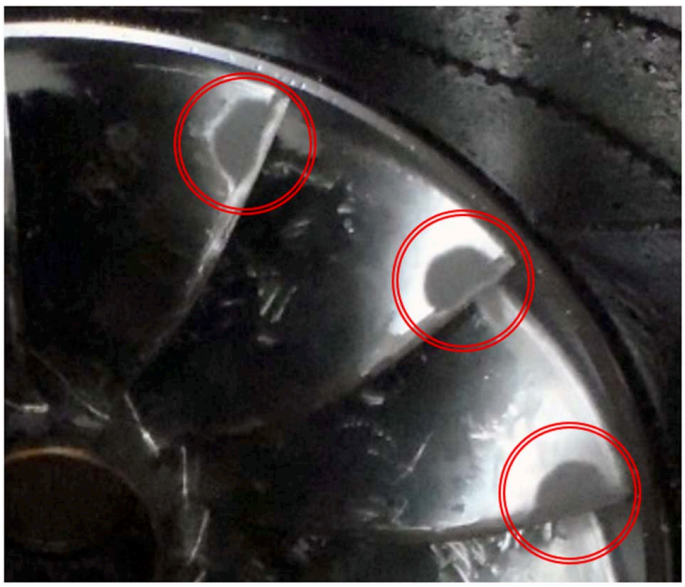

material surface becomes so complex that air and vapor remain in the cavities in the material, thus, potentially damping cavitation impacts and decreasing damage.

There are various methods for assessing a material's resistance to cavitation erosion. The ASTM G32 standardized vibratory cavitation apparatus creates a cavitation cloud in stationary liquid with a vibrating horn (ASTM G32-10, *Standard Test Method for Cavitation Erosion Using Vibratory Apparatus* [10]). Hattori, Ishikura, and Zhang [11], Hattori and Kitagawa [12], and Hattori and Ishikura [13] used this method to compare the erosion rates of a wide range of different metals. Kendrick, Light, and Caccese [14] used it to compare metals and composites. The ASTM G134-95 cavitation testing apparatus, *Standard Test Method for Erosion of Solid Materials by a Cavitating Liquid Jet*, provides a high-speed liquid jet that penetrates a static liquid. Cavitation occurs in the turbulent structures in the shear layer between the jet and the static liquid [15]. Soyama and Futakawa [16] compared multiple metals and several other materials using this method. Karimi [17] studied the cavitation erosion resistance of a duplex stainless steel with a vortex cavity generator.

Although many materials have been extensively tested with the G32 static liquid testing method, few have been tested with hydrodynamic methods, as such methods generally require a larger test setup and more complex test setup. The reasons for studying cavitation erosion resistance in a hydrodynamic testing rig, rather than in a static liquid, have been highlighted by Karimi and Avellan in Ref. [18] and by Chahine, Franc, and Karimi in Ref. [15]. In a vibratory cavitation apparatus, such as the G32, the cavitation bubbles are all virtually the same size, and the cavitation damage is distributed evenly and statically over the whole specimen. This means that the cavitation mostly attacks the weaker material phases. In contrast, the hydrodynamic methods produce both different-size bubbles and flow vorticity effects, as well as other interactions with the liquid flow. For these reasons, it is often regarded that a hydrodynamic method, such as was used in this study, provides a better comparison of materials than the static liquid method.

In their fatigue erosion model, Fortes Patella et al. [19] categorized the fatigue mechanism in cavitation erosion as low-cycle fatigue. Low-cycle fatigue occurs when plastic

deformation occurs with each loading, so that material failure happens after a relatively low number of loading cycles [20]. Balyts'kyi and Chmiel [21] found a correlation between cavitation erosion fracture and the low-cycle fatigue resistance of steel alloys. Aboul-Kasem, Emara, and Ahmed [22] studied the particles removed from the material at different stages of the cavitation erosion process using scanning electron microscopy (SEM). Their study also showed that the erosion mechanism is due to fatigue and that the shape and size of the removed particles changes as the erosion shifts from the incubation period to the mass loss period.

In this study, the materials from three Francis turbines were tested: one low-alloy steel and two different stainless steels (referred to here as Stainless steels 1 and 2). The test setup was the PREVERO high-speed cavitation tunnel (LEGI Laboratory, Grenoble, France) [23]. The tunnel creates an axisymmetric cavitation erosion pattern. The resulting cloud cavitation is very similar to that in a hydrofoil but with a higher intensity. Franc et al. [24] used the cavitation tunnel to study the cavitation erosion of a 7075 aluminum alloy, a C95400 nickel aluminum bronze alloy, a 304L stainless steel, and a A2205 duplex stainless steel, so the materials in this study were compared to those. Deplancke et al. [25] have studied the erosion of ultrahigh molecular weight polyethylene coatings, using the same operating parameters as Franc et al. [24], and they found that such coatings are highly resistant to cavitation. This type of coating could protect against cavitation in hydro machines, if it were economically feasible.

Material microstructure was attempted to be revealed by polishing, etching, and observing with an optical microscope. SEM imaging was used to study the cavitation erosion mechanisms and to pinpoint how the erosion evolves. All three tested materials were observed after they had been subjected to cavitation erosion. The images were taken from different locations and at different magnifications, allowing an overview of the erosion mechanisms at different stages of the erosion to be obtained, as all the stages of erosion coexisted in the eroded specimen, depending on the location of the observed region. The SEM images also allowed the resulting cracks and removed particles to be studied in detail.

## Experimental Setup

The experiments were carried out in a high-speed cavitation tunnel, an image and a schematic of which is shown in **Fig. 2**. The principle is that 20-mm-thick specimen disks of 100-mm diameter were placed in the radially diverging test section. The specimen disk thus acts as an opposing wall onto which the inlet nozzle directs the incoming flow. The incoming flow stagnates in the middle of the specimen and then follows the radially diverging channel, which has a smaller cross-sectional area than that of the inlet nozzle. Here, the flow velocity reaches its maximum and the static pressure its minimum. This is where cavitation is initiated (inception). As the channel diverges, the flow velocity decreases, the static pressure increases, and cavitation closure occurs.

The cavitation number in the tunnel is defined in Eq 1:

$$\sigma = \frac{P_d - P_v}{P_u - P_d} \tag{1}$$

where:

$P_d$ = pressure downstream of the test section, Pa,
$P_u$ = pressure upstream of the test section, Pa, and
$P_v$ = liquid vapor pressure, Pa.

**FIG. 2** The cavitation tunnel used in this study, with schematics and the specimen. The surface profiles were measured in the eight measurement zones or lines, one profile for each. The zones were named so that 0° corresponds to "north," 45° to "northeast," and so on.

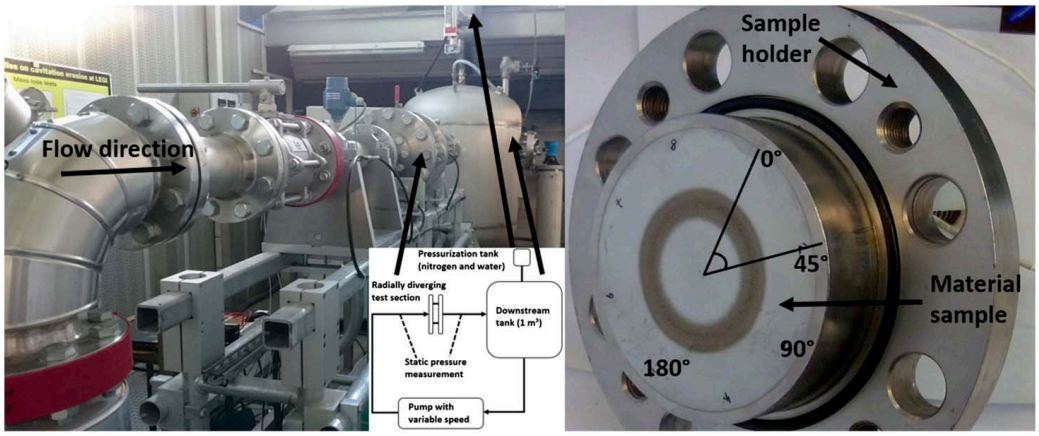


The cavitation number in this study was 0.87, corresponding to an upstream pressure of about 4 MPa and a downstream pressure of about 1.86 MPa. The downstream section is pressurized by nitrogen gas, and a pump linked to a frequency transformer is used to control both the upstream pressure and the flow velocity in the tunnel. Downstream pressure may be set between ambient pressure and about 3 MPa, and the maximum upstream pressure is 4 MPa. Similar cavitation tunnels can be studied in more detail in [6,23,26]. Fig. 2 presents the overview and schematic of the cavitation tunnel, along with the material specimen and specimen holder.

The test section consists of an inlet nozzle with a 16-mm diameter, followed by a radially diverging channel with a 2.5-mm thickness. The cross-sectional area of the channel drops by a factor of 1.6 at the beginning of the radially diverging part. This is where cavitation begins. The cavitation bubbles collapse somewhere between 19–32 mm radial distance from the center of the specimen, with the maximum erosion occurring at a distance of 22 mm from the center.

The main components of the cavitation tunnel are the downstream tank, the pump, and the test section, as presented in Fig. 2. The downstream tank is pressurized by a separate pressurization tank above the downstream tank. The tunnel is filled with water so that the pressurization tank is almost full; nitrogen gas is added from above through a pressure regulator. The pressure regulator controls the downstream pressure and thus, the overall pressure level of the tunnel. The pump, which is located below the tunnel, increases the upstream pressure. The upstream pressure and the flow speed are controlled by changing the pump rotation speed. Most of the pressure drop occurs in the test section when the tunnel is in a cavitating state.

Three Francis turbine runner blade materials were tested: one low-alloy steel and two stainless steels (named low-alloy steel and Stainless steels 1 and 2). All of the turbines in question were cast, but the exact details of the manufacturing process of the runner blades or the material specimens are the manufacturers' confidential knowledge. The low-alloy steel specimen was cut from an old turbine blade, as well as Stainless steel 1. Stainless steel 2 was a separately cast specimen, cast along with the turbine blades. All cutting was water

jet cutting, so it was assumed that any changes in the microstructure because of specimen manufacturing were insignificant. Initial polishing and evening of the surface were done by rotating sand paper grinding, with water added on the paper. Any major heating of the specimen was thus avoided.

The specimens were first mirror polished so that the surface was subject to as little initial strain as possible. The surface of the specimen had to be virtually untouched in order to measure the cavitation incubation period as accurately as possible. To achieve a mirror-polished surface, successive diamond pastes with grain sizes of 3 μm and 1 μm were used with rotating polishing tissues. The surface was finished off using a colloidal silica suspension with a grain size of 0.03 μm and then with yet another type of rotating polishing disk.

As the specimen mass was large compared with the mass of the eroded material (1.2 kg compared with only a few grams), it would be difficult to accurately measure the mass loss because of cavitation erosion by weighing. For this reason, the volume and mass loss were defined through profile measurements. The evolution of the erosion was typically measured at four- to five-hour intervals with a contact profilometer (Form Talysurf 50, Taylor Hobson, Leicester, UK) with a 2-μm spherical diamond point providing the contact with the surface. The erosion evolution could be calculated from these surface profiles, which were measured along a radial line running from the center of the specimen center to its outer edge.

Initially, four profiles for each measurement were taken for the low-alloy steel specimen, but this was later found to be inadequate because the erosion evolution had some discrepancies within one individual specimen, so eight profiles were used for the later measurements. Eight profiles had been used for the stainless steel specimens right from the start, as eight corresponded to the eight different azimuthal angles of the specimen (see **Fig. 2** for visualization). In order to minimize potential errors, each profile was measured five times along parallel lines, each of them one μm apart, and then these values were averaged out to produce one profile. The specimen underwent erosion until the maximum measured penetration depth in at least one profile reached about 500 μm. This took about 25 hours for the low-alloy steel and about 65 hours for both the stainless steels.

The surfaces of the fully eroded specimens were analyzed with an SEM (Leo S440, Leica Microsystems, Wetzlar, Germany). In order to form an accurate estimation of all the erosion mechanisms in the material, a great variety of images were taken, from 20 times magnification to up to 5,000 times magnification (20–5,000×) from different areas of the specimen, including those areas with little to no erosion, up to the maximum erosion.

A high strain rate is typical in cavitation impacts [27]. The material parameters for the specimens were studied with split Hopkinson pressure bar testing, which is a common testing method for stress–strain relationships with a high strain rate. A strain rate of 2,000 1/s was used for all the steels in this study, i.e., the low-alloy steel and the Stainless steels 1 and 2. As the strain rate is not constant in the plastic region of the specimens, Young's modulus is not measurable with this method, so only the yield stresses were obtained and used to compare the materials.

## Calculating Steady-state Volume Loss Rate

Ten to twenty profiles were obtained for each azimuthal angle for each of the specimen disks, each corresponding to an instant of time in the erosion process. **Fig. 3** shows the erosion evolution as a function of time for the low-alloy steel specimen with an azimuthal

**FIG. 3** Cavitation erosion evolution of low-alloy steel. For the sake of clarity, only chosen profiles corresponding to different exposure times are displayed.

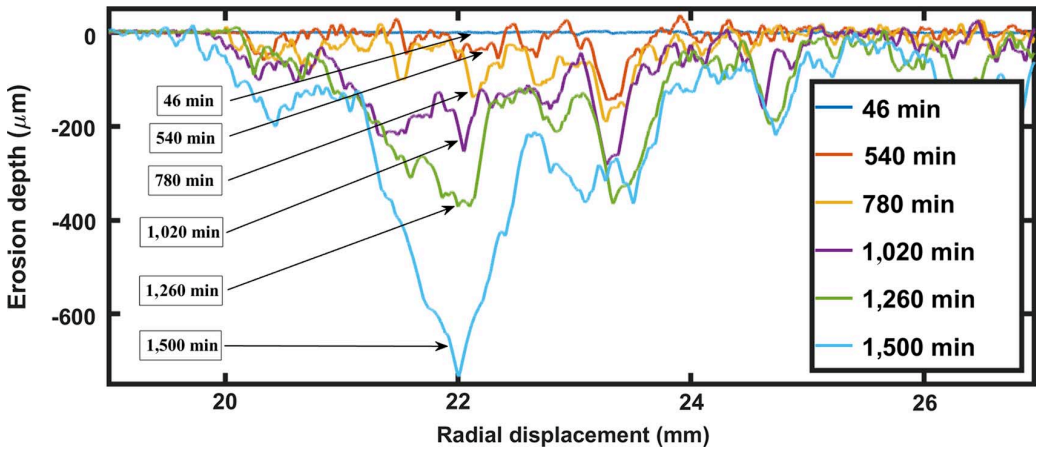


angle of 0°. The maximum penetration depth varies through the different azimuthal angles for the same specimen but is always located in the same radial location, as the erosion pattern is axisymmetric.

The first profile plotted in Fig. 3 shows the transition area between the incubation and acceleration periods that occurs after 46 minutes of exposure to cavitation. The erosion on the specimen is visible to the naked eye, and in the measured profiles, it appears as surface roughness. The blue curve shows the erosion after 25 hours (1,500 minutes), which was the total exposure time of the low-alloy steel and corresponds to a penetration depth of about 750 μm in the specimen surface for the azimuthal angle of 0° (about 450 μm for angles 90° and 270°). The initial surfaces, presented in Fig. 4, were virtually flat compared with the advanced erosion stages.

The initial profiles in Fig. 4 are only for one azimuthal angle, but the profiles for the other angles are of a similar order of magnitude. The initial profiles were separated from the subsequent ones, although this procedure has only a marginal effect, as the roughly half-micrometer fluctuations are negligible compared with the up-to-700 micrometer penetration depths. Values above zero in depth were observed for all the materials, especially in the incubation period. This is due to the piling up of the eroding metal because of the cavitation impacts. This is expected in materials with a high ratio between the Young's modulus and the yield stress, such as most metals [7].

As cavitation is assumed to be axisymmetric in the test section, one would assume an axially uniform erosion rate in the disk. To mitigate possible anomalies in the axisymmetricity of the erosion, the stainless steel specimens were turned 90 degrees in the specimen holder after each profile measurement. This procedure was introduced after the experiments with the low-alloy steel, as nonuniformities had been observed in these. Even with this procedure, the erosion depth was not equal in all the specimen azimuthal angles. Fig. 5a–c shows photographs of the tested specimen materials after their respective full exposure times.

The volume loss at a given time for a given specimen was calculated from the erosion profiles, as shown in Fig. 4. To calculate the total volume loss over the specimen, the depth value for each point was multiplied by the circumference. This meant that the volume loss

**FIG. 4** Initial surface profiles for the low-alloy steel and Stainless steels 1 and 2.

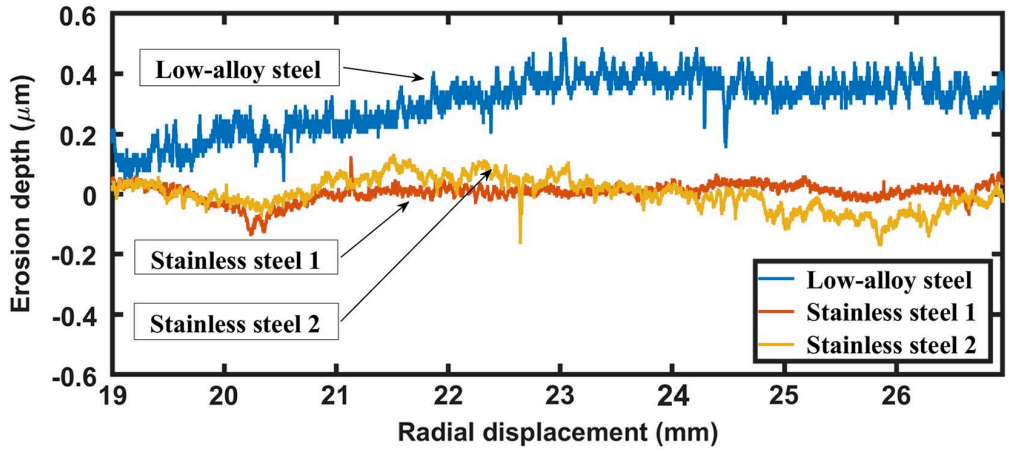


**FIG. 5** Material specimens after full exposure time: (a) low-alloy steel, 25 hours, (b) Stainless steel 2, 70 hours, (c) Stainless steel 1, 65 hours. The low-alloy steel is oxidized because of contact with water during the test.

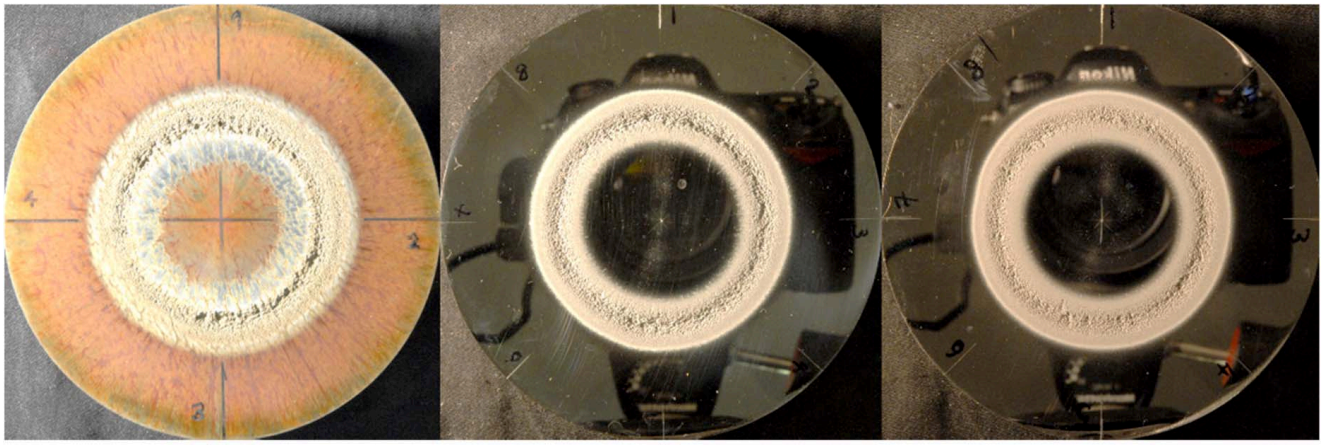


was calculated for each profile under the assumption that the erosion profile would be the same across the whole specimen. The average volume loss was calculated from the profiles (either 4 or 8). Finally, the mass loss was calculated by multiplying the volume loss by the material density.

## Results

### MATERIAL PROPERTIES

An external operator tested the chemical composition of the materials and these are listed in Table 1.

The materials actually contained minor traces of several other elements, but these were irrelevant and have been excluded from Table 1. The materials' mechanical strength was studied with split Hopkinson pressure bar testing, as cavitation impacts tend to have a

**TABLE 1**
Material chemical properties. The element contents are expressed as mass percentage.

| Material | Fe | C | Cr | Si | Mn | P | S | Ni | Mo | W |
|---|---|---|---|---|---|---|---|---|---|---|
| Low-alloy steel | 98.69 | 0.205 | 0.0051 | 0.205 | 0.551 | 0.033 | 0.028 | 0.026 | 0.0032 | 0.0077 |
| Stainless steel 1 | 80.00 | 0.046 | 13.80 | 0.238 | 0.726 | 0.026 | 0.014 | 4.385 | 0.201 | 0.219 |
| Stainless steel 2 | 81.67 | 0.02 | 12.6 | 0.45 | 0.58 | 0.025 | 0.005 | 4.2 | 0.45 | – |

high strain rate. The stress–strain curve of a split Hopkinson pressure bar test is similar to that of conventional compression tests. However, the strain rate changes significantly in the elastic region, and because this impeded the accurate calculation of the Young's modulus, the yield stress was used. The yield stress is a significant parameter for determining whether a cavitation impact has damaged a material [28]. The yield stress may be extracted from the stress–strain curves by fitting a linear equation to both the elastic and the plastic part of the curve and then finding the intersection of these equations. The yield stresses at 2,000 1/s strain rate for all three steels tested in this study are listed in **Table 2**. For the comparison materials, the values for the yield stresses are taken from the literature on conventional compression testing. The conventional pressure test value is also listed for the low-alloy steel, but there were no listed values for the two stainless steels.

To characterize the material microstructure, the stainless steel specimens were polished, etched, and then studied through optical microscopy. Two examples of the microscope images are presented in **Fig. 6a–b**. The microstructure study concentrated only on the two stainless steels, as the low-alloy steel was considered an outdated turbine material, and it was only used for erosion rate comparison.

According to the optical microscope analysis, Stainless steel 1 in **Fig. 6a** is fully martensitic, with small amounts of carbides and other precipitates, as well as larger slag inclusions. The precipitates (possibly carbides) are too small to properly resolve by optical microscopy. The microstructure of Stainless steel 2 in **Fig. 6b** is predominantly martensitic, with a small amount of residual δ-ferrite and carbides and other precipitates, which have a bimodal size distribution. The dark lines in **Fig. 6a** emerge from the prior austenite microstructure. They were not found in the other specimen, both because of the etching

**TABLE 2**
Steady-state mass loss and volume loss rates of the studied materials.

| Material | Steady-state volume loss rate ($mm^3/h$) | Steady-state mass loss rate (mg/h) | Material density ($kg/m^3$) | Yield stress (MPa) |
|---|---|---|---|---|
| Low-alloy steel | 8.95 | 69.79 | 7,800 [34] | 228, 259 at (2,000 1/s) |
| Stainless steel 1 | 1.79 | 13.93 | 7,800 | 452 at (2,000 1/s) |
| Stainless steel 2 | 2.72 | 21.23 | 7,800 | 477 at (2,000 1/s) |
| 7075 Aluminum alloy specimen 1 | 7.88 | 22.12 | 2,810 [35] | 103–145 [35] |
| 7075 Aluminum alloy specimen 2 | 8.18 | 22.99 | 2,810 [35] | 103–145 [35] |
| A2205 Stainless steel specimen 1 | 2.21 | 17.27 | 7,820 [36] | 448 [36] |
| A2205 Stainless steel specimen 2 | 1.31 | 10.25 | 7,820 [36] | 448 [36] |
| 304L Stainless steel specimen 1 | 3.29 | 26.29 | 8,000 [37] | 210 [37] |
| 304L Stainless steel specimen 2 | 2.83 | 22.64 | 8,000 [37] | 210 [37] |
| C95400 Nickel aluminum bronze specimen 1 | 2.86 | 21.34 | 7,450 [38] | 205 [38] |
| C95400 Nickel aluminum bronze specimen 2 | 2.30 | 17.17 | 7,450 [38] | 205 [38] |

**FIG. 6**

Optical microscope images of Stainless steels (a) 1 and (b) 2.

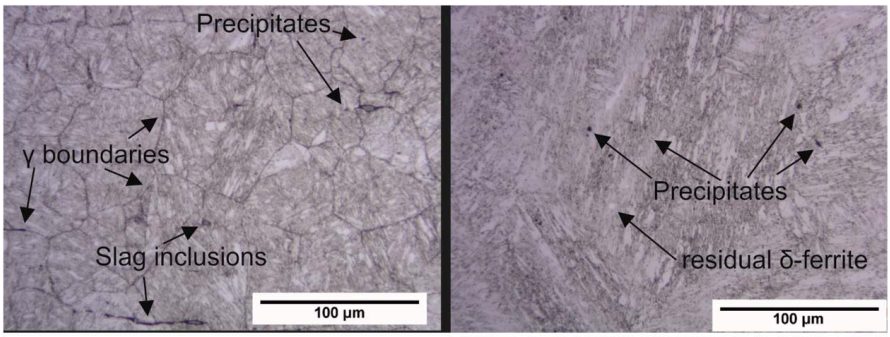


treatment not being optimal for the material and the apparently much larger prior austenite grain size.

The notable difference between the microstructures is the considerably finer prior austenite grain size of Stainless steel 1, measured as 37 µm, with a standard deviation of 10 µm, using the mean lineal intercept method as defined by ASTM E112, *Standard Test Methods for Determining Average Grain Size* [29]. The prior austenite boundaries of the specimen Stainless steel 2 could not be resolved. However, based on the visual observation of block and packet size and the configuration of the lath structure, the prior austenite grain size of Stainless steel 2 is much larger, by approximately an order of magnitude. The prior austenite grain size has been shown to correlate with martensite packet and block size [30], which in turn has a negative correlation with strength. It has been shown that impact resistance and plasticity are particularly sensitive towards prior austenite grain size [31,32], possibly explaining the better resistance of Stainless steel 1 towards cavitation impacts.

## STEADY-STATE EROSION RATE

The volume loss of the eroded materials as a function of time is presented in Fig. 7. The three specimens tested in this study, i.e., the low-alloy steel and Stainless steels 1 and 2 are presented, as are two specimens each of the other materials tested by Franc et al. [24]. Their specimens were smaller than those used for this study, as they were fitted to a specimen holder that holds eight specimens at a time. Their small 16-mm-diameter disks were eroded simultaneously, but for ease of comparison, the erosion of Franc et al.'s small disks was calculated as if they covered the same area as our large disks.

The volume loss curves of the low-alloy steel and both specimens of the 7075 aluminum alloy follow almost the same line, these being the fastest to erode. As some of the specimens had eroded more than the others, defining the steady-state erosion rate from only the final erosion rate is not a fair comparison. The volume loss rate seems to fluctuate even at the relatively steady states of erosion, as presented in Fig. 8. For this reason, the steady-state volume loss rate is rather difficult to define. Therefore, a decision was made to define the volume loss rate as the average of all the volume loss rates between 50 $mm^3$ and 100 $mm^3$.

The incubation time was not used in comparing the materials in this study, because the variance between similar materials was too great, so its effects were removed by linear curve fitting to the linear part of the volume loss curves in Fig. 7 and then defining the $x$-axis intersection of the linear fit. To define the average volume loss rate between 50 $mm^3$

**FIG. 7** Volume loss of eroded materials.

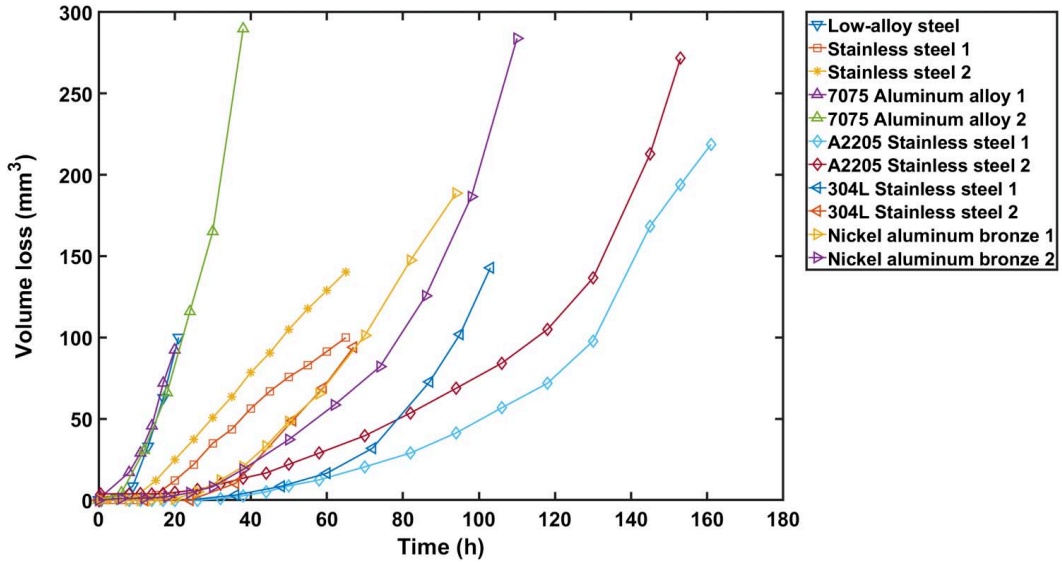


and 100 $mm^3$, a fourth order polynomial function was fitted to the volume loss data. The steady-state volume loss rate was calculated as in Eq 2:

$$V_{loss\ rate} = \frac{100\ mm^3 - 50\ mm^3}{t_{100} - t_{50}} \tag{2}$$

where:

$t_{100}$ = time when erosion volume is 100 $mm^3$, s, and
$t_{50}$ = time when erosion volume is 50 $mm^3$, s.

**FIG. 8** Volume loss rate as a function of volume loss.

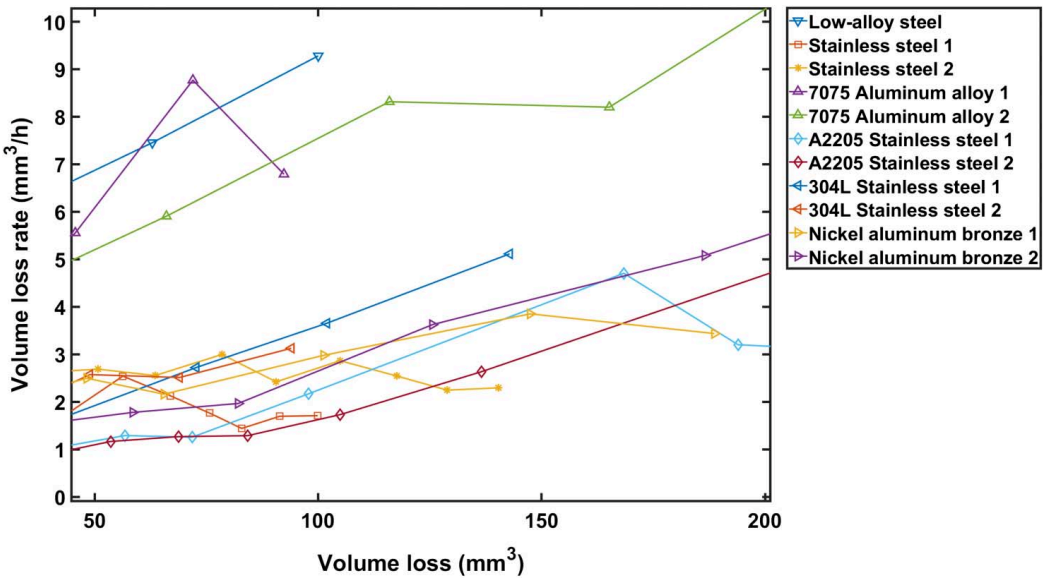

The values for $t_{100}$ and $t_{50}$ are instants interpolated from the polynomial fitted to the experimental points when the volume losses are 100 $mm^3$ and 50 $mm^3$, respectively.

As previously explained, the specimens in our study were a different size to those used in the comparison study. The average steady-state erosion rates and the high strain rate yield stresses for all of the compared materials are presented in **Table 2**.

The material densities presented in **Table 2** are general values, as they were not measured for the materials or individual specimens used in our study. For the two stainless steels, densities are assumed to be the same as that of the low-alloy steel. In the present work, the volume loss rate is preferred over the mass loss rate for defining the erosion rate, thereby reducing the importance of defining the densities accurately.

A lower steady-state volume loss rate indicates higher cavitation erosion resistance. Using this metric, our results show that the low-alloy steel has the poorest resistance to cavitation, falling into the same category as the 7075 aluminum alloy in terms of volume loss rate. The 304L stainless steel has a moderate resistance to cavitation and Stainless steel 2 falls into the same category as the C95400 nickel aluminum bronze alloy. Stainless steel 1 and A2205 stainless steel are both superior to all the other tested materials.

The low-alloy steel has a lower yield stress than the two stainless steels, with a strain rate of 2,000 1/s. The low-alloy steel was also tested in a conventional compression test, so both values are presented in the table. The other materials were not tested for their yield stresses in this study, so those values are taken from the literature. The three tested materials are not comparable to the rest of the specimens, as they were measured at different strain rates. However, they may be compared separately. The yield stresses for Stainless steels 1 and 2 are almost equal, although they have different erosion rates. For the other materials, the yield stresses correlate with the erosion rates, so that a higher yield stress corresponds to a lower steady-state erosion rate. It is worth noting that the low-alloy steel has a higher yield stress than the aluminum alloys (if one ignores the different strain rates).

It is noticeable that the low-alloy steel suffered greater mass loss than the 7075 aluminum alloy. In addition, the low-alloy steel started to rust during the experiments as it was in contact with water. This may also have contributed to its high erosion rate. As the metal oxidizes, it degrades the quality of the surface, which is then removed by the cavitation, continuously exposing fresh surface to the water, thus increasing the corrosion rate [33].

An interesting detail that surfaced from this comparison of the two-turbine runner stainless steels is that the one that performed better came from a Francis turbine designed in the 1970s, while the worse-performing one came from a much more recent Francis turbine design (2010s). The low-alloy steel was from a turbine constructed in the 1930s, which was later decommissioned. This detail shows that, at least in this case, cavitation erosion resistance was probably not a known parameter when making material choices at that time. Shifting from steels to stainless steels seems to increase the metal's resistance to cavitation erosion significantly.

As mentioned previously, the erosion rate is dependent on the azimuthal angle, as the evolution of the erosion is not perfectly uniform. This nonuniformity may not have been apparent with the small specimens used in the experiments by Franc et al. [24]. An example of the nonuniformity of erosion evolution is presented in **Fig. 9**, in which eight curves for eight different azimuthal angles are presented.

The reason for the differences in the erosion rates could be because of differences in the composition of the material within just the one specimen. As cavitation is such a complex process, it is possible that even small differences in the specimen's composition and

**FIG. 9** Volume loss of Stainless steel 2 for all eight specimen azimuthal angles. The incubation time was calculated for each azimuthal angle separately and was then subtracted from the exposure time to negate its effect.

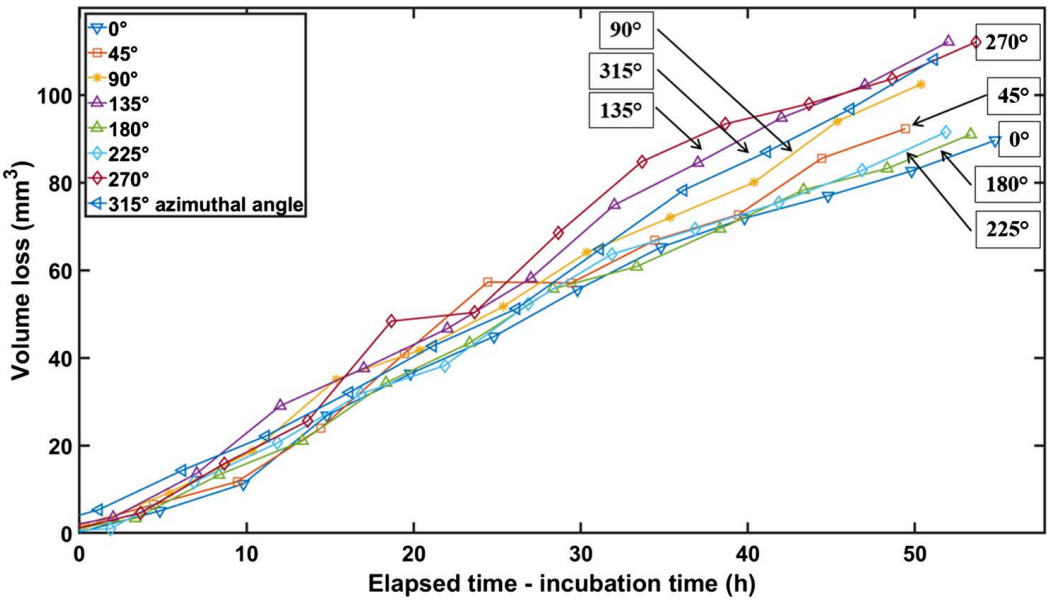


microstructure would lead to different erosion rates. These may that persist even if the erosion process goes on for a long time. The erosion rates do not seem to fall clearly around a single value as the erosion evolves. The strength of cavitation erosion in the cavitation tunnel is assumed to be axisymmetric, and even if this is not absolutely true, turning the specimen between each testing intervals should have negated any nonaxisymmetrical effect.

To study the differences in steady-state volume loss rates within one specimen, the rates were calculated using the same method as before for the four azimuthal angles for the low-alloy steel and for all eight azimuthal angles for the two stainless steels. The resultant steady-state volume loss rates are presented in Table 3.

The differences between the specimen azimuthal angles in the steady-state volume loss rates are significant, especially for the low-alloy steel. The low-alloy steel was not turned between measurements, so nonuniformity in the erosion potential of the cavitation tunnel might be a major reason in the differing erosion rates. The erosion rate follows a pattern in which a relatively high value always has a counterpart falling into the same diagonal. This raises the question as to whether the specimens were completely isotropic. It was initially assumed that they were, as they were manufactured by casting and were cut using methods that do not overly heat the specimen. Small differences in the

**TABLE 3**
Steady-state volume loss rates of the studied materials for different specimen azimuthal angles. The specimen azimuthal angle is presented in degrees so that 0° degrees means north and 180° degrees means south on the circular specimen surface.

| Material | Rate 1 ($mm^3/h$) 0° | Rate 2 ($mm^3/h$) 45° | Rate 3 ($mm^3/h$) 90° | Rate 4 ($mm^3/h$) 135° | Rate 5 ($mm^3/h$) 180° | Rate 6 ($mm^3/h$) 225° | Rate 7 ($mm^3/h$) 270° | Rate 8 ($mm^3/h$) 315° |
|---|---|---|---|---|---|---|---|---|
| Low-alloy steel | 11.62 | | 5.44 | | 12.38 | | 3.63 | |
| Stainless steel 1 | 1.40 | 1.70 | 2.02 | 2.24 | 1.52 | 1.58 | 2.30 | 2.21 |
| Stainless steel 2 | 4.02 | 2.94 | 3.02 | 2.95 | 3.56 | 2.66 | 2.43 | 2.27 |

microstructure are expected, as the material solidifies at a different rate depending on the location inside the cast. The fact that the steady-state volume loss rate fluctuates significantly depending on the azimuthal angle clearly indicates that the cavitation erosion resistance of a material cannot properly be defined without looking into its microstructure.

### SEM

SEM images with various magnifications were taken of the specimen surface in order to make this a qualitative study. Fig. 10a–c shows three panoramic images of the eroded areas of the studied materials taken with a 20 × magnification. These images show the center of the specimen on the left, and the right is towards the edge of the specimen.

Although the areas of maximum erosion in the images in Fig. 10 are not exactly aligned, in the actual specimens, the erosion occurred in the same radial location. The discrepancy is due to the image processing, as the panoramic images were constructed from multiple smaller images.

The erosion in the low-alloy steel in Fig. 10a begins abruptly compared to the stainless steels in Fig. 10b–c. The erosion in the downstream region after the maximum erosion depth is about 6-mm long for all three materials, while in the upstream region, although it is approximately the same for the stainless steels, it is only about 2-mm long for the low-alloy steel (based on visual observations from these images). The pits and erosion in the upstream region of the stainless steels consist of individual pits and surface roughness, placing the stage of erosion in those regions as somewhere between the incubation and acceleration periods. The downstream regions of all the specimens are rougher than the upstream regions, putting these regions in the acceleration, or even the steady-state, period of erosion evolution.

The exposure time of the low-alloy steel was much lower than that of the stainless steels. As the upstream damage to the stainless steels consists of single pits and surface roughness, it is concluded that the rate of cavitation impacts is much lower upstream of the maximum depth than it is in other regions. Because of the low-alloy steel's lower exposure time, there might be less time for such individual pits to form in the upstream region.

**FIG. 10**

Panoramic SEM images of (a) low-alloy steel, (b) Stainless steel 1 and (c) Stainless steel 2 with a 20 × magnification. Flow direction from the specimen center towards the edges is marked with the red arrows between the images.

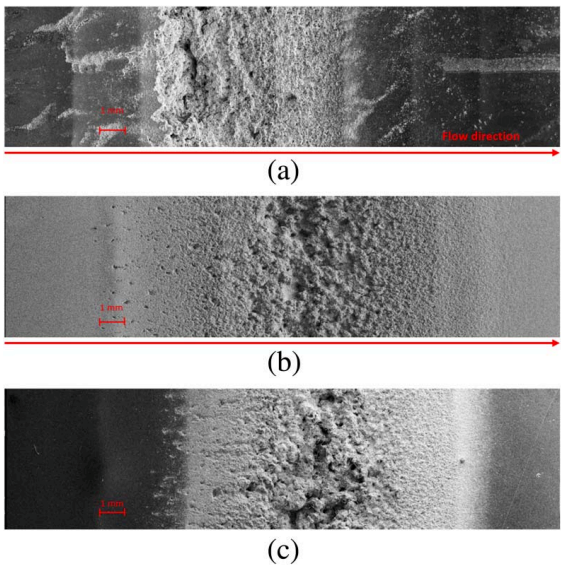

Figs. 10 and 11 show SEM images of the low-alloy steel at a greater magnification (200×). The evolving cracks can be seen everywhere, so it may be assumed that these cracks, and any subsequent ruptures, would be a major factor in the rate of material loss, as expected.

In Fig. 11, the eroded surface is uneven and the "valleys" of the erosion pits seem to be deep compared to the surrounding "mountains." The actual depth of the pits could not be defined using the SEM. This image with 200 × magnification shows the overall structure of the highly eroded surface, but it does not tell us much about the erosion mechanisms. When a chunk of the material is removed by rupture, it leaves a smooth surface behind, as can be seen in Fig. 12. The smooth surface is then attacked by subsequent cavitation impacts, leaving small pits that eventually start to overlap.

The 1,000 × magnification in Fig. 12 offers more insight into the erosion mechanisms. The surface in the middle of the image is relatively smooth, with some small widely-spaced pits in it. The diameter of the small pits is in the range of one μm, which corresponds to small cavitation impacts. One possible cause for such a smooth surface could be that a relatively large chunk, microscopic in actual size, of material was removed quite recently. Once the large chunk had been removed, the new smooth surface was only exposed to cavitation for such a short time (the time remaining in the test period) that only the small individual pits are seen.

Fig. 13, at 2000 × magnification, shows the progression of a crack front.

A series of lines, identified by the red arrows, are visible in Fig. 13. As each new impact of sufficient amplitude hits the surface of the material in the vicinity of the crack, the crack front is supposed to jump from one line to the next. This crack propagation ends up with the removal of a micropiece of material that makes the plane of the propagated crack visible, as can be seen in Fig. 12. This pattern is commonly associated with low-cycle fatigue, which supports the idea that cavitation erosion at the intensity generated in the cavitation tunnel is most probably due to low-cycle fatigue.

**FIG. 11**

Low-alloy steel SEM image erosion detail with 200 × magnification. Some of the cracks are marked by red crosses.

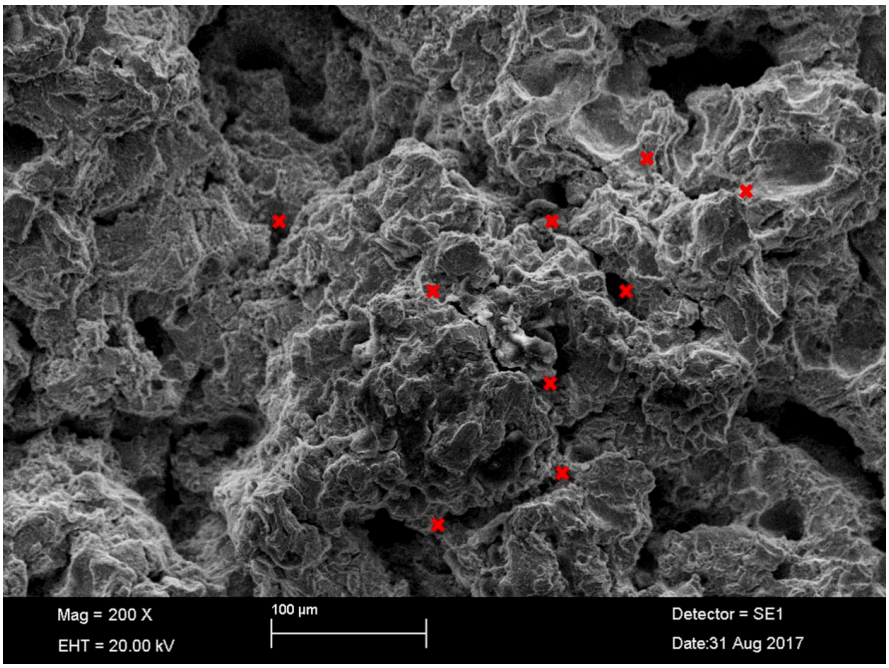

**FIG. 12** Stainless steel 1 SEM image erosion detail with 1,000 × magnification. The red lines highlight a relatively smooth surface.

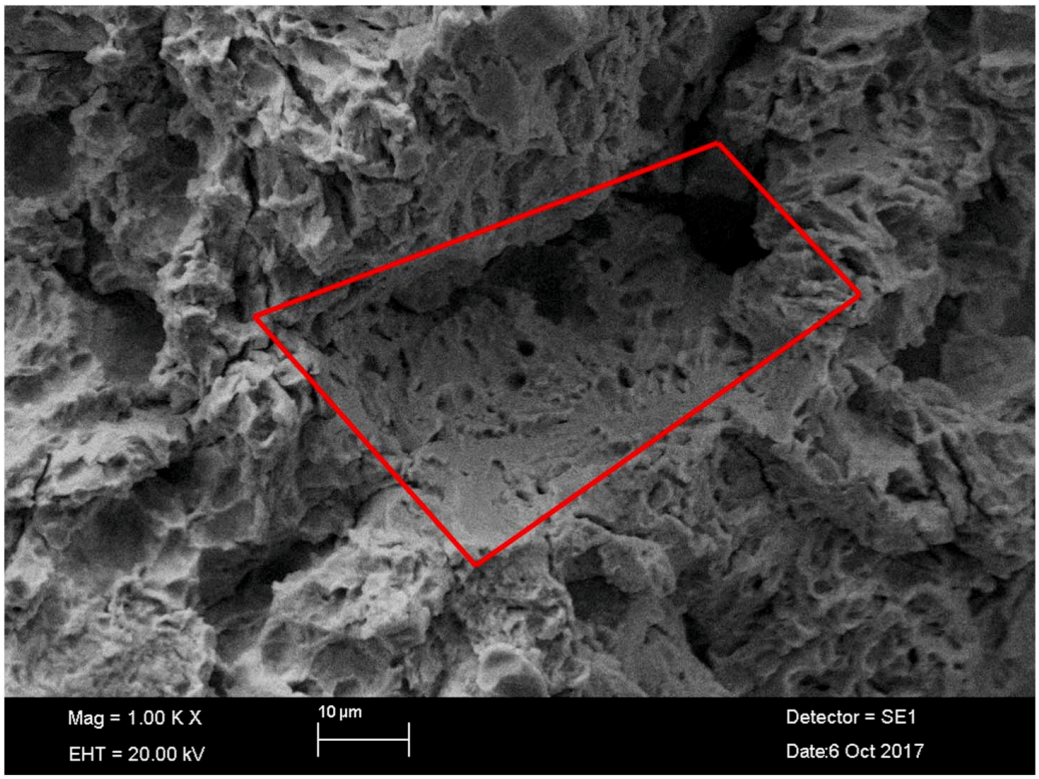


**FIG. 13** Successive crack front positions for Stainless steel 1 with 2,000 × magnification. The schematic in the top-right corner describes the crack propagation and the development of the "beach marks."

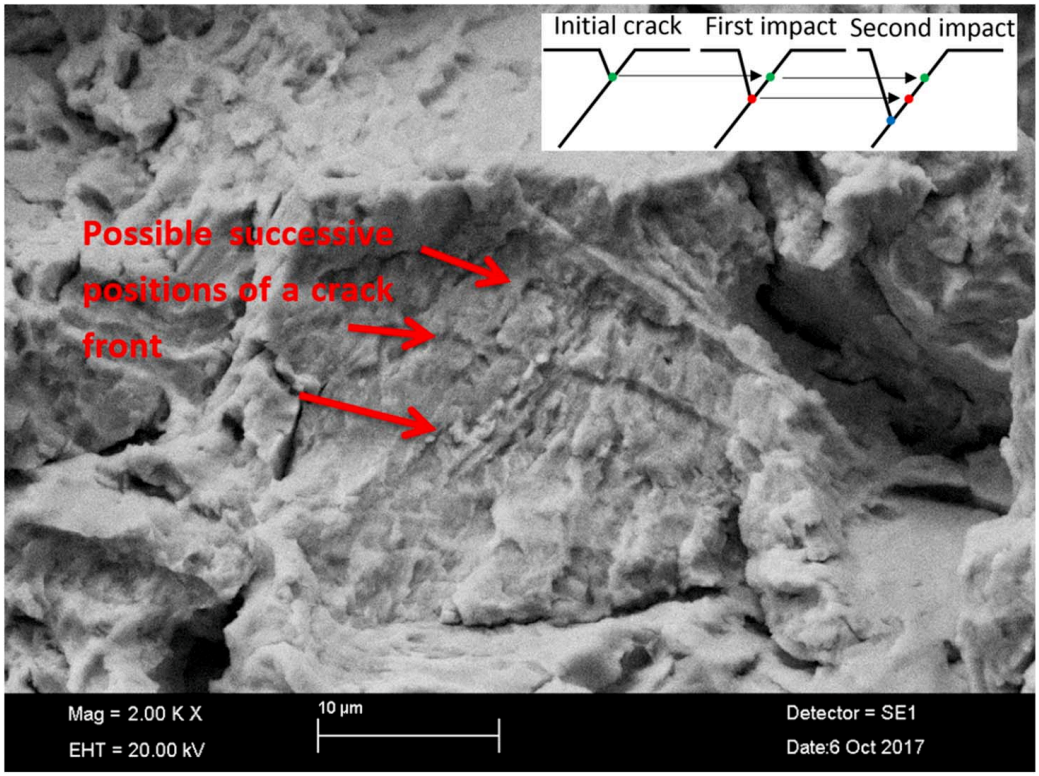

**FIG. 14** A SEM image of Stainless steel 2 erosion with 2,000 × magnification. The red lines highlight the assumedly soon-to-be-removed material chunk marked by the red A-letter.

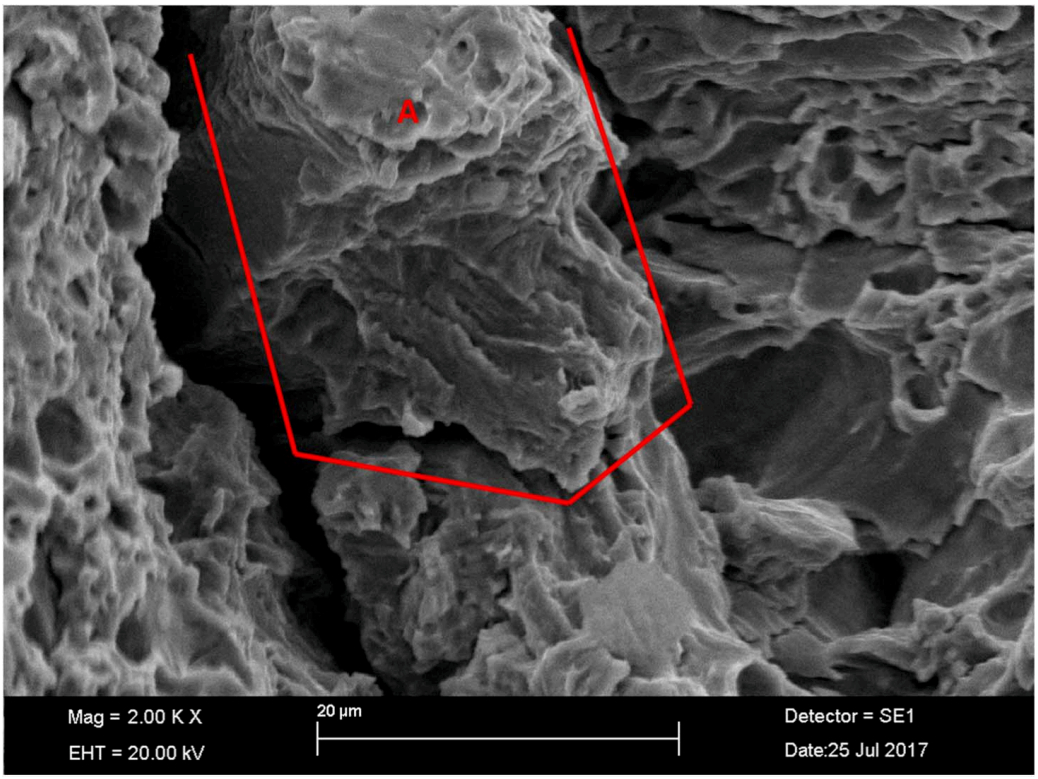


Fig. 14 shows a well-developed crack propagation process with a presumably soon-to-be-removed chunk of material.

The image with 2000 × magnification in Fig. 14 offers some insight into the removal of individual chunks of material. The chunk in the middle of the image is surrounded by large cracks, and it is covered with plastic deformation resulting from cavitation impacts. If the erosion were to continue, the cavitation impacts hitting the chunk of loosened material would eventually cause it to break away.

These observations all support the results and assumptions made in [19,21,22], which is that the erosion mechanism in the mass loss period is probably caused by low-cycle fatigue. Virgin surfaces with several small pits showing where tiny particles have subsequently been removed were found throughout the specimens, as were cracks and soon-to-be-removed chunks.

## Conclusions

Steady-state cavitation erosion rates were studied for one low-alloy steel and two stainless steels (Stainless steel 1 and 2). They were compared to those of 7075 aluminum alloy, C95400 aluminum bronze alloy, 304L stainless steel, and A2205 stainless steel. Steady-state volume loss rate was defined as the average volume loss rate between 50 $mm^3$ and 100 $mm^3$ total volume loss, to mitigate fluctuation and to provide a fair comparison of the materials. It was shown that to properly assess steady-state erosion rate, one has to

average several erosion processes through the specimen. The stainless steels were specimens from turbines that are of a type that is still in use, so they are relevant in the field of turbine design.

The low-alloy steel had the poorest cavitation erosion resistance, along with the 7075 aluminum alloy. In this study, 304L stainless steel, C95400 aluminum bronze alloy, and Stainless steel 2 had a better resistance than the other materials, while A2205 stainless steel and Stainless steel 1 had the highest cavitation erosion resistance. It was found that the erosion rates differ significantly even within one specimen. This means that assessing a single value for cavitation erosion resistance is problematic, because factors, such as small differences in the local material composition or microstructure, might change the erosion rates significantly. Even minor anisotropies in the specimen material might be the cause of significantly differing erosion rates, as it was observed that the erosion rates are either high or low along the same diagonal in a circular specimen. This means that in hydro machines, cavitation erosion rates may also differ greatly, depending on how, for example, the casting process leads to different grain sizes in the machine.

Materials with low steady-state erosion rates and therefore, high cavitation erosion resistances, generally had a higher yield stress. The yield stress, however, cannot be used alone to estimate the erosion rate, as Stainless steel 2 had a slightly higher yield stress than Stainless steel 1, for example, but it also had a higher erosion rate. Furthermore, the low-alloy steel had a higher yield stress than the 7075 aluminum alloy, but both materials eroded at the same rate. This was probably due to the combined effect of corrosion and cavitation erosion.

The material microstructure analysis showed that Stainless steels 1 and 2 consist of almost 100 % martensite and that the first one has a significantly smaller prior austenite grain size. The prior austenite grain size is related to the impact strength and plasticity, so this could explain the difference in erosion rate between these two martensitic steels.

SEM images were taken from three eroded specimens, and they were analyzed to observe the erosion mechanisms. The images showed the dominating erosion mechanism to be, most probably, low-cycle fatigue. Virgin areas were found, with recently removed material and pits resulting from plastic deformations. Cracks and presumably soon-to-be-removed chunks of material were observed throughout the specimens. So-called "beach marks" were also found, indicating towards low-cycle fatigue.

**ACKNOWLEDGMENTS**

The authors would like to thank Business Finland, Fortum Power and Heat Oy, Sandvik Mining and Construction Oy, Valtra Oy, and Teollisuuden Voima Oyj for funding the research and for providing technical support.

## References

[1] Brennen, C. E., "Cavitation Bubble Collapse," *Cavitation and Bubble Dynamics*, Oxford University Press, Oxford, UK, 1995, pp. 80–108.

[2] Avellan, F., "Introduction to Cavitation in Hydraulic Machinery," presented at the *Sixth International Conference on Hydraulic Machinery and Hydrodynamics*, Timisoara, Romania, Oct. 21–22, 2004, Politehnica University of Timişoara, Timisoara, Romania.

[3] Kumar, P. and Saini, R. P., "Study of Cavitation in Hydro Turbines—A Review," *Renew. Sustainable Energy Rev.*, Vol. 14, No. 1, 2010, pp. 374–383, https://doi.org/10.1016/j.rser.2009.07.024

[4] Escaler, X., Egusquiza, E., Farhat, M., Avellan, F., and Coussirat, M., "Detection of Cavitation in Hydraulic Turbines," *Mech. Syst. Sig. Process.*, Vol. 20, No. 4, 2006, pp. 983–1007, https://doi.org/10.1016/j.ymssp.2004.08.006
[5] Berchiche, N., Franc, J. P., and Michel, J. M., "A Cavitation Erosion Model for Ductile Materials," *J. Fluids Eng.*, Vol. 124, No. 3, 2002, pp. 601–606, https://doi.org/10.1115/1.1486474
[6] Franc, J. P., "Incubation Time and Cavitation Erosion Rate of Work-Hardening Materials," *J. Fluids Eng.*, Vol. 131, No. 2, 2009, p. 021303, https://doi.org/10.1115/1.3063646
[7] Franc, J. P., Chahine, G. L., and Karimi, A., "Pitting and Incubation Period," *Advanced Experimental and Numerical Techniques for Cavitation Erosion Prediction*, Springer Dordrecht Heidelberg, Heidelberg, Germany, 2014, pp. 37–69.
[8] Zhou, Y. K. and Hammitt, F. G., "Cavitation Erosion Incubation Period," *Wear*, Vol. 86, No. 2, 1983, pp. 299–313, https://doi.org/10.1016/0043-1648(83)90168-0
[9] Chahine, G. L., Franc, J. P., and Karimi, A., "Mass Loss and Advanced Periods of Erosion," *Advanced Experimental and Numerical Techniques for Cavitation Erosion Prediction*, Springer Dordrecht Heidelberg, Heidelberg, Germany, 2014, pp. 97–121.
[10] ASTM G32-10, *Standard Test Method for Cavitation Erosion Using Vibratory Apparatus*, ASTM International, West Conshohocken, PA, 2010, www.astm.org
[11] Hattori, S., Ishikura, R., and Zhang, Q., "Construction of Database on Cavitation Erosion and Analyses of Carbon Steel Data," *Wear*, Vol. 257, Nos. 9–10, 2004, pp. 1022–1029, https://doi.org/10.1016/j.wear.2004.07.002
[12] Hattori, S. and Kitagawa, T., "Analysis of Cavitation Erosion Resistance of Cast Iron and Nonferrous Metals Based on Database and Comparison with Carbon Steel Data," *Wear*, Vol. 269, Nos. 5–6, 2010, pp. 443–448, https://doi.org/10.1016/j.wear.2010.04.031
[13] Hattori, S. and Ishikura, R., "Revision of Cavitation Erosion Database and Analysis of Stainless Steel Data," *Wear*, Vol. 268, Nos. 1–2, 2010, pp. 109–116, https://doi.org/10.1016/j.wear.2009.07.005
[14] Kendrick, H., Light, M. S., and Caccese, V., *Development of a Cavitation Erosion Resistant Advanced Material System, Report No. UM-MACH-RPT-01-05*, Office of Naval Research, Arlington, VA, 2005, 67p.
[15] Chahine, G. L., Franc, J. P., and Karimi, A., "Laboratory Testing Methods of Cavitation Erosion," *Advanced Experimental and Numerical Techniques for Cavitation Erosion Prediction*, Springer Dordrecht Heidelberg, Heidelberg, Germany, 2014, pp. 21–35.
[16] Soyama, H. and Futakawa, M., "Estimation of Incubation Time of Cavitation Erosion for Various Cavitating Conditions," *Tribol. Lett.*, Vol. 17, No. 1, 2004, pp. 27–30, https://doi.org/10.1023/B:TRIL.0000017415.79517.8c
[17] Karimi, A., "Cavitation Erosion of a Duplex Stainless Steel," *Mater. Sci. Eng.*, Vol. 86, 1987, pp. 191–203, https://doi.org/10.1016/0025-5416(87)90452-6
[18] Karimi, A. and Avellan, F., "Comparison of Erosion Mechanisms in Different Types of Cavitation," *Wear*, Vol. 113, No. 3, 1986, pp. 305–322, https://doi.org/10.1016/0043-1648(86)90031-1
[19] Fortes Patella, R., Choffat, T., Reboud, J., and Archer, A., "Mass Loss Simulation in Cavitation Erosion: Fatigue Criterion Approach," *Wear*, Vol. 300, No. 1, 2013, pp. 205–215, https://doi.org/10.1016/j.wear.2013.01.118
[20] Bathias, C. and Pineau, A., "Low-Cycle Fatigue," *Fatigue of Materials and Structures: Fundamentals*, John Wiley & Sons, New York, NY, 2010, pp. 113–116, https://doi.org/10.1002/9781118623435
[21] Balyts'kyi, O. I. and Chmiel, J., "Resistance of Plate Shipbuilding Steels to Cavitation-Erosion and Fatigue Fracture," *Mater. Sci.*, Vol. 50, No. 5, 2015, pp. 736–739, https://doi.org/10.1007/s11003-015-9779-y

[22] Abouel-Kasem, A., Emara, K. M., and Ahmed, S. M., "Characterizing Cavitation Erosion Particles by Analysis of SEM Images," *Tribol. Int.*, Vol. 42, No. 1, 2009, pp. 130–136, https://doi.org/10.1016/j.triboint.2008.05.008
[23] Laboratoire LEGI, "The PREVERO Cavitation Erosion Tunnel," Laboratoire LEGI, 2018, https://web.archive.org/web/20180327065723/https://www.legi.grenoble-inp.fr/web/spip.php?article1265&lang=fr (accessed 27 March 2018).
[24] Franc, J. P., Riondet, M., Karimi, A., and Chahine, G. L., "Material and Velocity Effects on Cavitation Erosion Pitting," *Wear*, Vols. 274–275, 2012, pp. 248–259, https://doi.org/10.1016/j.wear.2011.09.006
[25] Deplancke, T., Lame, O., Cavaille, J., Fivel, M., Riondet, M., and Franc, J. P., "Outstanding Cavitation Erosion Resistance of Ultra High Molecular Weight Polyethylene (UHMWPE) Coatings," *Wear*, Vols. 328–329, 2015, pp. 301–308, https://doi.org/10.1016/j.wear.2015.01.077
[26] Ylönen, M., Saarenrinne, P., Miettinen, J., Franc, J. P., and Fivel, M., "Cavitation Bubble Collapse Monitoring by Acoustic Emission in Laboratory Testing," presented at the *Tenth International Symposium on Cavitation (CAV2018)*, Baltimore, MD, May 14–16, 2018, Johns Hopkins University, Baltimore, MD—unpublished.
[27] Chahine, G. L., Franc, J. P., and Karimi, A., "Cavitation and Cavitation Erosion," *Advanced Experimental and Numerical Techniques for Cavitation Erosion Prediction*, Springer Dordrecht Heidelberg, Heidelberg, Germany, 2014, pp. 3–20, https://doi.org/10.1007/978-94-017-8539-6
[28] ASTM E112-13, *Standard Test Methods for Determining Average Grain Size*, ASTM International, West Conshohocken, PA, 2013, www.astm.org
[29] Morito, S., Yoshida, H., Maki, T., and Huang, X., "Effect of Block Size on the Strength of Lath Martensite in Low Carbon Steels," *Mater. Sci. Eng. A*, Vols. 438–440, 2006, pp. 237–240, https://doi.org/10.1016/j.msea.2005.12.048
[30] Roy, S. C., 2015, "Modeling and Analysis of Material Behavior during Cavitation Erosion," Ph.D. dissertation, Université Grenoble Alpes, Grenoble, France.
[31] Zavaleta Gutiérrez, N., Luppo, M. I., Danon, C. A., Toda-Caraballo, I., Capdevila, C., and García, D. A., "Heterogeneous Austenite Grain Growth in Martensitic 9Cr Steel: Coupled Influence of Initial Metallurgical State and Heating Rate," *Mater. Sci. Technol.*, Vol. 29, No. 10, 2013, pp. 1254–1266, https://doi.org/10.1179/1743284713Y.0000000271
[32] Kim, H. J., Kim, Y. H., and Morris, Jr., J. W., "Thermal Mechanisms of Grain and Packet Refinement in a Lath Martensitic Steel," *ISIJ Int.*, Vol. 38, No. 11, 1998, pp. 1277–1285, https://doi.org/10.2355/isijinternational.38.1277
[33] Ryl, J., Darowicki, K., and Slepski, P., "Evaluation of Cavitation Erosion-Corrosion Degradation of Mild Steel by Means of Dynamic Impedance Spectroscopy in Galvanostatic Mode," *Corros. Sci.*, Vol. 53, No. 5, 2011, pp. 1873–1879, https://doi.org/10.1016/j.corsci.2011.02.004
[34] MatWeb, "Overview of Materials for Low Alloy Steel," 2018, MatWeb Material Property Data, http://web.archive.org/web/20180921140451/http://www.matweb.com/search/datasheettext.aspx?matguid=d1bdbccde4da4da4a9dbb8918d783b29 (accessed 27 March 2018).
[35] MatWeb, "Aluminum 7075-O," 2018, Matweb Material Property Data, http://www.matweb.com/search/DataSheet.aspx?MatGUID=da98aea5e9de44138a7d28782f60a836&ckck=1 (accessed 27 March 2018).
[36] MatWeb, "Carlson 2205 (UNS S32205) Duplex Stainless Steel," 2018, MatWeb Material Property Data, http://web.archive.org/web/20180921140647/http://www.matweb.com/search/datasheettext.aspx?matguid=086d8b05d09c4963b95253bd278dc4f4 (accessed 27 March 2018).
[37] MatWeb, "AISI Type 304L Stainless Steel," 2018, MatWeb Material Property Data, http://web.archive.org/web/20180921140725/http://www.matweb.com/search/datasheet_print.aspx?matguid=e2147b8f727343b0b0d51efe02a6127e (accessed 27 March 2018).
[38] MatWeb, "Aluminum Bronze, UNS C95400, Copper Casting Alloy, As Cast," 2018, MatWeb Material Property Data, http://web.archive.org/web/20180921140819/http://www.matweb.com/search/datasheettext.aspx?matid=11963 (accessed 27 March 2018).

# PUBLICATION III

**Estimation of Cavitation Pit Distributions by Acoustic Emission**

Ylönen, Markku., Saarenrinne, Pentti., Miettinen, Juha., Franc, Jean-Pierre., Fivel, Marc. & Laakso, Jarmo.

Journal of Hydraulic Engineering. 2019, Volume 146, Issue 2, p. 1-11.
(https://doi.org/10.1061/(ASCE)HY.1943-7900.0001686)

# Estimation of Cavitation Pit Distributions by Acoustic Emission

Markku Ylönen[1]; Pentti Saarenrinne[2]; Juha Miettinen[3]; Jean-Pierre Franc[4]; Marc Fivel[5]; and Jarmo Laakso[6]

**Abstract:** Cavitation erosion in hydraulic machinery, such as in turbines and pumps, often leads to significant reduction of the service life of the affected components, with serious consequences for their maintenance costs and operation efficiency. In this study, the potential contribution of acoustic emission (AE) measurements to the assessment of cavitation damage is evaluated from experiments in a cavitation tunnel. Stainless steel samples were exposed to cavitation and damage was characterized from pitting tests carried out on mirror-polished samples. The pits were measured using an optical profilometer and cavitation damage was characterized by pit diameter distribution. In parallel, AE time signal was measured directly from behind the samples. A dedicated signal-processing technique was developed in order to identify each burst in the AE signal and determine its amplitude. The AE amplitude distribution compares well with PVDF and pressure sensor measurements from literature. It is concluded that AE signal analysis can be used to monitor the formation of pits without visual examination of the damaged surface. This provides a basis for possible future applications of nonintrusive cavitation erosion monitoring in hydraulic machines, provided the findings remain true in a more complex environment. **DOI: 10.1061/(ASCE)HY.1943-7900.0001686.**




## Introduction

Cavitation is a major source of malfunctions in pumps, turbines, and other modern hydraulic applications (Arndt et al. 1989). Cavitation erosion is negligible, for example, in hydraulic turbines operated at their designed optimum conditions. However, the modern tendency is to operate turbines as regulating power sources in the electric grid, because they are flexible and respond quickly to changing power output requirements. This flexibility does not come without a cost. When a turbine is operated outside its best operation point, erosive cavitation may occur. Additionally, quick ramping cannot always be avoided and it can lead to extremely high loads and cavitation effects (Chirag et al. 2018). Some erosion might be tolerated, and some may be avoided, for example, by aerating the areas prone to cavitation (Penghua and James 2018; Gangfu and Hubert 2018), but in-situ knowledge of the actual erosion rate is limited. In these situations, monitoring cavitation damage in real time would be beneficial. The usual way to assess cavitation damage is to visually inspect the turbine during shutdowns in turbine revisions, and repair the turbines if there is too much damage. If reliable information was available during operation, unnecessary shutdowns and costly inspections could be avoided.

To understand the changes in the cavitation behavior of a machine, it would be beneficial to know the cavitation aggressiveness at different operating points. The first step towards such knowledge is to identify how cavitation impacts are distributed in a test rig that isolates cavitation from other phenomena. In this study, cavitation was created on a stainless steel sample in a high-speed cavitation tunnel (PREVERO 2018) and the pits caused by collapsing cavitation bubbles were detected and characterized through acoustic emission (AE) measurements and signal processing.

AE is defined as elastic waves traveling in a solid at a frequency above human hearing threshold (Holroyd 2000; Grosse 2008), typically in the range of 100 kHz to 1 MHz. These waves are detectable by acoustic emission sensors that are sensitive to surface deformations (Ohtsu 2008). The advantage of the AE monitoring method is that AE sensors can be placed outside the cavitation tunnel and there is no need to insert any sensors in the liquid flow. Additional benefits include low cost and fast installation. Only a good transfer path through solid materials is required. The main challenges lie in the interpretation of the data.

AE has been successfully used in monitoring cavitation, with different approaches than the one presented here. Neill et al. (1997) and Poddar and Tandon (2016) were able to detect cavitation incipience, their methods being based on the AE signals root mean squared (RMS) values that increase in amplitude and increasingly fluctuate when cavitation occurs. Analyzing parameters such as RMS and AE event energy and their fluctuation is a common approach, with typically good results (Boorsma and Fitzsimmons 2009;

[1]Doctoral Student, Faculty of Engineering and Natural Sciences, Tampere Univ., Korkeakoulunkatu 6, Tampere 33720, Finland (corresponding author). ORCID: https://orcid.org/0000-0002-0092-2537. Email: markku.ylonen@tuni.fi

[2]Emeritus Professor, Faculty of Engineering and Natural Sciences, Tampere Univ., Korkeakoulunkatu 6, Tampere 33720, Finland. ORCID: https://orcid.org/0000-0003-0279-2884. Email: pentti.saarenrinne@tuni.fi

[3]Docent, Faculty of Engineering and Natural Sciences, Tampere Univ., Korkeakoulunkatu 6, Tampere 33720, Finland. ORCID: https://orcid.org/0000-0002-4485-7140. Email: juha.miettinen@tuni.fi

[4]Emeritus Professor, Grenoble Institut d'ingénierie Université Grenoble Alpes, Laboratoire des Écoulements Géophysiques et Industriels, Univ. Grenoble Alpes, 1209-1211 Rue de la Piscine, Grenoble 38000, France. Email: jean-pierre.franc@legi.cnrs.fr

[5]CNRS Research Professor, Grenoble Institut d'ingénierie Université Grenoble Alpes, Science et Ingénierie des Matériaux et Procédés, Univ. Grenoble Alpes, 101 Rue de la Physique BP46, 38000 Grenoble, France. Email: marc.fivel@simap.grenoble-inp.fr

[6]Project Researcher, Faculty of Engineering and Natural Sciences, Tampere Univ., Korkeakoulunkatu 6, Tampere 33720, Finland. Email: jarmo.laakso@tuni.fi

Note. This manuscript was submitted on November 28, 2018; approved on July 10, 2019; published online on December 12, 2019. Discussion period open until May 12, 2020; separate discussions must be submitted for individual papers. This paper is part of the ***Journal of Hydraulic Engineering***, © ASCE, ISSN 0733-9429.

Boorsma and Whitworth 2011; Schmidt et al. 2014, 2015; Look et al. 2018). However, these calculated parameters lack the detection of individual cavitation impacts, as they tend to be temporally so close to each other that the parameter averaging interprets them as one. The enveloping and peak counting method developed in this study reliably distinguishes individual events, thus providing additional useful information.

Other methods to distinguish individual events include conventional pressure sensors (Franc et al. 2011) and polyvinylidene fluoride (PVDF) sensors that are thin piezoelectric pressure sensors (Hujer et al. 2015; Momma and Lichtarowicz 1995; Wang and Chen 2007; Carrat et al. 2017; Arndt et al. 1997). Notably, the measurements by Hujer et al. (2015) and Franc et al. (2011), which were carried out in the same tunnel, provided exponential cumulative distributions similar to the results extracted from AE signals of this study. Their results were used for qualitative comparison. This proved that the obtained distributions are of the expected type and that AE captures the right events.

The pressures involved in a single cavitation bubble collapse may reach the order of several GPa, as modelled numerically by Hsiao et al. (2014). In the cavitation tunnel used for the current study, the impact loads may be up to 6 GPa in the most aggressive operation condition as estimated by Roy et al. (2015a, b), using an inverse finite element method. They also found that the pit diameters correlate with the bubble size, while the shape factor, which is the ratio between pit depth and pit diameter, correlates with the impact loads. This paper presents relations between distributions of AE peak voltage values and pit diameters. The assumption is that while the pit diameters correlate with bubble size, the bubble size is correlated to the total impact energy and thus the damage potential of the bubble collapse event. The main outcome of this work serves as a basis in moving towards cavitation detection by AE in hydraulic machinery.

## Experimental Program

The aim of this study is to determine a correlation between AE amplitude peak values and pit sizes during the cavitation incubation period. The underlying idea is that the collapse of a cavitation structure should induce both a peak in the acoustic emission signal and a pit on the material surface, provided its intensity is sufficiently high in comparison with the material yield strength. As a result, a strong correlation is expected between the AE peak rate and the pitting rate. To find this correlation, AE was measured from a sample experiencing pitting in a cavitation tunnel (PREVERO 2018). Two tests were conducted with different cavitation aggressiveness, one with a 2 MPa and the other with a 4 MPa tunnel upstream pressure. A higher upstream pressure generates a higher flow velocity and consequently a more aggressive cavitation. It should be noted that the cavitation number was kept constant for the two operating points so that the development of the cavitation structure remained similar and only its intensity was varied. For these two conditions (2 and 4 MPa upstream pressures), the duration of these tests was 6 and 2 min, respectively.

### *Cavitation Tunnel and Sample Preparation*

The experiments were conducted in the PREVERO cavitation tunnel in the LEGI laboratory, Grenoble, France (PREVERO 2018). The cavitation tunnel has a radially diverging test section and it is used for accelerated cavitation erosion testing. The downstream pressure of the tunnel may be varied from ambient pressure to up to 3 MPa absolute pressure, and the upstream pressure may be varied from ambient pressure to up to 4 MPa absolute pressure. The downstream pressure is controlled using a pressurized nitrogen reservoir, and the upstream pressure is regulated by the rotation speed of the circulating pump. The typical temperature rise is in the order of 1°C per hour. Therefore, the temperature rises during the 2- and 6-min tests of this study were not measurable with the current setup and they were assumed to be insignificant.

The test section consists of a nozzle leading to a radially diverging section with a cross-section area smaller than that of the nozzle. The nozzle guides a high-speed water jet towards the stagnation point in the middle of a 100-mm diameter cylindrical material sample, which is flush-mounted to the flow channel. The flow turns 90° and diverges in all directions along the tested sample plane, as the channel transforms to a 2.5-mm thick radially diverging section. When the flow moves from the nozzle to the radial section, the cross-section area of the flow drops by 37.5%. With suitable operating parameters, the static pressure at the inlet of the radially diverging section falls below the critical pressure limit for cavitation inception, assumed to be close to the saturated vapor pressure. Further downstream, as the cross-section area increases, the static pressure increases and the cavitation structures collapse, thus damaging the sample placed in the test section.

Fig. 1(a) presents the cavitation tunnel's simplified schematics, with the downstream tank, pump, and pressure and temperature measurements. The pressures are measured at about 200 mm upstream and downstream from the test section and the pressure loss because of pipe flow is negligible compared to that in the test section. The test section marked in Fig. 1(a) is presented in detail in Fig. 1(b). The flow is diverted after it stagnates in the middle of the inflow nozzle and it is therefore parallel to the sample surface when cavitation occurs. Note that the eroded sample shown in Fig. 1(b) was selected for illustration purposes only, and it is not the same sample that was used in the present study. The one in the figure was eroded for a long duration, much longer than the incubation period length, and it is presented here to visualize the maximum erosion zone. The microscopic pits typical to the incubation period would not be visible in such a photograph. The AE sensor was attached to the sample with the aid of a waveguide, explained further in the text. The dimensions for the waveguide, the tunnel, or the test section are not in scale in Fig. 1.

When the cavitation tunnel is operated at the same cavitation number $\sigma$, the cavitation damage is always located at the same radial position of the cylindrical sample (Gavaises et al. 2015). The cavitation number in the tunnel is defined by Franc et al. (2012)

$$\sigma = \frac{P_d - P_v}{P_u - P_d} \tag{1}$$

where $P_d$ = pressure downstream of the test section, $P_u$ = pressure upstream of the test section, and $P_v$ = the liquid's saturated vapor pressure. A typical value $\sigma = 0.87$ is selected in order to locate the pitting zone at a radius of 22 mm [Fig. 1(b)]. To match the cavitation number, the downstream pressure is adjusted to $P_d = 1.86$ MPa for the 4 MPa upstream pressure and to $P_d = 0.93$ MPa for the 2 MPa upstream pressure.

The material samples in this study were made of a typical stainless steel used in Francis turbine runner blades. The material chemical composition, measured using optical spectrometry, is presented in Table 1.

The material had a tensile yield strength of 808 MPa (0.2% plastic strain) and an ultimate tensile strength of 870 MPa. The microstructure was analyzed by polishing and etching a sample and then observing it with an optical microscope. The microstructure consisted of almost 100% of martensitic phase, with a prior austenite grain size of 109 $\mu$m. The material properties are presented only for the record and they were not thoroughly analyzed here, as they are out of the focus of this study.

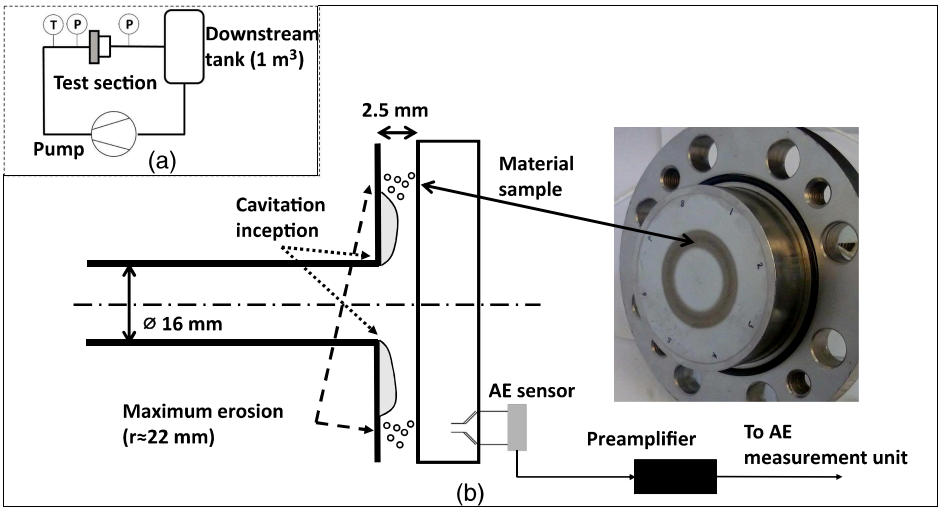


**Fig. 1.** (a) PREVERO cavitation schematics; and (b) tunnel test sections details and material sample.

**Table 1.** Material chemical composition

| Element | Chemical composition (%) |
|---|---|
| Fe | 81.7 |
| C | 0.02 |
| Cr | 12.6 |
| Si | 0.5 |
| Mn | 0.6 |
| P | 0.03 |
| S | 0.005 |
| Ni | 4.2 |
| Mo | 0.5 |

Two samples were prepared, one for each pitting test. The samples were 100-mm diameter and 20-mm thick cylindrical disks, with three screw threads machined in the face opposed to the exposed surface. One thread in the middle to fix the sample in the sample holder and two at diametrically opposed positions and a radial location of 22.5 mm to fix the acoustic emission waveguides into them [Fig. 1(b)]. The flow-side face was mirror-polished. The polishing was performed by grinding the sample with sandpapers of different grit sizes, followed by a polishing step with successive diamond pastes (3- and 1-$\mu$m grain size) and finally with a colloidal silica suspension (0.03-$\mu$m grain size).

### *Pit Detection by Profilometry*

To detect and characterize the pits resulting from cavitation, the sample surface was analyzed by an Alicona Infinitefocus G5 optical profilometer. The measurement technique was microscopy-like imaging based on depth measurement by focus variation. The imaging was done with the aid of a white light source. Light passed to the sample surface through illumination optics, a semitransparent mirror, and an objective lens. Because of the variation in the topography and reflectivity of the sample surface, the light reflected to different directions and partly back to the objective. That light proceeded through imaging mirrors and optics to the charge-coupled device (CCD camera) sensor for focally detecting individual points. The vertical focal position was varied to create sharp images. The altitude coordinate of each point was calculated, from the focal positions in the final sharp image. Fig. 2 presents a typical individual pit imaged by the optical profilometer, with a slightly better

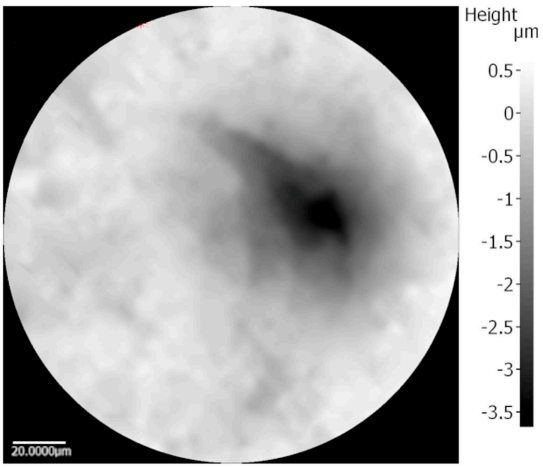


**Fig. 2.** Individual pit imaged by the profilometer.

resolution than used for the measurements performed on the entire eroded sample surface.

The sample surface was mirror-like, excluding the pits that were less reflective than the virgin surface. The pits, such as in Fig. 2, were captured rigorously, but the high reflectivity of the nondamaged surface provided some challenges. In this study, a polarizer was used to generate polarized light illumination and the reflected light was then filtered before it reached the CCD sensor.

The surface topography of the samples were measured with an objective lens of 20x magnification and the measurement of the entire eroded surface was obtained by stitching together multiple pictures into a large panorama. The measurement field area of the 20x objective is 0.81 mm by 0.81 mm and the best vertical resolution is 50 nm. The pits identified in the sample surface were distributed in size and in location. The profilometer data consisted of $X$-$Y$ coordinates and a depth value associated to each point. The grid resolution was 3.5226 $\mu$m by 3.5226 $\mu$m, leading to a minimum pit size of about 200 $\mu$m$^2$, which corresponds to about a 17-$\mu$m equivalent pit diameter.

To post-process the images, the measured sample surface was divided into sections with a maximum area of 1 mm$^2$. This size

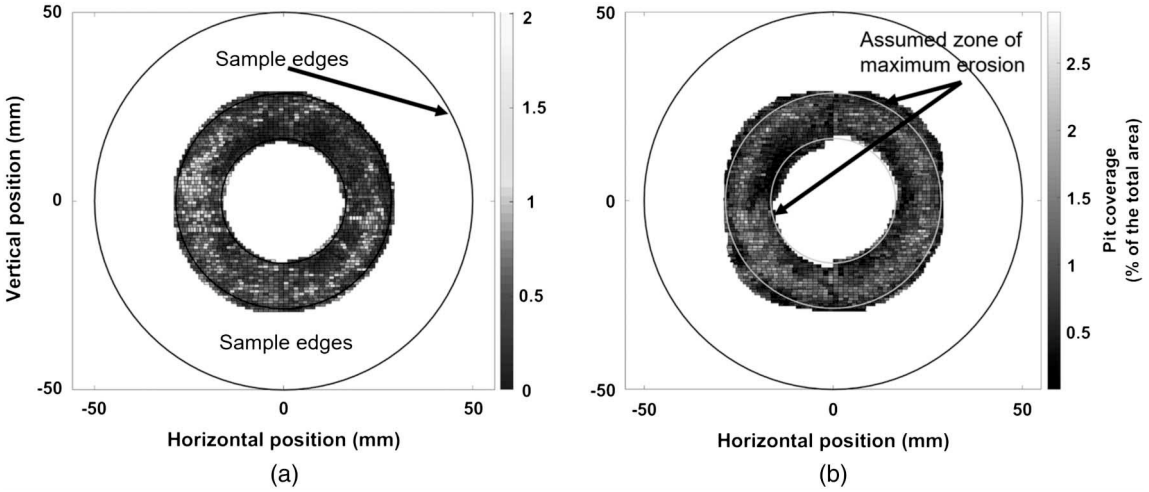


**Fig. 3.** Sample topographic sections analyzed by the optical profilometer for (a) the 2 MPa upstream pressure (6 min exposure); and (b) the 4 MPa upstream pressure (2 min exposure).



was found suitable, as detecting pits from the whole surface in one analysis would have been computationally demanding. Additionally, the measured surface was not completely flat. The overall surface level varied up to 20 $\mu$m from edge to edge of the sample. In a 1 mm$^2$ area, this variation was almost negligible and the surface plane could easily be corrected numerically. Since the center and outer zones are not exposed to cavitation, they were not measured. The surface area was then calculated for each detected pit. The pit coverage was defined as the sum of pit surface areas in a section, divided by section area. The pit coverage estimated from the separately analyzed sections is presented in Figs. 3(a and b), for both the 2 and 4 MPa upstream pressures.

The maximum pit coverage is substantially larger for the 4 MPa upstream pressure, as shown in Fig. 3(b). The respective exposure times were selected to lead to about the same coverage. It is however possible to compare the pitting procedures through pitting rate rather than the total amount of pits. A maximum coverage area was observed in both the samples in a ring-shaped region that corresponds to the cavity closure region, as expected. In long duration tests performed in the tunnel, there is a well-defined radius of maximum erosion rate, which should correspond to the maximum coverage area in the short duration tests. However, this is not apparent in these short duration tests, as observed from the figure. The coverage pattern is not fully axisymmetric, and this is probably a result of the random nature of the cavitation bubble and cloud collapses. Fig. 4 presents some pits detected from the profilometer data. The long scratches remaining in the surface, such as those visible in Fig. 4, were excluded from the pit analysis as explained subsequently.

The pits were first detected by setting a threshold level, and then they were characterized according to their size. The scratches originally detected as pits were elongated, so it was possible to differentiate them from pits resulting from cavitation impacts, using the shape circularity parameter $C$ defined as:

$$C = \frac{4\pi A}{P^2} \tag{2}$$

where $A$ = pit area and $P$ = pit perimeter. A perfect circle has a circularity of 1 and any other shape has a circularity of less than 1. The smaller the circularity is, the more it deviates from a circle. A suitable circularity minimum of $C = 0.75$ was selected by comparing the visualized surface, before and after excluding shapes with

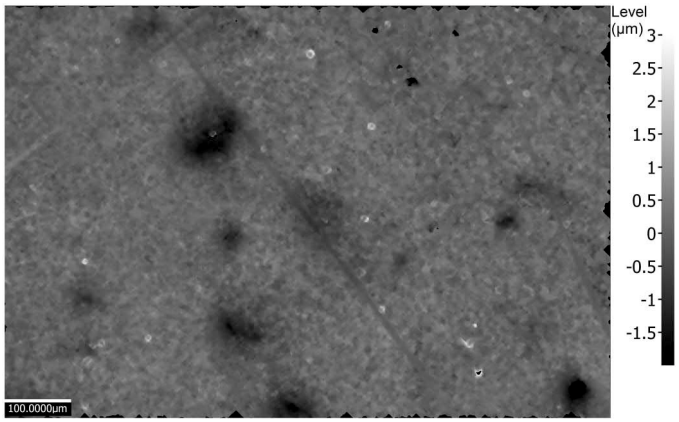


**Fig. 4.** Pit detection from the surface data in the original profilometer image.

different circularity conditions. The pits all had a more or less circular shape ($C > 0.9$) whereas the scratches were noticeably elongated in shape ($C < 0.5$), so it was easy to remove the latter using the threshold value.

### Measurement Uncertainty in Pit Detection

As it was impractical to include the analysis of the measurement uncertainty in the presented figures as error bars, it is discussed separately here. Assuming that the profilometer works reliably and that the algorithm detects all the pits as it should, the main uncertainty concerns the measurement of the pit diameter. The profilometer manufacturer reports a 50-nm vertical resolution, so it was assumed that such a resolution for the depth would not affect the pit detection and the diameter estimations.

Let us now focus on the error induced by the $X$-$Y$ measurements. As previously stated, the pixel size was 3.5226 $\mu$m. The minimum measurable equivalent pit diameter was about 17 $\mu$m, corresponding to five pixels. Thus, the maximum error corresponds to a case where the pit borders are either overestimated or underestimated by the pixel width. In this example, the 5-pixel diameter pit would be measured as a 3- or 7-pixel diameter pit, with erroneous pixels in both sides of the circular pit.

This rough estimate gives the upper limit of the error for the smallest measurable pits ($\pm 7$ $\mu$m), which corresponds to twice the pixel size. The absolute error is approximately the same in the higher diameter range, as the increase or decrease of surface area is always because of an addition of a single pixel. The relative error thus decreases with increasing pit size. However, the error is typically cancelled out at least partially, as it is highly improbable for a pit to have a pixel added or removed to every point in the pit border area. More likely, some parts of the border are overestimated while some parts are underestimated, in a random pattern. Therefore, the 7-$\mu$m error is a highly exaggerated value.

### Acoustic Emission Setup

The acoustic emission sensors were placed behind the samples, without any contact with the water flowing in the test channel. The sensors were fitted to the sample with the help of waveguides, which are steel rods with M8 screw threads in their ends. The waveguides were fixed to the material samples with the screw threads. The AE sensor is a cylinder of 20-mm diameter and 20-mm thickness. It was attached to the other end using a spring load. The waveguide length was 110.9 mm and its diameter was 12.0 mm except in the end with the screw thread. As visualized in Fig. 1(b), the contact between the waveguide and the sample was enhanced by a 90° countersink. To increase the elastic wave propagation through the interface, the contact surfaces were greased between the waveguide, the sensor, and the sample. Shiotani et al. (2016) explain the waveguides and the coupling medium requirements in detail.

The acquisition system was the PAC PCI-2, fitted with two sensors, the PAC R15 and the PAC D9203b, and with PAC 2/4/6 preamplifiers. Only the R15 was found to produce useful measures for the needs of this study. It has a resonance frequency of 160 kHz, as pointed out in Fig. 5 which shows the frequency response chart of the sensor. The main advantage of the R15 sensor is its sensitivity to short duration impacts, which makes it possible to distinguish individual cavitation impacts. This was observed from the waveforms, as the R15 had distinct peaks and only signal noise between impacts, compared to the D9203b that had more constant signal levels. The sampling frequency was 5 MHz, and the voltage resolution was 18 bits, which corresponds to 76 $\mu$V for the 20 V amplitude. The signals were acquired as continuous waveforms throughout the 2- and 6-min tests. The 2/4/6 preamplifier had a 100–400 kHz band-pass analog filter. The signal was also filtered digitally in the acquisition card with the same band-pass.

## Results and Discussion

### Pit Size Distributions

To characterize the pits resulting from cavitation, the following size parameters were calculated for each pit: (1) surface area, (2) volume, (3) depth, and (4) equivalent diameter. The equivalent diameter is the diameter of an equivalent circle:

$$D = \sqrt{\frac{4A}{\pi}} \tag{3}$$

where $D$ = pit diameter and $A$ = pit surface area. Cumulative pit size distributions were found to be suitable for comparison between pit sizes and acoustic emission amplitude peak values. Figs. 6(a–d) presents the cumulative size distributions for all size parameters and for both operation points. The scale is linear—logarithmic.

The cumulative distribution of the pit diameter plotted in Fig. 6(a) was calculated from the pit surface distribution, using Eqs. (3) and (4). This means that the pit diameter distribution is merely proportional to the square root of the pit surface distribution. The pit diameter distribution provided the best fit in exponential distribution, i.e., it had a substantial linear part in the linear—logarithmic scale. For this reason, it was chosen as the parameter of comparison to the AE data. An exponential curve was fitted to the pit diameter distribution, marked with the dashed line in Fig. 6(a). This curve is given by the following equation:

$$\dot{N}_{\text{pit}} = \dot{N}_{0,\text{pit}} e^{-\frac{D}{D_0}} \tag{4}$$

where $\dot{N}_{\text{pit}}$ = cumulative pitting rate, $D$ = pit diameter, and $D_0$ = a reference pit diameter that controls the slope of the pit distribution. $\dot{N}_{0,\text{pit}}$ is the reference pitting rate, equal to the total pitting rate estimated by extrapolating the exponential distribution to $D = 0$. Let us recall here that the profilometer resolution limits the identification to pits having a diameter larger than 17 $\mu$m. For an exponential distribution supposed to be valid for all diameters, it can easily be shown

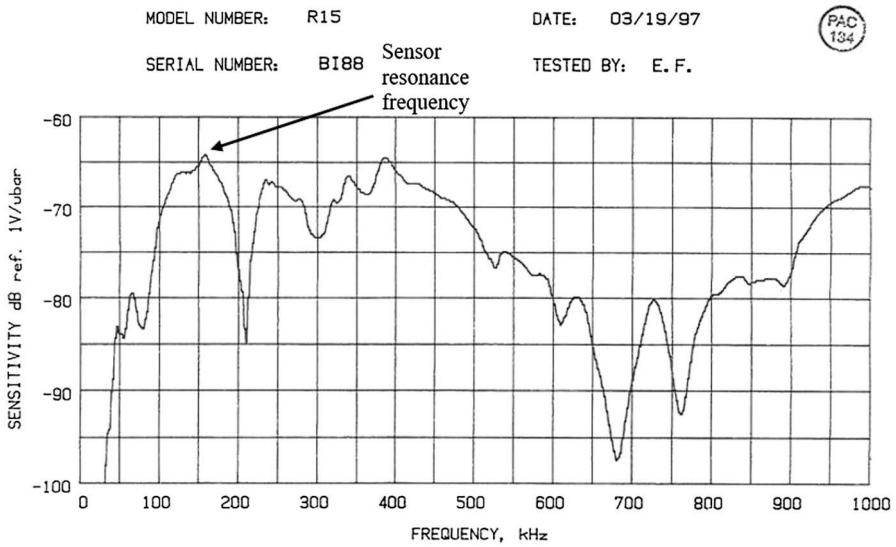


**Fig. 5.** PAC R15 sensor frequency response chart.

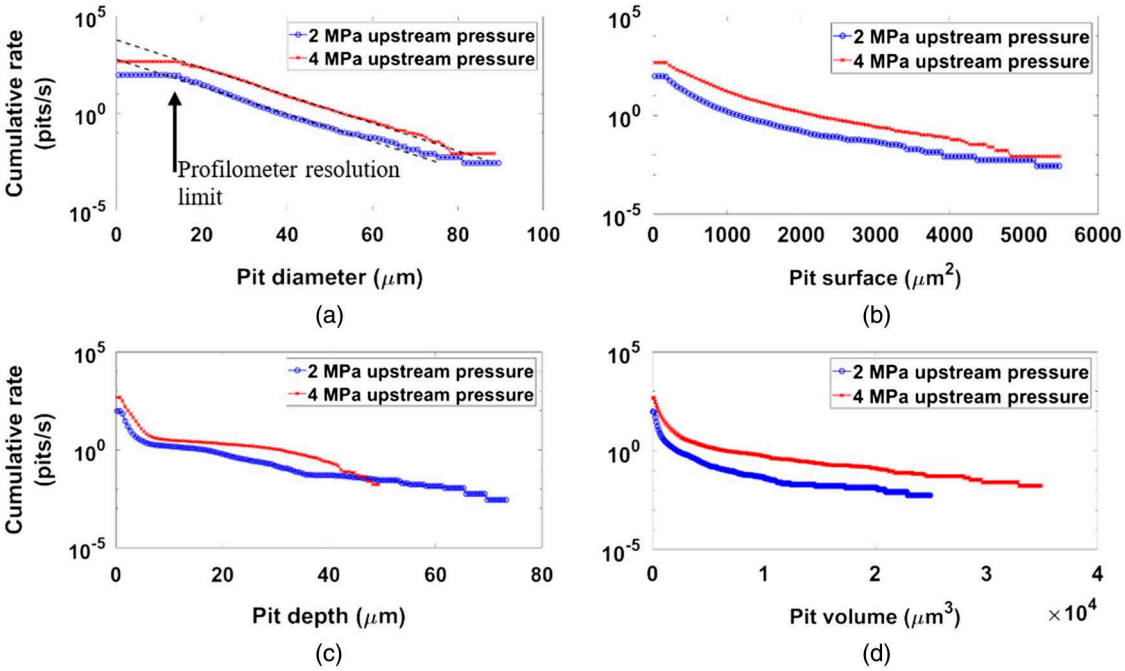


**Fig. 6.** Pit size cumulative distributions for both the 2 and 4 MPa upstream pressures.

that parameter $D_0$ is the mean value of pit diameter over the whole distribution.

### *Acoustic Emission Amplitude Peak Value Distribution*

To detect the events leading to the formation of the pits measured in "Pit Size Distribution," an analysis was performed to the temporal AE signals recorded during the tests. As shown in Fig. 7, the raw AE signal consists of time on the $X$-axis versus voltage on the $Y$-axis. The signal is symmetric in the $Y$-direction, when the sensor is working correctly. A typical example of an AE signal recorded during an erosion test is given in Fig. 7. In Fig. 7, one can count about 40 events for the presented 11 ms window. It corresponds to a rate of about 3,600 events/s. For the full test duration, the rate of events is from 1,200 to 1,400 events/s. This means that the event rate fluctuates significantly and a long enough time window should be considered to ensure statistical convergence of the results.

It was assumed that each burst in the AE signal corresponds to a single cavitation event. As the duration of the cavitation events is sufficiently short, the induced burst signals dissipate fast enough not to overlap with each other significantly. The higher frequency peaks within the bursts were considered as dissipating sensor resonance, as their frequency was close to the sensor resonance frequency of 160 kHz. For example, in the magnification shown in Fig. 7, the average frequency is about 150 kHz, ranging between 128 and 167 kHz. The assumption that the detected AE events correspond to damaging impacts was based on the observations by van Rijsbergen et al. (2012), who found in a hydrofoil that AE sensors attached to its shaft detect only the events occurring close enough to the hydrofoil. To detect each individual event, an envelope function

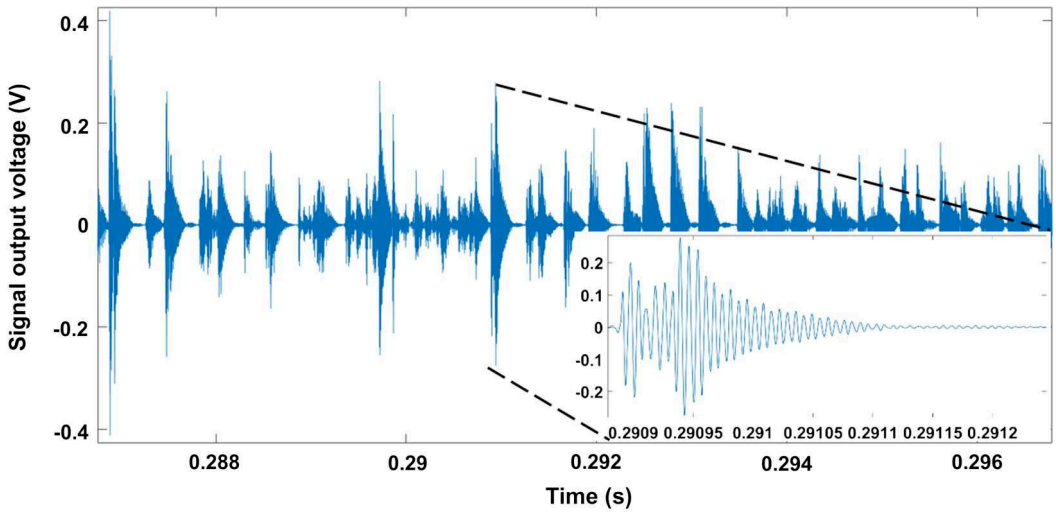


**Fig. 7.** R15 sensor acoustic emission signal in a cavitation test at 4 MPa upstream pressure and a zoom into one of the peaks.

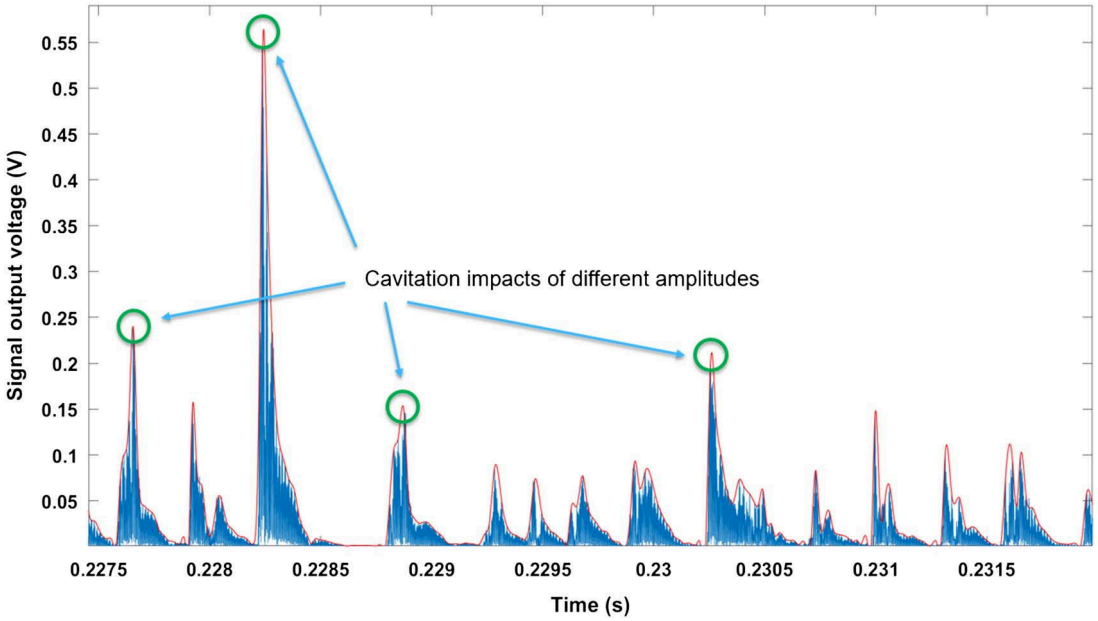


**Fig. 8.** Envelope fit in the absolute value of the acoustic emission signal. The envelope function follows the acoustic emission signal main peaks, and thus ignores the higher frequency resonance effects of the sensor.



was fitted to the absolute values of all the waveforms as shown in Fig. 8. The envelope function was then used to determine the peak values of the signal amplitude.

Using this procedure, the peak values were calculated for both the 2 MPa and the 4 MPa cavitation test, for the full duration of the tests, and the amount of peaks was divided by test duration to calculate the peak rate. The cumulative distribution of the amplitude peak rate, similar to that of the pit sizes in Fig. 6, is presented in Fig. 9(c). For comparison, similar plots based on measurements by Franc et al. (2011) and by Hujer et al. (2015) are also presented in Figs. 9(a and b) respectively. Franc et al. (2011) and Hujer et al. (2015) calculated the impact loads by dropping steel balls on their sensors from different heights, thus obtaining calibration curves for the relation between impact load and peak voltage. This kind of absolute calibration of the AE sensor is not as straightforward as for pressure sensors. As the AE measurement is indirect, the signal amplitude and type depends on the location and installation of the sensor. In the installation of this study, the sensor captures events from the full sample surface, thus the response is not equal for identical impacts on different locations. Thus, the AE voltages were not transformed into any physical parameter, and only relative amplitudes were compared. This is typical in AE applications in general (Broch 1984).

The cumulative distribution for amplitude peak values shown in Fig. 9(c) has a linear part in the semi-log scale diagram, similar to the pit diameter distribution plotted in Fig. 6(a). The 4 MPa curve follows the exponential law for the whole range of data, but the 2 MPa curve tends towards the 4 MPa one for the smaller voltage values. It was assumed that this is because of the noise level arising from machine vibration and possibly from AE induced by the flow. For this reason, the linear curve was fitted only to the linear part of the distribution curve. The noise level was assumed not to vary significantly between operation points; therefore, the lowest amplitude part of the distribution should be the same for both the 2 and the 4 MPa cases. In a similar way to pit distributions, AE peak distributions were approximated by the following exponential law:

$$\dot{N}_{\text{peak}} = \dot{N}_{0,\text{peak}} e^{-\frac{U}{U_0}} \tag{5}$$

where $\dot{N}_{\text{peak}}$ = cumulative peak rate, $U$ = peak voltage value, and $U_0$ = a reference peak amplitude directly related to the slope of the peak voltage value distribution. $\dot{N}_{0,\text{peak}}$ is the total number of AE events corresponding to 0 V. The parameter $U_0$ can be interpreted as the mean amplitude of the peaks, if the exponential distribution law is assumed to remain valid over the whole voltage range.

### Pitting Estimation from Acoustic Emission

It was assumed that the exponential curve, or the linear fit in the semi-log plot, is valid also for the small-scale events, i.e., down to $D = 0$ for pit distributions and down to $U = 0$ for AE peak amplitude distributions. When this assumption is valid, the $Y$-axis intersection of the distributions both for the pit diameter and for the AE peak rate represents the total amount of events. The results of Franc et al. (2011) and Hujer et al. (2015) also support the idea of a continuity of the exponential behavior. Fig. 10 presents a direct comparison between the cumulative pitting rate $\dot{N}_{\text{pit}}$ and the cumulative AE peak rate $\dot{N}_{\text{peak}}$ when plotted as a function of $D/D_0$ and $U/U_0$ respectively.

One can see that the total number of AE amplitude peaks is slightly larger than the total number of pits on the materials. This can be attributed to the signal noise that tends to create large amounts of small amplitude values that shift the cumulative curve to higher levels. The envelope function did not have a threshold level, so when there were no cavitation events, the signal noise was detected as small peaks. In order to improve the comparison between pitting and AE measurements, a parameter called the cut-off voltage ($U_{\text{cutoff}}$) was introduced. It corresponds to the voltage value in the cumulative peak distribution for which the AE peak rate is equal to the total pitting rate extrapolated to $D = 0$. The cut-off voltage can be calculated from the following equation:

$$\frac{\dot{N}_{0,\text{pit}}}{\dot{N}_{0,\text{peak}}} = e^{-\frac{U_{\text{cutoff}}}{U_0}} \tag{6}$$

The cut-off voltage is visualized in Fig. 11. Effectively, the AE amplitude peak values smaller than the cut-off voltage are

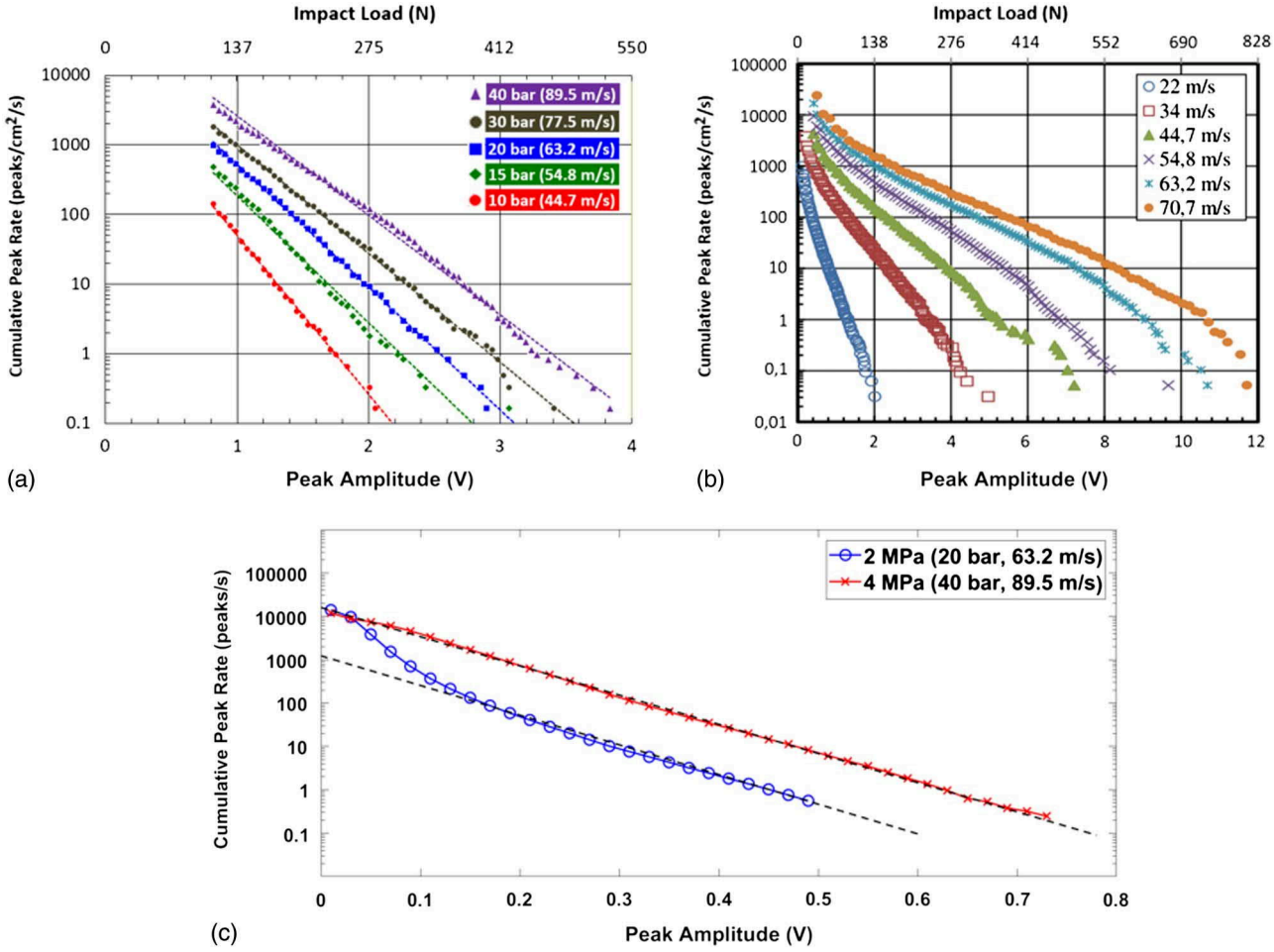


**Fig. 9.** (a) Pressure sensor cumulative peak rates (data from Franc et al. 2011); (b) PVDF sensor cumulative peak rates (data from Hujer et al. 2015); and (c) AE sensor cumulative peak rates in linear—logarithmic scale.

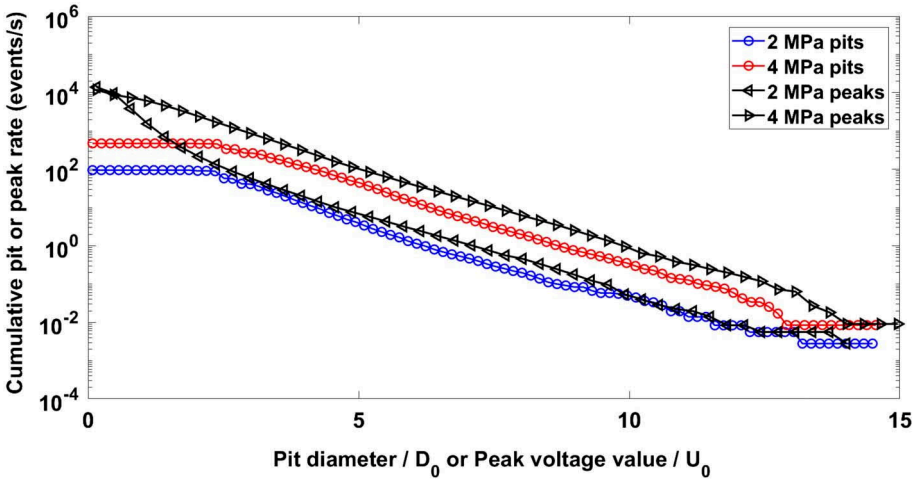


**Fig. 10.** Pit diameters and amplitude peak values normalized by the reference values, and plotted in the same graph. One notices slight overshooting of the peak amplitudes, compared to the pit diameters.

excluded from further calculations. When substituting Eq. (6) into Eq. (5), the AE peak distribution law takes the following form:

$$\dot{N}_{\text{peak}} = \dot{N}_{0,\text{pit}} e^{-\frac{U-U_{\text{cutoff}}}{U_0}} \tag{7}$$

This equation shows that the two exponential laws for the pitting rate [Eq. (4)] and for the AE peak rate [Eq. (5)] overlap when they are plotted as a function of $D/D_0$ or $(U–U_{\text{cutoff}})/U_0$, respectively. As a result, a linear relation was found between amplitude peak value and pit diameter

$$\frac{D}{D_0} = \frac{U - U_{\text{cutoff}}}{U_0} \tag{8}$$

This equation allows transposing AE measurements into pit measurements. The reference values and the cut-off voltages for both the 2 and 4 MPa test cases are presented in Table 2. The total peak rates, i.e., the $Y$-axis intersections in Fig. 9(c), are also listed in the table.

If the distributions are normalized so that the pit diameter is divided by the reference pit diameter, while the cut-off voltage is first subtracted from amplitude peak value and then divided by the reference amplitude peak value, the distributions for both the 2 MPa and the 4 MPa operation points almost perfectly overlap, as shown in Fig. 12.

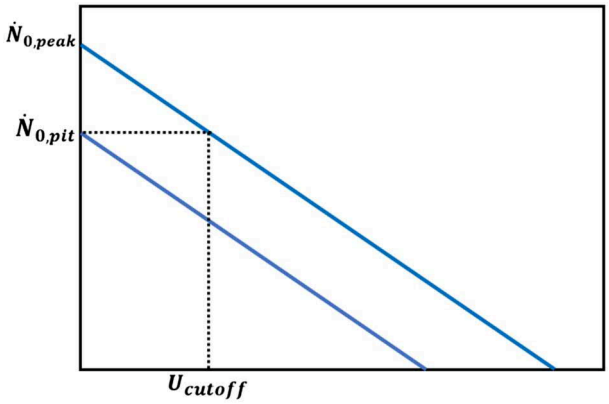


**Fig. 11.** Definition of the cut-off voltage.

**Table 2.** Pitting and AE reference values and cut-off voltages

| Variable | 2 MPa | 4 MPa | Average |
|---|---|---|---|
| $U_{\text{cutoff}}$ (V) | 0.045 | 0.062 | 0.054 |
| $U_0$ (V) | 0.064 | 0.065 | 0.064 |
| $D_0$ ($\mu$m) | 6.17 | 6.08 | 6.13 |
| $U_0/D_0$ (V/$\mu$m) | 97.28 | 94.22 | 95.75 |
| $\dot{N}_{0,\text{pit}}$ (1/s) | 598 | 6,070 | — |
| $\dot{N}_{0,\text{peak}}$ (1/s) | 1,232 | 15,958 | — |

The cut-off voltage $U_{\text{cutoff}}$ is slightly changing with flow aggressiveness since it is 0.045 V at 2 MPa and 0.062 V at 4 MPa. However, compared to the whole range of the AE peak amplitudes, which is approximately 1 V, it may be acceptable to assume that it is almost constant. It can then be conjectured that this threshold is mostly material-dependent and would characterize the limit value of an AE peak that would leave a permanent pit on the material surface. A higher cut-off voltage would likely correspond to a more resistant material. Pitting tests with different materials would be necessary to confirm this trend. The reference parameters $U_0$ and $D_0$ are nearly constant for both the 2 and 4 MPa upstream pressures, as presented in Table 2. This means that by using the relation in Eq. (8), a pit diameter could be defined for each cavitation event, using the AE amplitude peak value. However, since the temporal location of each pit is impossible to detect during the cavitation tests, it was not found possible to relate a single peak voltage value to a single pit diameter. In other words, the presented results are statistically valid, but not necessarily for each individual bubble collapse.

The proposed method is nevertheless promising in monitoring cavitation in hydraulic machines, if developed further. Practically, several steps need to be taken. First, the pitting should be measured for a given operation point and in the area experiencing cavitation, while recording the AE signal. The transfer path from the eroding area to the sensor should be solid, and short enough to avoid significant external disturbances. The exact maximum distance is probably highly case-dependent. Second, the reference parameters $U_0$ and $D_0$ should be defined for the measured operation point. If it is assumed that these reference parameters remain constant in the hydraulic machine as it was in the laboratory testing, the pit diameter distribution could be then estimated for any operation point, as long as there is cavitation. Validating the extension to hydraulic machines is out of the scope of the current study.

## Conclusions

In this study, mirror-polished cylindrical stainless steel samples were subjected to cavitation erosion in a high-speed cavitation tunnel. The exposure to cavitation erosion was 2 min, when the tunnel upstream pressure was 4 MPa, and 6 min when it was 2 MPa. These relatively short exposure times are within the incubation period of cavitation erosion and they ensure that damage is limited to isolated

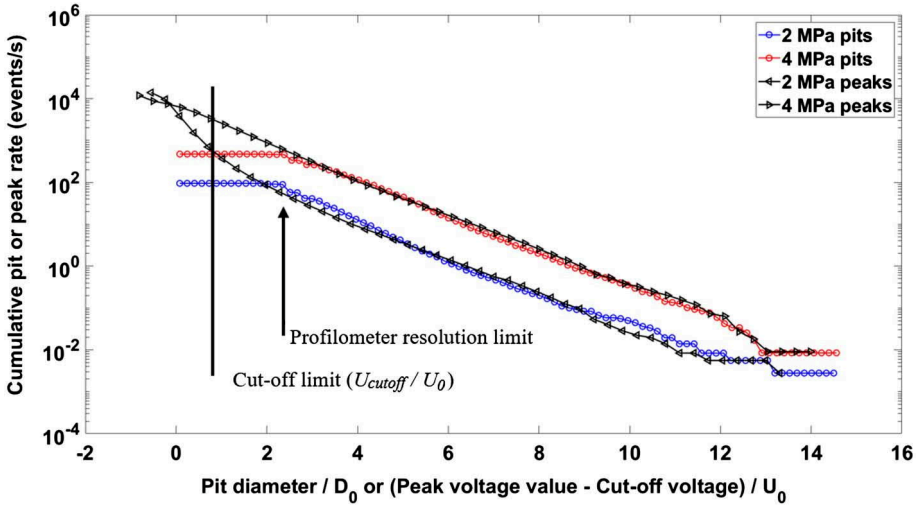


**Fig. 12.** Pitting and AE normalized cumulative distributions.

pits resulting from plastic deformation caused by cavitation bubble or cloud collapses. These pits were detected and measured in three dimensions using an optical profilometer. In parallel, acoustic emission was measured using a 160-kHz resonance frequency sensor with a 5-MHz sampling frequency. The complete waveforms were analyzed by peak counting from an envelope-filtered signal.

A method was presented on how to estimate cavitation pitting from the AE signal, regardless of the cavitation intensity. By introducing parameters such as the cut-off voltage, reference pit diameter and reference amplitude peak value, it was possible to establish a relationship between the cumulative distributions of amplitude peak values and pit diameters. Since the pit diameter correlates with the cavitation bubble size (Roy et al. 2015b), it is a parameter that describes, at least partially, the cavitation bubble distribution in the flow. It could be envisioned that cavitation intensity would be defined from the resulting pit diameters, but this is out of the scope of the current study. The obtained cumulative distributions for the AE signal for the two flow conditions were similar to those published by Franc et al. (2011) for pressure sensors and to those by Hujer et al. (2015) for PVDF sensors. This indicates that AE captures the correct events.

This study is limited to the incubation period of cavitation erosion. Moreover, the tests were conducted on ideal and polished samples with no initial strain, and the test duration was short. In practice, the incubation period characteristics are strongly linked to the long-term erosion rate (Franc 2009; Choi et al. 2012; Soyama and Futakawa 2004; Zhou and Hammitt 1983).

The investigated domain was limited between 2 and 4 MPa upstream pressures, so it may not be concluded that the results could be extrapolated to any situation. The cavitation in the tunnel best corresponds to that in hydrofoils; therefore, it is likely that the same relationship exists for hydrofoil tests. A common feature of the tunnel and of hydrofoils is that they may be operated in conditions leading to cloud cavitation. For extrapolation of this work to other systems, it would be preferred to seek for applications with such a cavitation type.

## Data Availability Statement

Some or all data, models, or code generated or used during the study are proprietary or confidential in nature and may only be provided with restrictions (e.g., anonymized data). All data, including the acoustic emission signal and the profilometer data are the propriety of the Tampere University NEM-project. The corresponding author may ask, on request, a permission from the proprietor to provide the data.

## Acknowledgments

The authors would like to thank Business Finland, Fortum Power and Heat Oy, Sandvik Mining and Construction Oy, Valtra Oy, and Teollisuuden Voima Oyj and Fortum Foundation for funding the research and for providing technical support.

## Notation

*The following symbols are used in this paper:*

$A$ = pit area ($\pi$m$^2$);
$C$ = pit circularity (-);
$D$ = pit diameter ($\pi$m);
$D_0$ = pit reference diameter ($\pi$m);
$\dot{N}_{\text{peak}}$ = peak rate (1/s);
$\dot{N}_{\text{pit}}$ = pitting rate (1/s);
$\dot{N}_{0,\text{peak}}$ = reference peak rate (1/s);
$\dot{N}_{0,\text{pit}}$ = reference pitting rate (1/s);
$P$ = pit perimeter ($\pi$m);
$P_d$ = downstream pressure (Pa);
$P_u$ = upstream pressure (Pa);
$P_v$ = vapor pressure (Pa);
$U$ = amplitude peak value (V);
$U_{\text{cutoff}}$ = cut-off voltage (V);
$U_0$ = reference amplitude peak value (V); and
$\sigma$ = cavitation number (-).

## References

Arndt, R. E., P. Saurav, and C. R. Ellis. 1997. "Application of piezoelectric film in cavitation research." *J. Hydraul. Eng.* 123 (6): 539–548. https://doi.org/10.1061/(ASCE)0733-9429(1997)123:6(539).

Arndt, R. E., R. L. Voigt, J. P. Sinclair, R. Peter, and F. Antonio. 1989. "Cavitation erosion in hydroturbines." *J. Hydraul. Eng.* 115 (10): 1297–1315. https://doi.org/10.1061/(ASCE)0733-9429(1989)115:10(1297).

Boorsma, A., and P. Fitzsimmons. 2009. "Quantification of cavitation impacts with acoustic emissions techniques." In *Proc., 7th Int. Symp. on Cavitation*, 1–6. Red Hook, NY: Curran Associates.

Boorsma, A., and S. Whitworth. 2011. "Understanding the details of cavitation." In *Proc., 2nd Int. Symp. on Marine Propulsors*, 1–9. Hamburg, Germany: Institute for Fluid Dynamics and Ship Theory, Hamburg Univ. of Technology.

Broch, T. J. 1984. "Acoustic emission." In *Mechanical vibration and shock measurement*, 214–219. 2nd ed. Denmark: Bruel & Kjaer.

Carrat, J., R. Fortes-Patella, and J. Franc. 2017. "Assessment of cavitating flow aggressiveness on a hydrofoil: Experimental and numerical approaches." In *Proc., ASME 2017 Fluids Engineering Division Summer Meeting*. New York: ASME.

Chirag, T., A. Einar, and O. G. Dahlhaug. 2018. "Experimental investigation of a Francis turbine during exigent ramping and transition into total load rejection." *J. Hydraul. Eng.* 144 (6): 04018027. https://doi.org/10.1061/(ASCE)HY.1943-7900.0001471.

Choi, J., A. Jayaprakash, and G. L. Chahine. 2012. "Scaling of cavitation erosion progression with cavitation intensity and cavitation source." *Wear* 278–279 (Mar): 53–61. https://doi.org/10.1016/j.wear.2012.01.008.

Franc, J. 2009. "Incubation time and cavitation erosion rate of work-hardening materials." *J. Fluids Eng.* 131 (2): 021303. https://doi.org/10.1115/1.3063646.

Franc, J., M. Riondet, A. Karimi, and G. L. Chahine. 2011. "Impact load measurements in an erosive cavitating flow." *J. Fluids Eng.* 133 (12): 121301. https://doi.org/10.1115/1.4005342.

Franc, J., M. Riondet, A. Karimi, and G. L. Chahine. 2012. "Material and velocity effects on cavitation erosion pitting." *Wear* 274–275: 248–259. https://doi.org/10.1016/j.wear.2011.09.006.

Gangfu, Z., and C. Hubert. 2018. "Effects of step and cavity shapes on aeration and energy dissipation performances of stepped chutes." *J. Hydraul. Eng.* 144 (9): 04018060. https://doi.org/10.1061/(ASCE)HY.1943-7900.0001505.

Gavaises, M., F. Villa, P. Koukouvinis, M. Marengo, and J. Franc. 2015. "Visualisation and les simulation of cavitation cloud formation and collapse in an axisymmetric geometry." *Int. J. Multiphase Flow* 68 (Jan): 14–26. https://doi.org/10.1016/j.ijmultiphaseflow.2014.09.008.

Grosse, C. 2008. *Acoustic emission testing*. Berlin: Springer.

Holroyd, T. 2000. *Acoustic emission and ultrasonics handbook: Coxmoor's machine & system condition monitoring*. Moreton-in-Marsh, UK: Coxmoor Publishing Co.

Hsiao, C., A. Jayaprakash, A. Kapahi, J. Choi, and G. L. Chahine. 2014. "Modelling of material pitting from cavitation bubble collapse." *J. Fluid Mech.* 755: 142–175. https://doi.org/10.1017/jfm.2014.394.

Hujer, J., J. Carrat, M. Müller, and M. Riondet. 2015. "Impact load measurements with a PVDF pressure sensor in an erosive cavitating flow." *J. Phys. Conf. Ser.* 656 (012051): 1–4. https://doi.org/10.1088/1742-6596/656/1/012051.

Look, A., O. Kirschner, S. Riedelbauch, and J. Necker. 2018. "Detection and level estimation of cavitation in hydraulic turbines with convolutional neural networks." In *Proc., 10th Int. Symp. on Cavitation (CAV2018)*, 1–4. New York: ASME.

Momma, T., and A. Lichtarowicz. 1995. "A study of pressures and erosion produced by collapsing cavitation." *Wear* 186 (Part 2): 425–436. https://doi.org/10.1016/0043-1648(95)07144-X.

Neill, G. D., R. L. Reuben, P. M. Sandford, E. R. Brown, and J. A. Steel. 1997. "Detection of incipient cavitation in pumps using acoustic emission." *Proc. Inst. Mech. Eng.* 211 (4): 267–277. https://doi.org/10.1243/0954408971529737.

Ohtsu, M. 2008. "Sensor and instrument." In *Acoustic emission testing*, edited by C. Grosse and M. Ohtsu, 19–40. Berlin: Springer.

Penghua, T., and Y. James. 2018. "Modeling and prototype testing of flows over flip-bucket aerators." *J. Hydraul. Eng.* 144 (12): 04018069. https://doi.org/10.1061/(ASCE)HY.1943-7900.0001531.

Poddar, S., and N. Tandon. 2016. "Detection of journal bearing vapour cavitation using vibration and acoustic emission techniques with the aid of oil film photography." *Tribol. Int.* 103 (Nov): 95–101. https://doi.org/10.1016/j.triboint.2016.06.039.

PREVERO. 2018. "The PREVERO cavitation erosion tunnel." Accessed October 25, 2018. http://web.archive.org/web/20180327065723/http://www.legi.grenoble-inp.fr/web/spip.php?article1265&lang=fr.

Roy, S. C., J. Franc, and M. Fivel. 2015a. "Cavitation erosion: Using the material as a pressure sensor." *J. Appl. Phys.* 118 (16): 164905. https://doi.org/10.1063/1.4934747.

Roy, S. C., J. Franc, N. Ranc, and M. Fivel. 2015b. "Determination of cavitation load spectra—Part 2: Dynamic finite element approach." *Wear* 344–345 (Dec): 120–129. https://doi.org/10.1016/j.wear.2015.09.005.

Schmidt, H., O. Kirschner, and S. Riedelbauch. 2015. "Cavitation measurements on a pump-turbine model." *J. Phys. Conf. Ser.* 656 (012051): 1–4. https://doi.org/10.1088/1742-6596/656/1/012071.

Schmidt, H., O. Kirschner, S. Riedelbauch, J. Necker, E. Kopf, M. Rieg, G. Arantes, M. Wessiak, and J. Mayrhuber. 2014. "Influence of the vibro-acoustic sensor position on cavitation detection in a Kaplan turbine." In Vol. 22 of *Proc., IOP Conf. Series: Earth and Environmental Science*, 1–9. Bristol, UK: IOP Publishing.

Shiotani, T., Y. Mizutani, H. Nakamura, and S. Yuyama. 2016. "Practical AE testing, data recording and analysis." In *Practical acoustic emission testing*, 67–72. New York: Springer.

Soyama, H., and M. Futakawa. 2004. "Estimation of incubation time of cavitation erosion for various cavitating conditions." *Tribol. Lett.* 17 (1): 27–30. https://doi.org/10.1023/B:TRIL.0000017415.79517.8c.

van Rijsbergen, M., E. Foeth, P. Fitzsimmons, and A. Boorsma. 2012. "High-speed video observations and acoustic-impact measurements on a NACA 0015 Foil." In *Proc., 8th Int. Symp. on Cavitation (CAV 2012)*, 958–964. Singapore: Research Publishing Services.

Wang, Y., and Y. Chen. 2007. "Application of piezoelectric PVDF film to the measurement of impulsive forces generated by cavitation bubble collapse near a solid boundary." *Exp. Therm Fluid Sci.* 32 (2): 403–414. https://doi.org/10.1016/j.expthermflusci.2007.05.003.

Zhou, Y., and F. G. Hammitt. 1983. "Cavitation erosion incubation period." *Wear* 86 (2): 299–313. https://doi.org/10.1016/0043-1648(83)90168-0.

# PUBLICATION IV

**Shedding Frequency in Cavitation Erosion Evolution Tracking**

Ylönen, Markku., Franc, Jean-Pierre., Miettinen, Juha., Saarenrinne, Pentti. & Fivel, Marc.

Journal of Multiphase Flow. 2019, Volume 118, p. 141-149.
(https://doi.org/10.1016/j.ijmultiphaseflow.2019.06.009)

International Journal of Multiphase Flow 118 (2019) 141–149

Contents lists available at ScienceDirect

International Journal of Multiphase Flow

journal homepage: www.elsevier.com/locate/ijmulflow

# Shedding frequency in cavitation erosion evolution tracking

Markku Ylönen[a,*], Jean-Pierre Franc[b], Juha Miettinen[a], Pentti Saarenrinne[a], Marc Fivel[c]

[a] Tampere University, Faculty of Engineering and Natural Sciences, Korkeakoulunkatu 6, 33720 Tampere, Finland
[b] Univ. Grenoble Alpes, CNRS, Grenoble INP, LEGI, 38000 Grenoble, France
[c] Univ. Grenoble Alpes, CNRS, Grenoble INP, SIMaP, 38000 Grenoble, France

ARTICLE INFO

*Article history:*
Received 21 January 2019
Revised 6 May 2019
Accepted 12 June 2019
Available online 13 June 2019

*Keywords:*
Cavitation erosion
Cloud cavitation
Shedding frequency
Acoustic emission

ABSTRACT

Cavitation erosion is a concern for most hydraulic machinery. An especially damaging type of cavitation is cloud cavitation. This type of cavitation is characterized by a growth-collapse cycle in which a group of vapor bubbles first grows together in a low-pressure region and then collapses almost simultaneously when the pressure recovers. Measuring the frequency of these collapse events is possible by acoustic emission (AE), as demonstrated in this study, in which a cavitation tunnel is utilized to create cloud cavitation in the vicinity of a sample surface. These samples were equipped with AE sensors, and the initially high frequency AE signal was demodulated to detect the relatively low frequency cloud cavitation shedding. It was found that when the cavitation number is increased, AE successfully detects the changes in this frequency, confirmed by comparing the results to video analysis and to simulations from literature. Additionally, the frequency increases when cavitation erosion progresses, thus providing means to track the erosion stage. It is concluded that the presented method is suitable for both detecting the transition from cloud to sheet cavitation and the erosion evolution in the experimental cavitation tunnel. The method could probably be extended to non-intrusive hydraulic machine monitoring, as this type of cloud cavitation is common in hydrofoils.



## 1. Introduction

Cavitation is characterized by the growth and collapse of vapor bubbles in a liquid. It can be observed either in a static liquid or in a liquid flow due to decrease and the subsequent recovery of the static pressure. The collapse of these bubbles potentially damages adjacent surfaces, as a result of the cumulated plasticity induced at micrometer scale by each bubble collapse. Since the bubbles are typically quite numerous and the duration of exposure to cavitation is generally long, damage tends to accumulate and reach macroscopic levels. This causes serious harm to the structural integrity and flow performance of hydraulic machines, pipes, and valves. This damage is typically difficult to avoid when searching for the maximum benefit of an equipment at the expense of the ideal conditions of use. Additionally, the extent of erosion is not usually well known during operation, as it is difficult to monitor in situ. Cavitation often occurs inside flow channels, where continuous visual observation may be difficult and costly, if not impossible.

This study focuses on cloud cavitation, which is a common type of cavitation observed in various hydraulic equipment and in particular in hydrofoils. Cloud cavitation is a highly eroding type of cavitation. A cloud of vapor bubbles forms in the leading edge of a hydrofoil, due to an increase in the flow velocity, which leads to the decrease in static pressure. It travels downstream the foil, and collapses towards the trailing edge, if the static pressure recovers sufficiently along the foil. The cloud is not static; it grows and collapses periodically following a mechanism of growth, formation of a re-entrant flow, shedding, and collapse. The shedding frequency depends on flow velocity, surface quality, overall pressure, temperature and surrounding liquid quality. (Brennen et al., 2000; Franc and Michel, 2005; Nishimura et al., 2014; Gnanaskandan and Mahesh, 2016; Hsiao et al., 2017)

The current study can be divided into two main approaches in detecting and utilizing the shedding frequency: (1) finding the correlation between the cavitation number and the cloud shedding frequency via acoustic emission (AE) and confirming the results through comparison to high-speed video analysis and to simulation results by other authors, and (2) tracking cavitation erosion evolution through shedding frequency measured via AE. Material samples that were fitted with AE sensors were eroded in a cavita-

* Corresponding author.
*E-mail addresses:* markku.ylonen@tuni.fi (M. Ylönen), jean-pierre.franc@legi.cnrs.fr (J.-P. Franc), juha.miettinen@tuni.fi (J. Miettinen), pentti.saarenrinne@tuni.fi (P. Saarenrinne), marc.fivel@simap.grenoble-inp.fr (M. Fivel).

https://doi.org/10.1016/j.ijmultiphaseflow.2019.06.009
0301-9322/

tion tunnel that creates cloud cavitation. Changes in the cloud cavitation shedding frequency is not a common way to monitor cavitation erosion, but with the approach in this study, it proved to be an efficient method. A series of erosion tests were conducted, along with a 'ramp test' to study the effects of the cavitation number. In the ramp test, the cavitation number was gradually increased, to study the changes in the cloud shedding phenomenon.

Acoustic emission is defined as elastic waves traveling in a solid material (Holroyd, 2000; Grosse, 2008). These elastic waves are the result of energy released in the material. The energy release may be due to changes in internal stresses, external impacts or surface contacts. As an AE source, cavitation represents external impacts, resulting from bubble collapses near a solid boundary. AE has a wide frequency band, resulting from wave front reflections in the solid medium, the range being typically from 100 kHz to 1 MHz (Pollock, 1986). Two main types of sensors exist: the resonance type and the broadband sensor, with the main difference being the damping properties in sensor structure. They are placed on a solid surface that has a good transfer path to the signal source. AE is a tempting method in monitoring cavitation, as it is non-intrusive and sensors can be placed in the machine structure. The main challenge is the interpretation of the results, as the signal voltage is not easily transformed into any physical quantity (Ohtsu et al., 2016; Achenbach, 1975; Inaba, 2016; Trampe Broch, 1984).

As far as the authors know, AE has been used in cavitation detection and erosion intensity evaluation, but not in erosion evolution tracking. AE detects the incipience of cavitation efficiently (Alfayez and Mba, 2005; Neill et al., 1997), enabling early detection of possibly harmful cavitation, for example in journal bearing lubrication films (Poddar and Tandon, 2016). Potentially damaging cavitation occurs typically close to surfaces. Indeed, bubbles collapsing in the free flow induce pressure shocks, but do not damage the surfaces that are located far away. Therefore, properly placed AE sensors detect only the collapses occurring near the fluid/structure interface that lead to impacts towards the material surface (van Rijsbergen et al., 2012). The non-damaging collapse events happening far away from the surface lead to no significant sensor response.

The presented approach begins by demonstrating the applicability of AE in shedding frequency monitoring by comparing the detected frequencies to those calculated from a video analysis and to those from simulations by Gavaises et al. (2015). Then, the method is used in tracking how the frequency changes when the material surface erodes, thus modifying the flow field in the cavitation test section. The presented method provides an effective way to monitor changes in cloud shedding frequency, due to erosion evolution or changes in flow velocity, provided the cloud shedding phenomenon is pronounced enough.

## 2. Experimental program

In the experiments, two different stainless steel samples were eroded in a high-speed cavitation tunnel, while recording AE signal. A 'ramp test' of varying cavitation number was also performed. The authors of Gavaises et al. (2015) provided their video recordings of the cavitation tunnel, which were completely reanalyzed in this study to complement the AE results concerning the cavitation cloud shedding frequencies.

### 2.1. Testing equipment and procedure

The cavitation test rig was the PREVERO cavitation tunnel (PREVERO, 2018). The data acquisition board was a PAC PCI-2, with two sensors: the PAC R15D resonance type sensor, and the PAC D9203b broadband sensor, both used with a PAC 2/4/6 preamplifier. The preamplifier had a 100 kHz to 400 kHz band-pass analogue

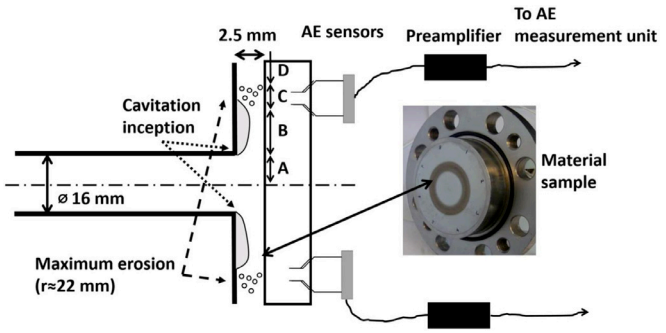


**Fig. 1.** Schematics of the cavitation tunnel test section and the AE setup, and a photograph of an eroded material sample fixed to the sample holder. Areas A-D are later used in the video analysis in Figs. 3-7.

filter for the R15D and a 100 kHz to 1200 kHz one for the D9203b. The sampling rate was 5 MHz per channel. The data-acquisition software was PAC AEWin$^{TM}$ and the signals were further analyzed in Matlab$^{TM}$.

The cavitation tunnel consists of a water loop, a test section, a pump, and a pressurizing tank, along with pressure, temperature, and flow meters. The tunnel is pressurized by an external nitrogen tank connected to the downstream tank of the tunnel. Below the downstream tank is the pump that has a frequency regulator to control rotation speed, therefore controlling the upstream pressure and flow velocity of the tunnel. On the same level with the downstream tank is the test section where cavitation occurs. The pressure loss in the test section is the dominating pressure loss source in the tunnel. The cavitation tunnel was operated with a constant cavitation number of 0.87 for the mass loss tests, and with a varying cavitation number for the ramp test. The cavitation number $\sigma$ in the tunnel is defined as (Franc et al., 2012):

$$\sigma = \frac{P_d - P_v}{P_u - P_d} \tag{1}$$

where $P_u$ is the tunnel upstream pressure or the pressure before the test section, $P_d$ is the tunnel downstream pressure or the pressure after the test section, and $P_v$ is the saturated vapor pressure. A constant cavitation number, regardless of the overall pressure level, leads to equal radial position of the cavitation closure on the material sample (Gavaises et al., 2015). The pressure difference $P_u$–$P_d$ is linked to the overall flow velocity, which is a significant contributor to cavitation aggressiveness. If the upstream pressure is increased, the cavitation number decreases; therefore, to retain a constant cavitation number, the downstream pressure needs to be increased. The rise in overall pressure level corresponds to the increase of cavitation aggressiveness (Franc et al., 2012).

The samples are cylinders of 100 mm diameter and 20 mm thickness. They have one flat, uniform, and initially mirror-polished face for cavitation erosion tests. The other face, or the back of the sample, is used for fixing the sample to the sample holder by a screw in the center. The test section is an axisymmetric, radially diverging channel, one channel wall being the tested material sample. The nozzle directs a water jet in the middle of the sample, where the water flow stagnates and diverges radially. The flow cross section area drops to 62.5% from the original, thus dropping the static pressure under the critical value for cavitation inception. As the flow further diverges and the static pressure increases due to increasing cross section area, cavitation closes, leading to erosion of the sample and flow channel surface. Cavitation occurs parallel to the sample surface. Fig. 1 illustrates the test section and the cavitation inception and closure, along with a photograph of an eroded material sample fixed to the sample holder. Areas A-D correspond to areas later used in defining the different areas in

the video analysis. A is the nozzle area, where the flow stagnates, B is the area of the growth of the cavitation cloud, C is the cavitation closure area, between 19 mm and 32 mm radial position from the centerline if $\sigma \approx 0.9$, and D is the area where cavitation is no longer observed.

The two tested samples were made of martensitic stainless steel and they were named stainless steel 1 and stainless steel 2. They were exposed to cavitation erosion for about 65 h. Both of them were specimens from Francis turbine runner blades. The material properties do not have any significance in the current approach, as the analysis concentrated on the shedding frequency, which is linked to the flow rather than the surface material. This study utilizes the data of the volume loss measurements by Ylönen et al. (2018), where the material properties were thoroughly examined. Therefore, the volume loss curves later used in this study correspond to the ones previously presented in Ylönen et al. (2018).

Volume loss and erosion depth were calculated from surface profiles that were measured with a Taylor-Hobson Form Talysurf 50 contact profilometer. The sample profile was measured along eight equally divided azimuthal angles of the sample. The measurement was from the center towards the edge of the circular sample surface. The surface profiles were mostly measured in five-hour intervals, excluding the beginning of the tests, where the interval was reduced to thirty minutes or two hours. The upstream pressure was 4 MPa and the downstream pressure was 1.9 MPa for the volume loss tests, corresponding to the maximum aggressiveness of the cavitation tunnel.

In the ramp test, the cavitation number was increased from well-developed cavitation up to the point where cavitation disappears, and further on to non-cavitating flow. The cavitation number was increased gradually by decreasing the upstream pressure, while keeping the downstream pressure constant. The initial upstream pressure was 4 MPa and it was gradually decreased down to 2.3 MPa, while the downstream pressure was maintained at 1.9 MPa. Cavitation disappeared when $\sigma \approx 2.8$, the observation based on audible noise and on the significant drop in AE levels.

### 2.2. Video analysis

The videos were courtesy of Professor M. Gavaises and coworkers, who performed a detailed analysis of the cavitation structures in the tunnel and measured the corresponding shedding frequencies (Gavaises et al., 2015). They conducted a vast campaign with different operating points, but for the present study, only five videos were selected, corresponding to the operation points within the ramp tests. They were filmed from the side where the sample would normally be located, and with the sample being replaced by a Perspex window. The videos covered only a partial area of the tunnel test section. For more information, the filming procedure is explained in detail by Gavaises et al. (2015). In this study, these five videos were reanalyzed using a slightly different approach; the video analysis was based on a FFT analysis of the gray level of each pixel.

The videos were recorded with a frame rate of 77,000 frames per second. The visualized area was 34 × 16 mm$^2$, the pixel size was 132 × 125 μm$^2$, the image size was 256 x 128 pixels and the video was directly recorded in grayscale. The video lengths in terms of number of frames and the operation points of the cavitation tunnel are presented in Table 1.

For each pixel in the video, the grayscale value was captured and the values were picked frame by frame. An example of a video frame is presented in Fig. 2.

The most interesting areas in the images are B and C. Area A was masked for the video analysis and area D has no cavitation. The grayscale value as a function of time was obtained for each individual pixel and for all five videos, and they were analyzed via FFT. The frequency resolution is limited by the frequency bin size $f_{bin}$:

$$f_{bin} = F_s * \frac{L}{2} \tag{2}$$

where $F_s$ is frame rate and $L$ is the video length in frames. The videos were all relatively short, C30 being the shortest one with 2895 frames. This gives a frequency bin size $f_{bin}$ of 51.5 Hz. Therefore, the peak frequency values have an uncertainty of +/− 26 Hz. This was considered acceptable, since the shedding frequencies were above 1600 Hz, so that the relative error was in the order of 2%.

The frequency maps for the analyzed videos with different values of the cavitation number $\sigma$ are presented in Figs. 3-7. The zero and close to zero frequencies in the A and D regions correspond to the masked nozzle area and the downstream area with no cavitation. In Fig. 7, a large part of the area, including regions B and C, had no measurable frequencies. In all videos, several individual pixels were found having a more than 10 kHz frequency. They were interpreted as local anomalies, and therefore they were excluded from further analysis. The dominating frequency, where it is well definable, was assumed to correspond to cavitation cloud shedding frequency. Figs. 3 and 4 present the peak frequency maps for relatively low cavitation numbers ($0.8 < \sigma < 1.0$).

The dominating frequency for $\sigma = 0.811$ in Fig. 3 cannot be well defined. Three major frequency zones were identified: 798 Hz,

**Table 1**
Video lengths and the operation points of the cavitation tunnel.

| Video ID | Cavitation number $\sigma$ | Upstream pressure (MPa) | Downstream pressure (MPa) | Length (frames) |
|---|---|---|---|---|
| C27 | 1.897 | 2.909 | 1.905 | 1738 |
| C28 | 1.515 | 3.166 | 1.907 | 1495 |
| C29 | 1.159 | 3.562 | 1.912 | 1356 |
| C30 | 0.908 | 4.027 | 1.916 | 1331 |
| C31 | 0.811 | 4.273 | 1.913 | 2895 |

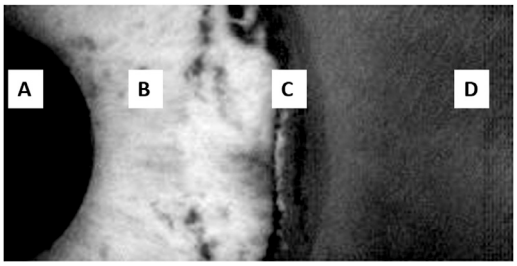


**Fig. 2.** An individual frame from video C30. Area markers: (A) Flow stagnation from the nozzle, covered for filming, (B) Cavitation cloud growth, (C) Cavitation closure and (D) No cavitation. The areas (A-D) are also presented in Fig. 1.

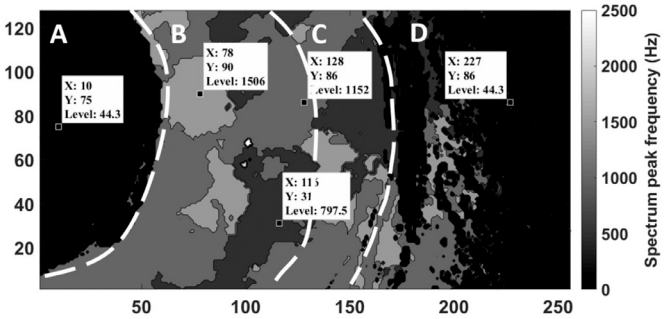


**Fig. 3.** Frequency map of $\sigma = 0.811$. The *X* and *Y*-axes represent the pixel coordinates in a video frame.

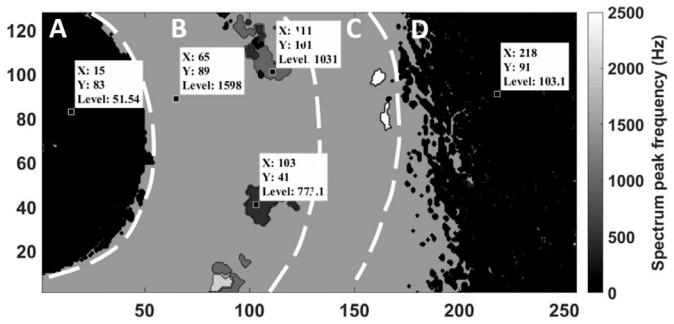


**Fig. 4.** Frequency map of $\sigma = 0.908$. The $X$ and $Y$-axes represent the pixel coordinates in a video frame.

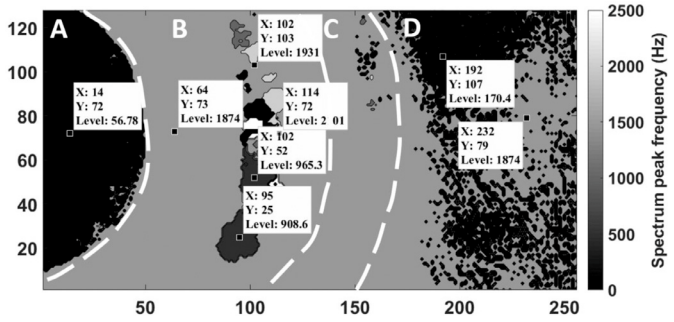


**Fig. 5.** Frequency map of $\sigma = 1.159$. The $X$ and $Y$-axes represent the pixel coordinates in a video frame.

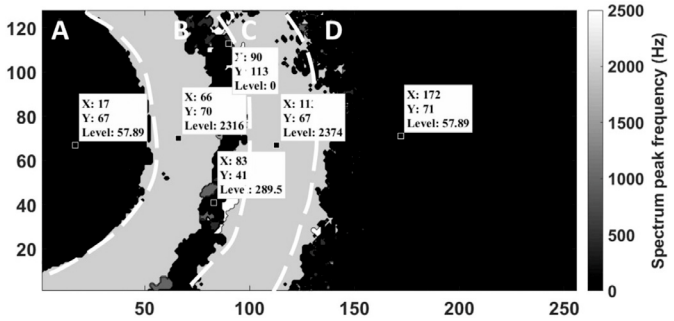


**Fig. 6.** Frequency map of $\sigma = 1.515$. The $X$ and $Y$-axes represent the pixel coordinates in a video frame.

1152 Hz and 1506 Hz, the largest in area being 1152 Hz. The 1506 Hz would be in line with the other results, and it is the one presented in the comparison of methods later on. Longer videos might have made the results more representable, but none was available. When $\sigma = 0.908$ in Fig. 4, the dominating frequency is clearly 1598 Hz. Figs. 5 and 6 present the peak frequency maps for higher cavitation numbers, where cloud shedding is still observed ($1.1 < \sigma < 1.6$).

When $\sigma = 1.159$ in Fig. 5, the dominating frequency of 1874 Hz can be clearly identified. When $\sigma = 1.515$ in Fig. 6, two different dominating frequencies were observed: 2316 Hz and 2374 Hz, and between them, a narrow band of multiple different frequencies. It is notable that the two dominating frequencies represent neighboring frequency bins. Therefore, they probably represent a single frequency that happens to be close to the average of these two frequencies. As the frequency resolution is limiting the observations, 2374 Hz was picked as the cloud shedding frequency for $\sigma = 1.515$, as it is located in the area of cavitation closure (region C). In Fig. 7, the cavitation number is so high ($\sigma = 1.897$) that presumably the shedding phenomenon ceases to exist, at least in a significant scale. Using the same color map as for the other figures,

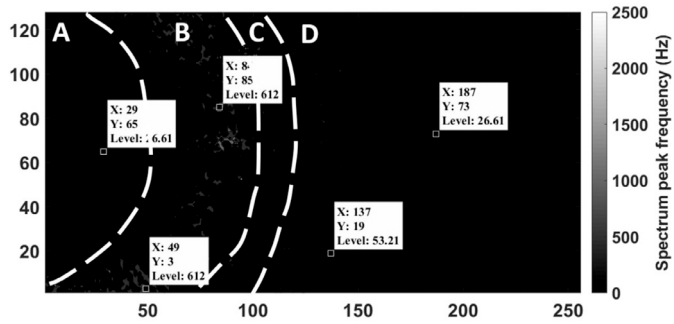


**Fig. 7.** Frequency map of $\sigma = 1.897$. The $X$ and $Y$-axes represent the pixel coordinates in a video frame.

Fig. 7 is almost completely black, as only small areas with peak frequencies of several hundreds of Hz were detected, observed as gray areas in the figure.

When $\sigma$ increases, the cavitation cloud shedding becomes less and less pronounced. A similar disappearance of a dominating frequency was found in the AE signal analysis, as shown in the next section. Therefore, it seems that the cloud shedding phenomenon is well observable only with low cavitation numbers, as also noted by Gavaises et al. (2015). This suggests a transition from cloud cavitation to sheet cavitation, when the cavitation number is increased (Pelz et al., 2017).

## 3. Acoustic emission signal processing

The initial goal in this study was to track changes in AE energy, RMS-value, peak frequencies, and amplitudes when cavitation erosion evolves. This was tempting, as the acquisition system automatically tracked these parameters. It was found that the values did fluctuate and their levels changed during the cavitation tests, but no proper trend was found in the current study. Therefore, these parameters were disregarded, in favor of another approach.

Raw voltage signal was also recorded during the erosion, in roughly one-hour intervals for a five-minute acquisition time, except for the first sixty minutes that were recorded in full. The sampling frequency was 5 MHz. He and Shen (2012) stated that the signal average energy would have a good correlation with the mass loss rate in their tests using an ASTM G32-10 (ASTM, 2010) vibratory cavitation testing apparatus. However, the present investigation did not confirm their observation, since no clear correlation between the signal average energy and the mass loss rate could be found.

To validate that AE properly captures cavitation events, the AE signals from several different cavitation numbers are presented in Fig. 8. The exact voltages that are induced by cavitation are not important in this study, but comparing amplitudes in Fig. 8 clearly shows that when cavitation disappears, the AE levels drop over a hundred-fold compared to the fully-developed cavitation. The operating condition in Fig. 8D has practically no cavitation, but dropping the cavitation number about 0.2 would lead to the inception of cavitation. Fig. 8A and B represent conditions where cloud shedding was observed in the video and AE analysis, while Fig. 8C corresponds to cavitation with assumedly no pronounced cloud growth-collapse cycle.

The signal amplitudes might correlate with the strength of cavitation erosion, but the current approach was based on signal frequencies. The frequency responses of the AE sensors are rather non-linear. This means that the frequency content of the signals is highly colored with the sensor frequency response. Therefore, the initially observed maximum frequency from raw voltage signals is usually the peak value of the sensor frequency response.

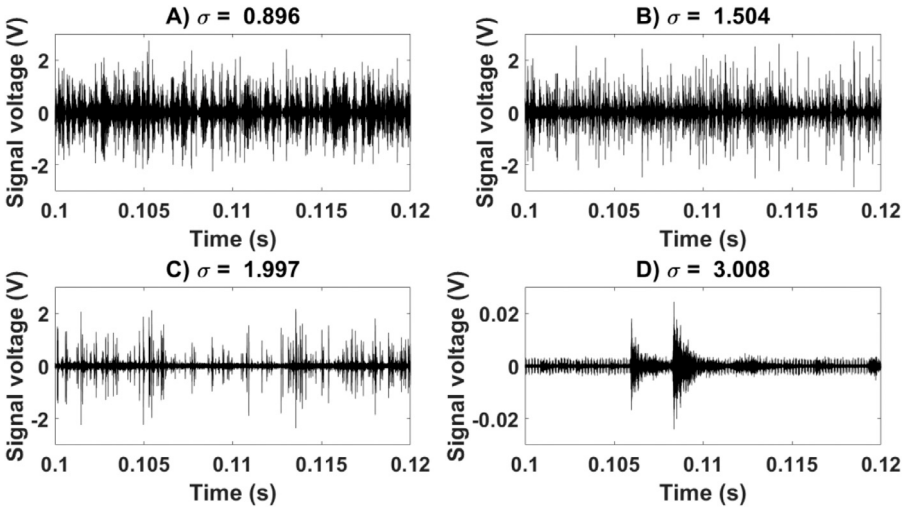


**Fig. 8.** AE signal voltage levels for varying cavitation numbers. (A) and (B) represent fully developed cavitation with cloud shedding, (C) represents cavitation that is assumed to be sheet cavitation, and (D) represents a cavitation number where cavitation no longer occurs.

Based on the results by Gavaises et al. (2015), it was expected that the cavitation cloud shedding frequency would be at several thousand Hz. The AE signals were band-pass filtered with a lower limit frequency of 100 kHz, so it could be expected that the low frequency shedding could not be detected. However, it is detectable using signal demodulation techniques. Events, such as cavitation cloud shedding, occurring at lower frequencies, have a high frequency content inside them that is not lost in the filtering process. At time intervals corresponding to the shedding frequency, a rise in AE activity is observed, the signal frequencies inside the shedding event being in the sensor frequency range.

Berry (1997a) utilized a waveform enveloping and demodulation technique to promote low frequency content in signals. This method provides a possibility to e.g. track bearing failures (Berry, 1997b). The method works with any signal that has low frequency content that is of note, but that is not properly detectable using direct spectral analysis, and provided that the high frequency content acts as a modulated carrier signal. The demodulation process in this study was essentially similar to that of Berry, although signal enveloping was performed according to the description by Marple Jr (1999). The procedure, modified from the description by the previous authors to suit the needs of the current signals, was the following:

1) AE signal was first measured with band-pass filtering from 100 kHz to 400 kHz or 100 kHz to 1200 kHz, depending on the sensor. At that stage, the signal contained also the high frequency modes of the repeating shedding events. The low frequencies of the shedding were “hidden” in the high frequency content.
2) The signal average was subtracted, with the average value saved for later corrections
3) A Fast Fourier Transform (FFT) was performed on the zero-averaged signal. Note that the average was initially close to zero, since AE signals generally should be close to symmetric around zero volts.
4) The frequency domain one-sided discrete-time analytic signal was calculated, with the mathematical formulation in Marple Jr (1999).
5) The discrete-time analytic signal magnitude was calculated via inverse FFT (IFFT). This corresponds to the creation of an envelope of the original signal. The original signal average was added to the enveloped signal. The modulated carrier signal is lost at this point, so the low frequency contents are promoted.
6) A low-pass filter was applied, with the decimation of the signal. The low-pass filter was an eighth-order Chebyshev Type I low-pass filter, the default option of the Matlab™ function ‘decimate’. The decimation resampled the signal with a lower frequency, to reduce sample sizes, in addition to the low-pass filtering. The original sampling rate was not required, as the high frequency content was filtered out at this point.
7) The filtered signals were then transformed to frequency domain by Welch’s method. The window size was 5000 samples and the window overlapping was 50%.
8) The two frequencies with the highest amplitudes were then detected and saved for further analysis.

The demodulation process effectively promotes the low frequency content in the signal; the low frequency content exists also in the non-demodulated frequency data, but it is usually lost because the high frequency content is dominating. Fig. 9 presents the FFT analysis of both an original and a demodulated signal. Note that the shedding frequency is observable from the original data, but not reliably, as the high frequency amplitudes are about ten orders of magnitude larger.

## 4. Results

### 4.1. Shedding frequency in the ramp tests

The ramp test went through a set of experimental conditions ranging from well-developed cavitation to no cavitation state of the cavitation tunnel. All the AE waveforms were demodulated, for both sensors. Typically, two distinguishable peak frequencies were detected, as in Fig. 9. The peak frequencies as a function of the cavitation number are presented in Fig. 10. The higher frequency peaks were interpreted as the first harmonic of the shedding frequency, as its frequency was always two times the lower one, and it was excluded from further analysis. Each marker in Fig. 10 represents a thirty-second interval. Six of these were measured and analyzed for each cavitation number. The first harmonic is also marked in Fig. 10, to highlight that it follows the same trend as the actual shedding frequency.

Both the resonance type sensor (R15D) and the broadband sensor (D9203b) detect the same frequency, in most cases. The linear growth in frequencies is lost after $\sigma > 1.75$, although already at $\sigma = 1.75$, the frequencies begin to be scattered. The consistency in detecting a shedding frequency was lost between $\sigma \approx 1.5$ and

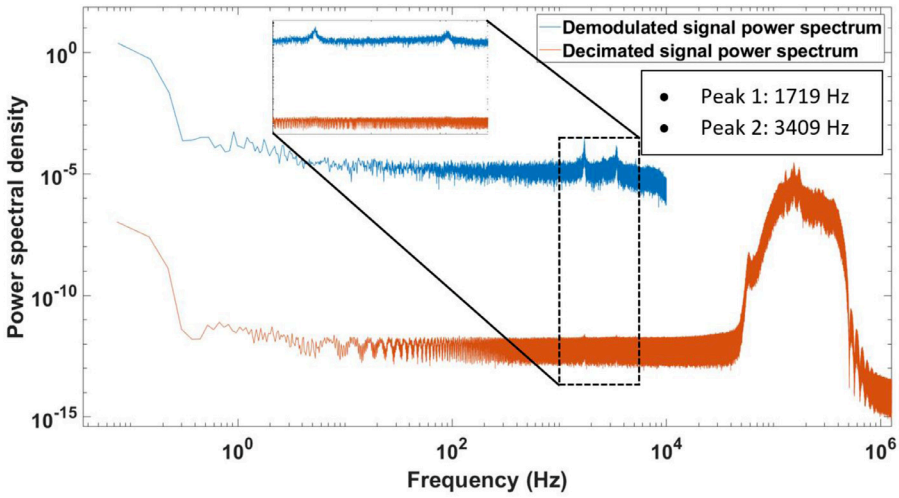


**Fig. 9.** The demodulated signal power spectral density compared to that of the original signal.

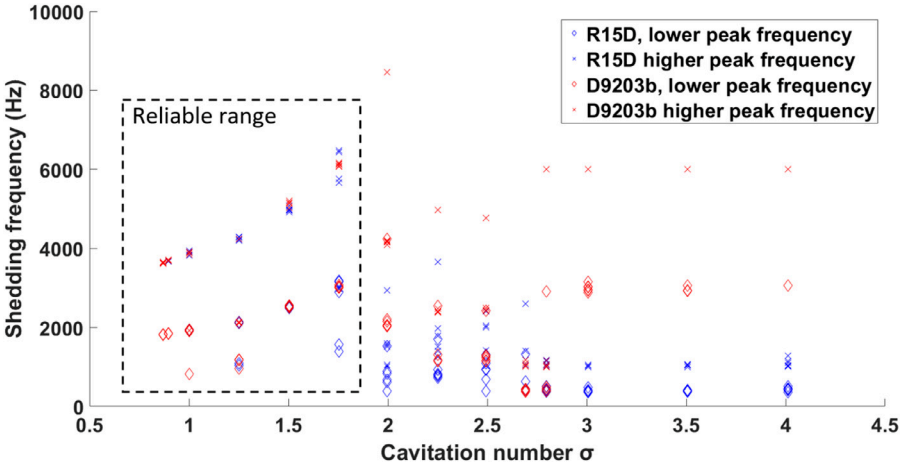


**Fig. 10.** Cavitation shedding frequency, and its first harmonic, measured by AE as a function of cavitation number. The diamond markers indicate the lower peak frequency, which is assumed to be the shedding frequency, while cross markers indicate the first harmonic.

$\sigma \approx 1.8$ also in the video analysis. This suggests that the shedding phenomenon ceases to exist, when the cavitation number exceeds a certain limit.

### 4.2. Shedding frequency: comparison between AE and videos

This section aims to evaluate the AE capability in capturing the correct shedding frequency. The AE frequencies deduced from the demodulation process are now compared to the shedding frequencies found from the video analysis and the simulation results by Gavaises et al. (2015), who simulated the erosion via computational fluid dynamics (CFD), using a hybrid RANS/LES model. A key result of theirs, in the scope of this study, was the relation between the cavitation number and the shedding frequency, reprinted with permission in Fig. 11.

Gavaises et al. (2015) simulated multiple downstream pressures ($P_{back}$). For each pressure level, the shedding frequency clearly increases with increasing cavitation number. A lower downstream pressure corresponds to a lower shedding frequency. In this study, the analysis was limited to 1.9 MPa, or 19 bar downstream pressure, so only those values were kept for Fig. 12, which compares all the three different methods to determine the shedding frequency when the cavitation number is varied.

The error bars in the video analysis are the result of the FFT bin size. The largest bin size was 51.5 Hz, so the maximum error was rounded to +/− 30 Hz. The AE result standard deviation was always less than 12 Hz between the thirty-second intervals, therefore it was not feasible to visualize in the figure. Fig. 12 shows that all the three different methods are in good agreement. It is thus concluded that the shedding frequency can be captured reliably and with sufficient accuracy from AE measurements, provided the presented demodulation processing technique is applied. The result is valid at least for the cavitation tunnel. At this stage, the validity of the method is only demonstrated in the case of the cavitation tunnel but is expected that this remains true for other experimental conditions.

### 4.3. Shedding frequency from AE and cavitation erosion

The previous results demonstrated that AE captures the proper shedding frequency. In this section, a similar analysis is carried out for cavitation erosion tests, in order to highlight a potential drift in shedding frequency with changing surface geometry. The material samples, referred to as stainless steel 1 (SS1) and stainless steel 2 (SS2), were eroded from a virgin non-eroded surface to approximately 400-$\mu$m maximum erosion depth. Both samples were exposed to cavitation for 65 h to reach this state. Stainless steel 2 eroded more in volume and average erosion depth than stainless steel 1; therefore, it had an inferior resistance to cavitation, already stated by Ylönen et al. (2018).

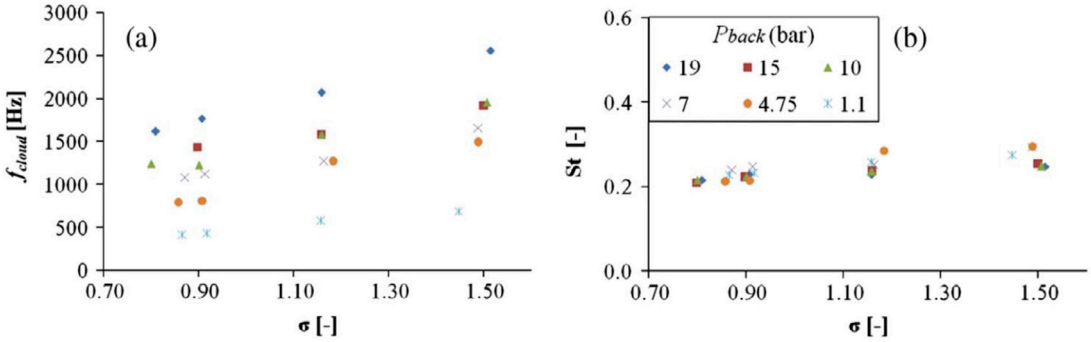


**Fig. 11.** (a) Simulated shedding frequency as a function of the cavitation number in the cavitation tunnel by Gavaises et al. (2015). (b) The Strouhal number *St* was defined as the ratio of shedding frequency multiplied by the gap size of 2.5 mm and the mean flow velocity at the 25 mm radius of the diverging channel. Reprinted from Gavaises et al. (2015), Fig. 15, Copyright 0301-9322/© 2014 Elsevier Ltd, with permission from Elsevier.

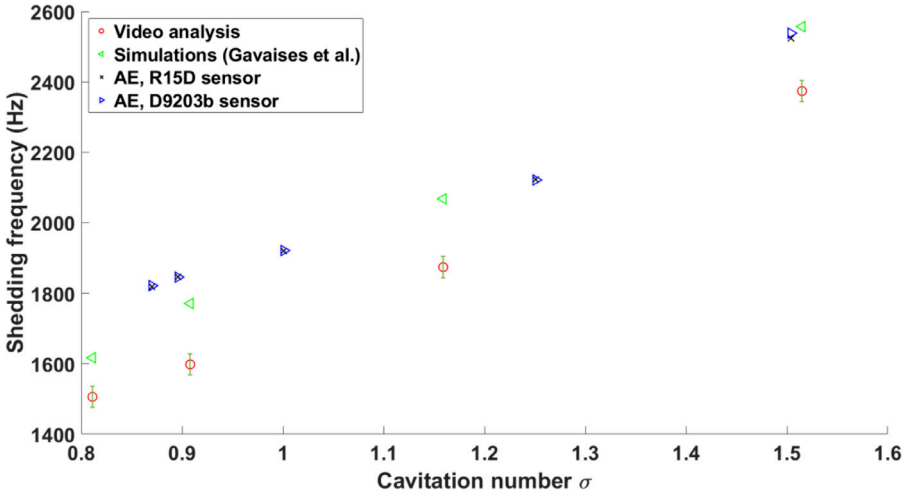


**Fig. 12.** Comparison of the results by Gavaises et al. (2015), the video analysis, and the AE measurements, regarding the relation between the shedding frequency and the cavitation number.

AE was measured at one- to two-hour intervals, excluding the beginning of the tests, where it was measured continuously. The waveforms were collected for five minutes at each interval, and the five-minute waveform was split into thirty-second sections that were individually analyzed, following the demodulation algorithm. Fig. 13A presents the evolution of the shedding frequency, for both samples and both AE sensors. The volume losses and erosion depths for both samples are presented in Fig. 13B. Fig. 13C presents the shedding frequency as a function of volume loss, while Fig. 13D presents the shedding frequency as a function of erosion depth. The erosion depth was defined as the maximum profile depth at each measurement point.

It is notable that the shedding frequency, the volume loss and the erosion depth of stainless steel 2 (SS2) begins to increase faster than those of stainless steel 1 (SS1), after about 12 h of erosion, or roughly after the cavitation incubation period. During the incubation period, the surface deformation rate is slower than in the advanced periods, meaning that the increase in roughness is smaller. After 48 h of erosion, the slopes of the shedding frequency curves begin to decrease, reaching possibly a constant value. This suggests that the changes in roughness might have little effect when the surface is highly damaged. After a critical level of roughness, the shedding frequency seems to become roughness independent. This is, however, not possible to confirm in the limited scope of this investigation.

When plotting the shedding frequency as a function of volume loss in Fig. 13C and erosion depth in Fig. 13D, the plots for the two different tests and materials overlap to a significant degree. This suggests that the shedding frequency is a parameter that is linked only to the surface deformation of the samples. The relation is linear at least between 0 and 100 $mm^3$ volume loss, or between 0 and 350 $\mu$m erosion depth. It should be noted that the shedding frequency tends to fluctuate, so deriving a volume loss or an erosion depth out of the shedding frequency measurement would only lead to a rough estimate of the actual values.

When the material surface is degraded, the resulting surface roughness leads to modifications in the flow field and therefore in the shedding phenomenon. The increase in shedding frequency with the increase in roughness is consistent with the results by Hao et al. (2017). Their rough hydrofoil experiencing cloud cavitation had a 20 Hz shedding frequency, whereas for a smooth one in equal conditions, the frequency was 17 Hz. They explained the difference by the rough surface having a more complex flow pattern, including initial and large-scale shedding, with a different type of attachment to the surface. In contrast to these results and the results in this study, Stutz (2003) found no effect of roughness in the case of a cavitation sheet. This suggests that a cavitation cloud is more sensitive than a cavitation sheet to changes in surface roughness.

The shedding frequency is a well-definable parameter in cloud cavitation. Therefore, measuring its change in a hydraulic machine would give information about the state of cavitation erosion. Acoustic emission is a promising option for measuring the frequency, as the sensors can be placed outside the flow and the

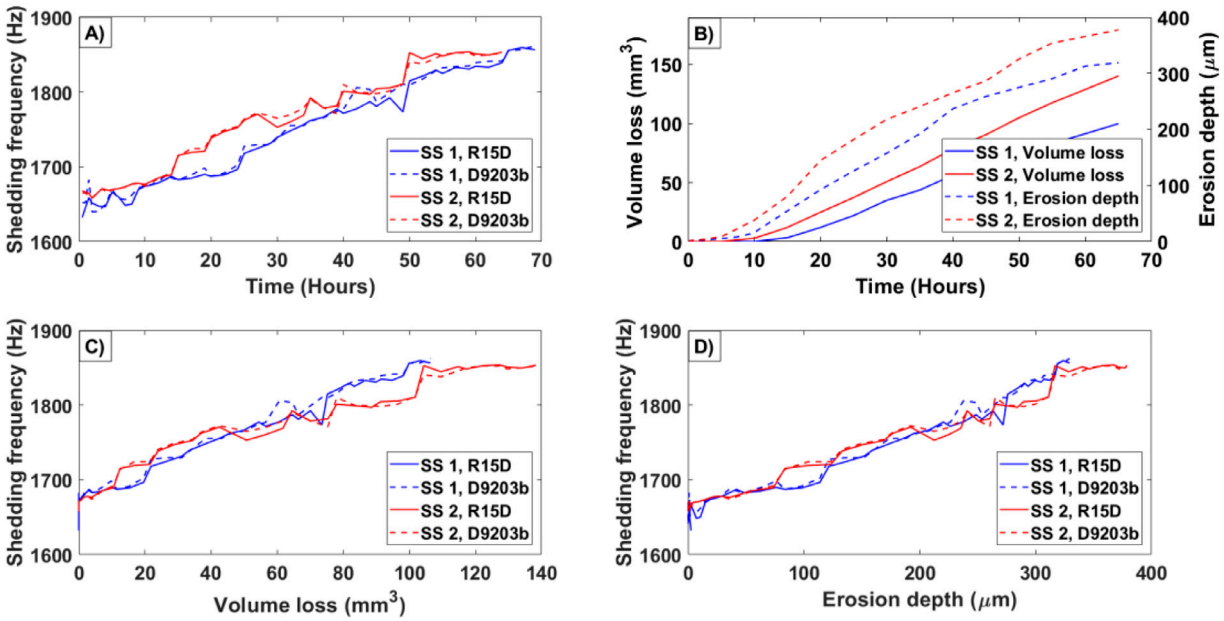


**Fig. 13.** Cavitation shedding frequency as a function of erosion time, combined with volume loss and erosion depth. Cavitation number $\sigma = 0.87$.

measurements are non-intrusive and non-destructive. As long as the cavitation number is constant between two separate measurements, an unchanged shedding frequency corresponds to no change in surface roughness or erosion evolution. However, for a shedding phenomenon to exist and to be detectable, cavitation has to be well developed, as pointed out in the cavitation number analysis.

## 5. Conclusions

The cavitation cloud shedding frequency in cavitation tunnel tests was detected reliably both from a video analysis and from an AE analysis. The frequencies were in good agreement with those simulated by Gavaises et al. (2015), for the same test channel geometry. The AE signal demodulation process proved to be efficient in promoting the shedding frequency that is significantly lower than the lower frequency limit of the AE acquisition system. The AE signals were band-pass filtered so that the lower frequency limit was 100 kHz, and the cavitation shedding frequency was between 1600 Hz and 1900 Hz. The high frequency AE signal acted as a modulated carrier signal for the shedding phenomenon, with the low frequency content not lost with the initial filtering process. Effectively, the shedding frequency remained embedded in the signal, as the growth-collapse process of a cavitation cloud is periodical, and the collapse stage induces high loads that were well detected by AE.

The cavitation shedding phenomenon becomes less pronounced as the cavitation number $\sigma$ increases. The limit of no cavitation state in the tunnel was reached at $\sigma \approx 2.8$, but both the video analysis and the AE analysis began to fail in finding a shedding frequency when $\sigma > 1.5$. A potential explanation is provided by the research of Pelz et al. (2014 & 2017), where the transition between a stationary sheet and cloud cavitation was studied. A sheet cavity does not have any periodical structures, so there is no definable shedding frequency. Additionally, a sheet cavity is much less erosive than cloud cavitation; therefore, it should induce less AE. If one would reliably measure the cloud shedding frequency in a hydraulic machine, the disappearance of the well-defined shedding would reveal the transition from cloud cavitation to stationary sheet cavitation, i.e. the transition from an erosive cavitation to a less erosive type of cavitation. This would require knowledge of the frequency range of the shedding phenomenon, obtained either from CFD or from experiments.

In addition to being able to detect the transition from cloud to sheet cavitation, AE use was demonstrated to be effective in tracking erosion evolution. As the increasing surface roughness leads to increase in the cloud shedding frequency (Hao et al., 2017), the shedding frequency increases while erosion progresses. The shedding frequency was about 1600 Hz when the samples were non-eroded and about 1850 Hz when they were eroded to the practical maximum of the cavitation tunnel. This gradual increase of the frequency was linked to the volume loss and the erosion depth, which were parameters defining erosion evolution. The frequencies were virtually the same for a resonance type and a broadband type AE sensor that were used simultaneously during the tests. The frequencies were not significantly affected by the stainless steel quality of the samples, only by the stage of erosion. It is therefore assumed that the shedding frequency is a parameter related to surface geometry and the flow field.

The presented method could be extended to monitoring hydraulic machine erosion stages, if either the machine experiences cloud cavitation, or the machine could be deliberately moved into a stage where cloud cavitation occurs, even if this stage is not in the normal operation region. No change in shedding frequency between measurements would correspond to no change in erosion evolution. The main advantage of using AE to define the shedding frequency would be the ease of installation in an existing machine, with no intrusion into the flow, along with the possibility to record continuously the AE signal as long as needed.

## Acknowledgements

The authors would like to thank Business Finland, Fortum Power and Heat Oy, Sandvik Mining and Construction Oy, Valtra Oy, Teollisuuden Voima Oyj, and Fortum Foundation for funding the research and for providing technical support. The authors would also like to thank Fabio Villa and Phoevos Koukouvinis for providing their cavitation shedding videos for reanalysis and for the discussion on how to interpret the results.

## Supplementary materials

Supplementary material associated with this article can be found, in the online version, at doi:10.1016/j.ijmultiphaseflow.2019.06.009.

## References


Achenbach, J.D., 1975. Wave Propagation in Elastic Solids. North Holland Publishing.

Alfayez, L., Mba, D., 2005. Detection of incipient cavitation and determination of the best efficiency point for centrifugal pumps using acoustic emission. Proc. Inst. Mech. Eng. Part E 219 (4), 327–344.

ASTM International, 2010. ASTM G32-10, Standard Test Method for Cavitation Erosion Using Vibratory Apparatus.

Berry, J.E., 1997a. High Frequency Enveloping and Demodulation Techniques Using Instruments From Various Vendors. Technical Associates of Charlotte, P.C.

Berry, J.E., 1997b. Tracking of Rolling Element Bearing Failure Stages Using Both Vibration Signature Analysis as Well as High Frequency Envelopping and Demodulation Special Techniques. Technical Associates of Charlotte, P.C.

Brennen, C., Colonius, Y., Wang, A., Preston, A., 2000. Cloud cavitation phenomena. In: Twenty-Second Symposium on Naval Hydrodynamics, pp. 239–253.

Franc, J., Michel, J., 2005. Fundamentals of Cavitation. Springer Science + Business Media, Inc..

Franc, J., Riondet, M., Karimi, A., Chahine, G.L., 2012. Material and velocity effects on cavitation erosion pitting. Wear 274–275, 248–259.

Gavaises, M., Villa, F., Koukouvinis, P., Marengo, M., Franc, J., 2015. Visualisation and les simulation of cavitation cloud formation and collapse in an axisymmetric geometry. Int. J. Multiph. Flow 68, 14–26.

Gnanaskandan, A., Mahesh, K., 2016. Large eddy simulation of the transition from sheet to cloud cavitation over a wedge. Int. J. Multiph. Flow 83, 86–102.

Grosse, C., 2008. Acoustic Emission Testing. Springer Berlin Heidelberg, Heidelberg, Germany.

Hao, J., Zhang, M., Huang, X., 2017. The influence of surface roughness on cloud cavitation flow around hydrofoils. Acta Mech. Sin. 34 (1), 10–21.

He, Y., Shen, Z., 2012. Experimental research on cavitation erosion detection based on acoustic emission technique. In: 30th European Conference on Acoustic Emission Testing & 7th International Conference on Acoustic Emission, pp. 1–8.

Holroyd, T., 2000. Acoustic Emission and Ultrasonics Handbook (Coxmoor's Machine & System Condition Monitoring). Coxmoor Publishing Co., Moreton-in-Marsh, United Kingdom.

Hsiao, C., Ma, J., Chahine, G.L., 2017. Multiscale tow-phase flow modeling of sheet and cloud cavitation. Int. J. Multiph. Flow 90, 102–117.

Inaba, H., 2016. AE sensor (AE Transducer), practical acoustic emission testing. Jpn. Soc. Non-Destruct. Insp. 35–45.

Marple Jr, L., 1999. Computing the discrete-time "analytic" signal via FFT. IEEE Trans. Signal Process. 47, 2600–2603.

Neill, G.D., Reuben, R.L., Sandford, P.M., Brown, E.R., Steel, J.A., 1997. Detection of incipient cavitation in pumps using acoustic emission. Proc. Ins. Mech. Eng. 211 (4), 267–277.

Nishimura, S., Takakuwa, O., Soyama, H., 2014. Effect of nozzle geometry on aggressivity of cavitating jet for cavitation erosion test and applications. In: Kim, K., Chahine, G., Franc, J., Karimi, A. (Eds.), Advanced Experimental and Numerical Techniques For Cavitation Erosion Prediction. Springer, Netherlands, Dordrecht, pp. 283–302.

Ohtsu, M., Enoki, M., Mizutani, Y., Shigeishi, M., 2016. Principles of the acoustic emission (AE) method and signal processing, practical acoustic emission testing. Jpn. Soc. Non-Destruct. Insp. 5–35.

Pelz, P., Keil, T., Groß, T., 2017. The transition from sheet to cloud cavitation. J. Fluid Mech. 817, 439–454.

Pelz, P., Keil, T., Ludwig, G., 2014. On the kinematics of sheet and cloud cavitation and related erosion. Fluid Mech. Appl. 106, 221–237.

Poddar, S., Tandon, N., 2016. Detection of journal bearing vapour cavitation using vibration and acoustic emission techniques with the aid of oil film photography. Tribol. Int. 103, 95–101.

Pollock, A.A., 1986. Classical wave theory in practical AE testing. In: Progress in Acoustic Emission III: proceedings of the 8th International Acoustic Emission Symposium, pp. 708–722.

PREVERO, 2018. The PREVERO Cavitation Erosion Tunnel http://web.archive.org/web/20180327065723/http://www.legi.grenoble-inp.fr/web/spip.php?article1265&lang=fr.

Stutz, B., 2003. Influence of roughness on the two-phase flow structure of sheet cavitation. J. Fluids Eng. 125 (4), 652–659.

Trampe Broch, J., 1984. Acoustic Emission, Mechanical Vibration and Shock Measurements. Brüel & Kjær, pp. 212–236.

van Rijsbergen, M., Foeth, E., Fitzsimmons, P., Boorsma, A., 2012. High-speed video observations and acoustic-impact measurements on a NACA 0015 foil. In: 8th International Symposium on Cavitation (CAV 2012), pp. 958–964.

Ylönen, M., Saarenrinne, P., Miettinen, J., Franc, J., Fivel, M., Nyyssönen, T., 2018. Cavitation erosion resistance assessment and comparison of three francis turbine runner materials. Mater. Perform. Charact. 7 (5), 1107–1126.

# PUBLICATION V

**Martensitic Steel Microstructure Effects in Cavitation Erosion**

Ylönen, Markku., Nyyssönen, Tuomo., Honkanen, Mari. & Peura, Pasi.

Unpublished Manuscript